



Microplasticity at Room Temperature in α/β Titanium Alloys

S. HÉMERY, P. VILLECHAISE, and D. BANERJEE

The current understanding of room temperature microplasticity in α/β titanium alloys is reviewed with a special emphasis on dual-phase engineering alloys. As the interplay between microstructure and deformation mechanisms governs both the microscale and macroscale mechanical response, a brief description of the main features of α/β microstructures is first provided. Elastic and plastic deformation in individual phases is then described. The complex interactions that govern the effect of grain boundaries, phase interfaces and microtexture on deformation behaviour are reviewed. Crystal plasticity simulations have evolved over the past decade as a key technique to obtain a mechanistic understanding of the deformation of Ti alloys. Micromechanical aspects are emphasized with a discussion of input parameters required to achieve realistic constitutive modeling. As microplasticity is especially relevant in cyclic loading such as experienced in-service by components, the current understanding of the relation of this regime with fatigue and dwell-fatigue behavior is briefly summarized in the final section.

<https://doi.org/10.1007/s11661-020-05945-4>

© The Minerals, Metals & Materials Society and ASM International 2020

I. INTRODUCTION

TITANIUM and its alloys constitute a class of two-phase microstructures based on its bcc (β) and hcp (α) allotropic modifications. A recent description of various aspects of the physical and mechanical behaviour of these alloys is provided in Reference 1. The α and β phases can be arranged in a variety of distributions, morphologies, volume fractions and length scales that govern the properties of the individual phases, as well as the interactions between them. The properties of the β phase are particularly susceptible to nanoscale metastable decomposition reactions. The development of plasticity in such microstructures has been investigated more recently with a variety of techniques that include high resolution digital image correlation and high energy X-ray diffraction coupled crystal plasticity based modelling that provide insights into the early deformation behaviour that sets the stage for macroscopic yield and damage accumulation at small strains. It is this aspect that we focus on in this article. We first

provide an introduction to α/β microstructures and then survey elasticity, fine structure of dislocations and twinning and critical resolved shear stresses in individual phases in some detail since these govern the onset of plasticity. This is followed by a description of plasticity development in various microstructural and microtextural modifications of titanium alloys including the role of α/α grain boundaries and α/β interfaces. We conclude with a brief note on crystal plasticity modelling in relation to these studies and a summary of the effects of incipient plasticity on mechanical behavior under fatigue and dwell-fatigue loadings.

II. A BRIEF DESCRIPTION OF α/β MICROSTRUCTURES

Titanium undergoes an allotropic transformation from bcc β to hcp α at 882 °C. Alloying additions such as Al, and O stabilize the α phase while bcc elements such as Mo, V, Ta, Nb, Cr and Fe are among those that are commonly used to strengthen and stabilize the β phase. Sn, Zr and Hf are relatively neutral additions. As schematically shown in Figure 1(a), Ti alloys are generally classified as α , $\alpha + \beta$ (including near- α), metastable β and β alloys according to their position in a pseudo-binary section through a β isomorphous phase diagram.^[2] The metastable β alloys lie in the two phase $\alpha + \beta$ region but are distinguished from $\alpha + \beta$ alloys in that M_s for these alloys is below room

S. HÉMERY and P. VILLECHAISE are with the Institut Pprime, CNRS-ENSMA, Université de Poitiers, UPR CNRS 3346, Physics and Mechanics of Materials Department, ENSMA Téléport 2, 1 avenue Clément Ader, BP 40109, 86961 Futuroscope Chasseneuil Cedex, France. Contact e-mail: samuel.hemery@ensma.fr
D. BANERJEE is with the Department of Materials Engineering, Indian Institute of Science, Bangalore 560012, India.

Manuscript submitted February 26, 2020.

Article published online August 18, 2020

temperature. A variety of metastable and short-range atomic configurations emerge in these phases on alloying that influence both the dislocation character and distribution and stress induced ‘plasticity’ and are therefore summarized below. The β phase is susceptible to instabilities that depend on the variation of elastic constants as a function of composition and temperature. The martensites, hexagonal α' and orthorhombic α'' are well known.^[2] The former is present in β stabilizer lean alloys while the latter is an intermediate structure that forms in more enriched alloys. With higher β stabilizing additions nanometric dispersions of ω phase^[2] and O' ^[3,4] are observed on quenching from the high temperature β phase field. These are products of displacement controlled reactions related to $2/3 \langle 111 \rangle$ longitudinal phonon waves and $\{110\}\langle 110 \rangle$ transverse displacement waves, respectively, and can coexist over temperature and composition ranges that depend on alloy content. In addition local distortions and charge density modifications around alloying elements such as V have been postulated.^[5] α has a large solubility for O as shown in Figure 1(b). Ordering associated with oxygen in the α phase has been discussed as early as in the fifties^[6] and has more recently been quantified through first-principles statistical mechanics approach based on cluster expansion^[7] to show that ordered phases based on Ti_6O may be stable in titanium rich compositions. Short range order (SRO) also appears on alloying with Al^[8] and leads finally to nanodispersions of the intermetallic Ti_3Al (α_2) phase. The presence of these ordering effects depends on Al content of the α phase in the alloy (Figure 1(c)), and thermal treatment. Hydrogen has a limited solubility in the α phase and is a β stabiliser. Its solubility in α and interaction with dislocations is expected to be influenced by the very large specific volume difference (~ 17 pct) between hydride and α , and its effect on metastable decomposition in β has not been studied. Because of its high diffusivity its local concentration may be influenced by local stresses and strains in a manner that has not been quantified.

In two-phase alloys, α precipitates in a lath/plate form from the β phase with the Burgers orientation relationship (BOR): $(101)_\beta \parallel (0001)_\alpha$, $[\bar{1}11]_\beta \parallel [11\bar{2}0]_\alpha$, $[\bar{1}21]_\beta \parallel [1100]_\alpha$ as 12 crystallographic variants. As a consequence of this orientation relationship parallelism or near-parallelism between slip planes and direction exists in the α and β phases that, together with the magnitude of the Burgers vectors and the defect structure at the interface, will influence slip transfer between the two phases. Very small deviations from the BOR have been documented,^[9] and α/β interfaces of BOR α are semi-coherent with a structure described in detail recently.^[10] The mean free path for slip of multivariant α distributions is influenced by the geometry of the distribution^[11] as will be described later in the paper.

α initially forms at grain boundaries of the β phase. Grain boundary or triple point α is invariably BOR related to one or more of the adjacent grains.^[11–13] At low levels of β stabilizer addition and high transformation temperatures, α grows as widmanstätten sideplates

from grain boundary α into the β grain with which the grain boundary α has the BOR and can consume the entire grain (Figure 2(a)). This colony structure consists of identical, parallelly oriented variants of the α phase with thin ribs of retained β . At lower transformation temperatures or with higher β stabilizer content, transgranular α begins to dominate the structure. Features of variant distribution in transgranular α have been described in Reference 14. The distribution of transgranular α is strongly affected by stress accommodation. Groups or clusters of trivariant α that share a common $[111]_\beta/[11\bar{2}0]_\alpha$ direction are often observed (Figures 2(b) and (d)) and their crystallography is shown in Figure 2(e). At higher β stabilizer content and higher transformation temperatures, these trivariant clusters are composed of bundles of α laths (Figure 2(c)). Each individual bundle arises from extensive branching of α laths during growth through a solid state dendrite formation mechanism.^[15] Trivariant clusters of individual plates are observed at lower transformation temperatures. The distribution of α can be manipulated through transformation *via* intermediate phases such as ω .^[16] The martensitic transformation to α' is not utilized in engineering alloys in conventional processing. However, in additive manufacturing, and much additive work has focused on the Ti-6Al-4V $\alpha + \beta$ alloy, the as-solidified structure normally consists of columnar parent β grains with α' whose variant distribution can be affected by residual stress during processing. Subsequent thermal cycles during additive build up or by post processing heat treatment result in α' decomposition and represents a different pathway to the final structure as compared to standard processing.^[17]

Thermomechanical processing can be used to convert the lath α to equiaxed α . Various aspects of morphology and texture reconstitution have been recently reviewed.^[18] All titanium alloys are initially processed and annealed in the single phase β region to homogenize solidification microsegregation and refine the coarse as-solidified β grains. They can then be hot worked in the single phase α region or in the two-phase $\alpha + \beta$ region (depending on composition) to change the morphology of the lath α that forms on cooling from the β phase region. This is usually followed by a solution or recrystallization anneal along with a final stabilization or aging treatment for the two-phase alloys. These processing paths are schematically indicated in Figure 3(a) and resulting microstructures shown in Figure 3(b) through (d). Some characteristic features in relation to heterogeneities in plasticity will be briefly described here. The spheroidization of the α phase occurs typically through a geometric dynamic recrystallisation process involving strain induced pinching off of the α laths. Such a process leads to a deviation from the BOR and it is generally assumed that equiaxed α realized through thermomechanical processing has no orientation relationship with the surrounding β grains. However, a classic recrystallization process can also occur on subsequent heat treatment of heavily worked structures or dynamically during thermomechanical processing. This process has an epitaxial nature in the

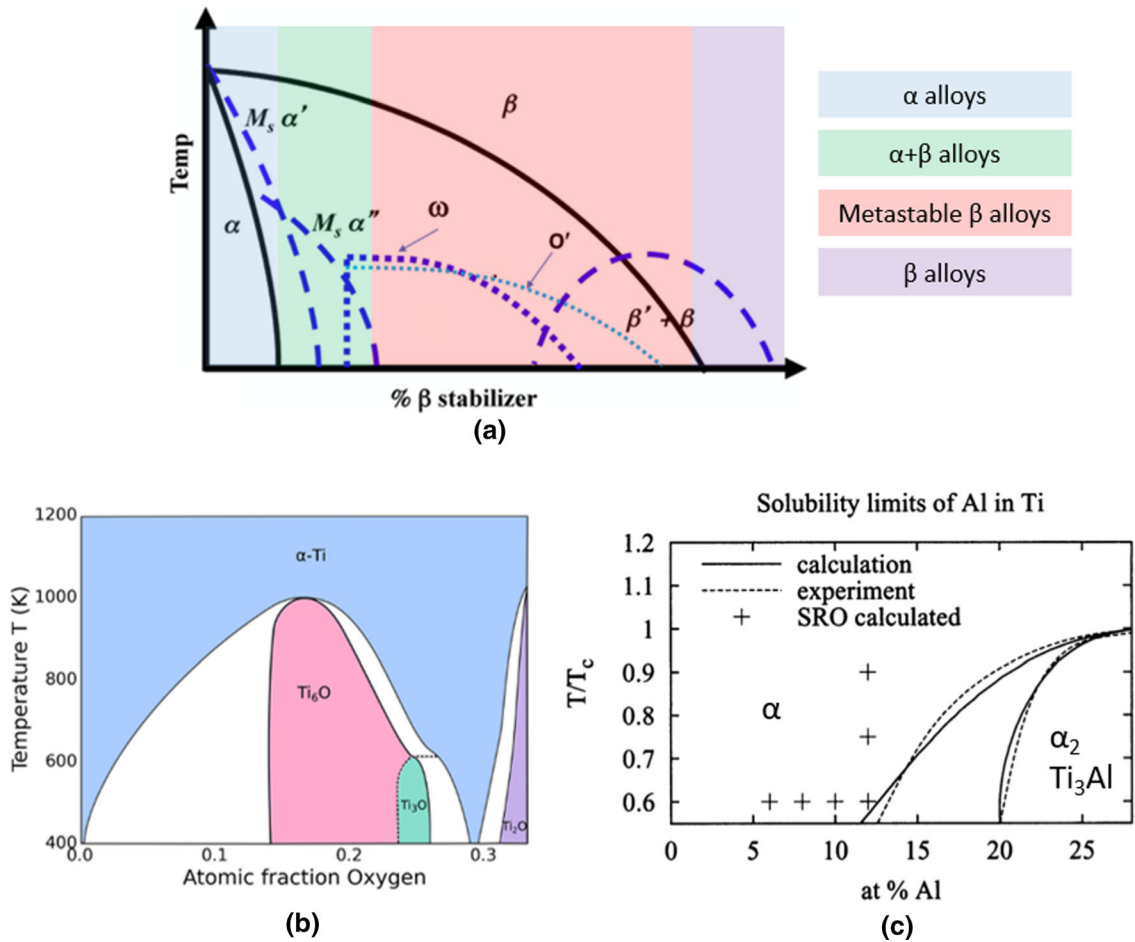


Fig. 1—(a) A phase diagram illustrating equilibrium and non-equilibrium phases observed in titanium alloys, (b) the Ti-O phase diagram (reprinted with permission from Ref. [7]) and (c) the Ti-Al phase diagram (reprinted from Ref. [8]).

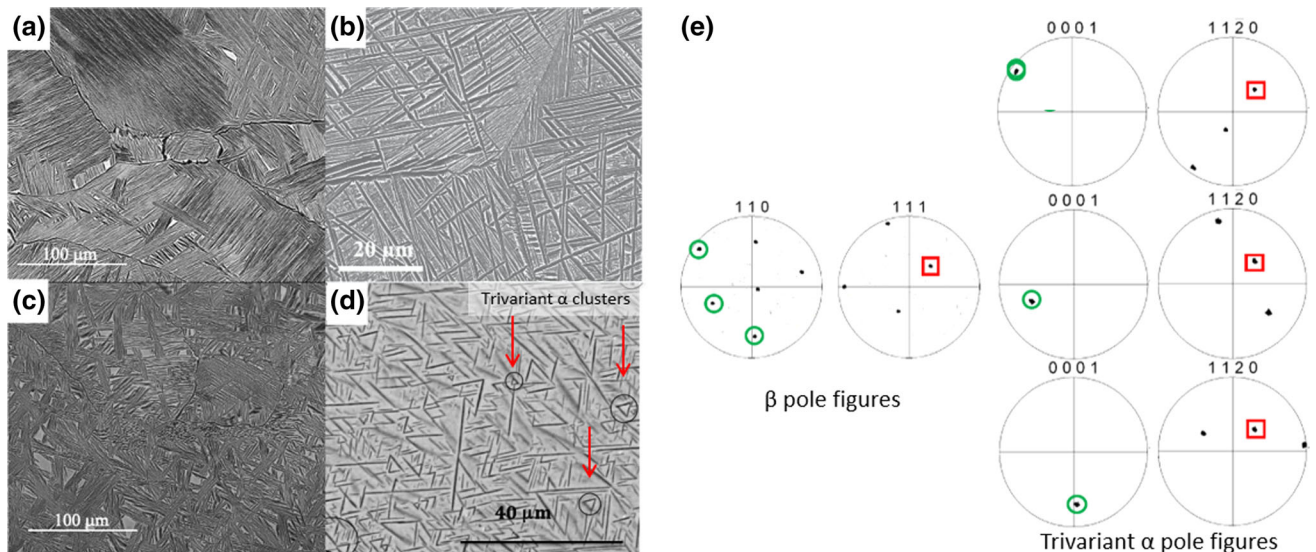


Fig. 2—Lath α morphology and distribution (a) colony structures, (b) transgranular basketweave α , (c) transgranular α bundles, (d) transgranular α in a high β volume fraction alloy (trivariant clusters are circled), (e) trivariant α orientation relationships showing a common $[111]_{\beta} // [1120]_{\alpha}$.

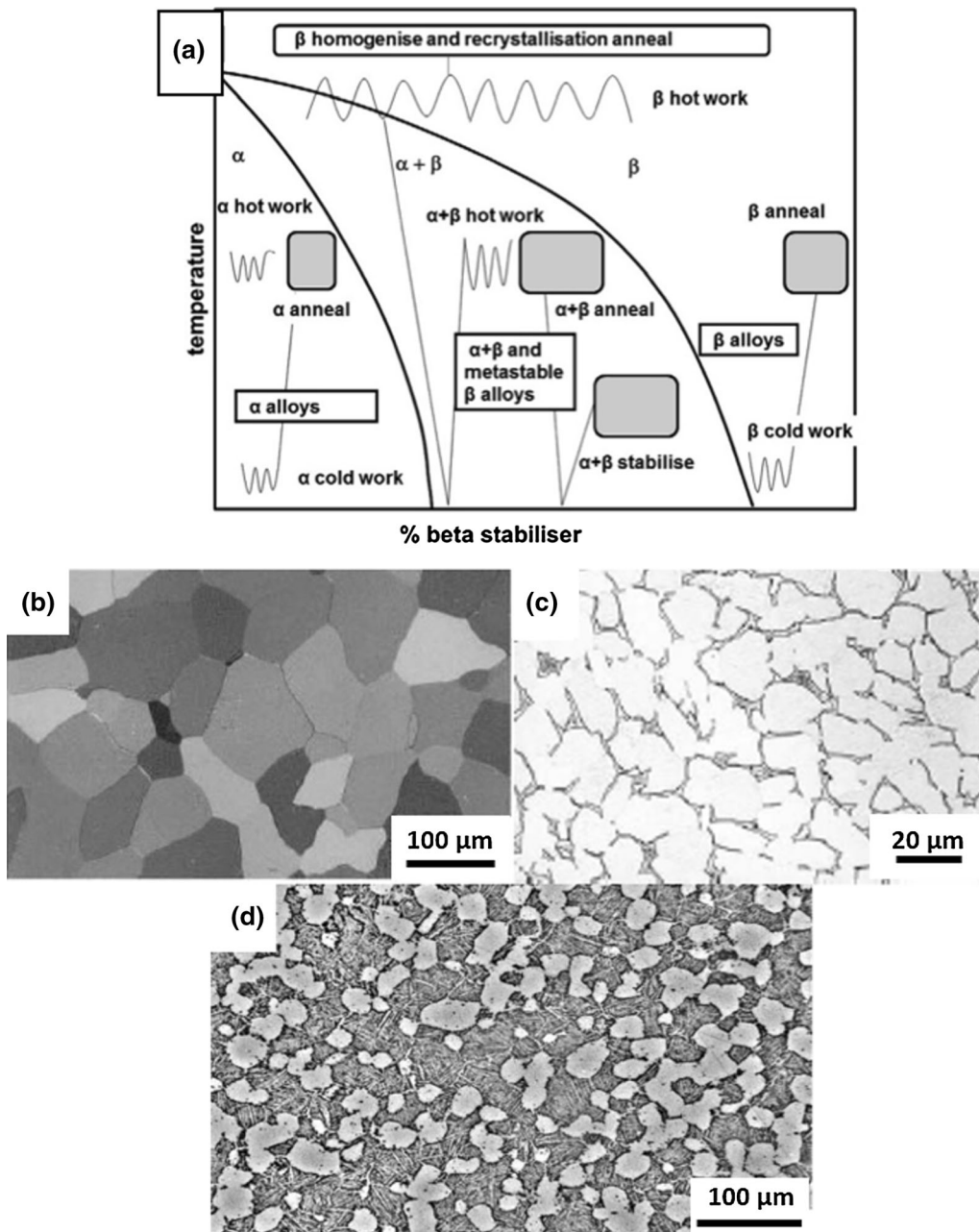


Fig. 3—(a) Different thermomechanical processing routes for titanium alloys, with curved lines indicating mechanical working, (b) single phase polycrystalline α , (c) equiaxed α structure with β at α grain boundaries, (d) bimodal structures with equiaxed α and transformed β containing α laths.

sense that newly recrystallized α and β grains form with the BOR to adjacent phases and leads to a restoration of the BOR.^[19] As a consequence, equiaxed α grains can often be BOR related to surrounding β (Figures 4(a) and (b)). Also as a consequence of this epitaxial recrystallisation process, β grains can be related to each other by special orientations. Figure 4(c) presents all special misorientations between the β grains shown in (d) by the β boundaries marked in yellow. Finally, coarse colony structures tend to yield domains or zones of equiaxed alpha that are similarly oriented

(Figure 4(e)).^[20] These are often called macrozones or microtextured regions (MTR).

The microtexture associated with each of these processes described above has consequences for incipient plasticity because the BOR results in elastic interactions between the two phases that govern the initiation of slip through local stress redistribution and also allows the near parallelism of several slip systems in the two phases that influences the development of plasticity in ways that will be described in subsequent sections.

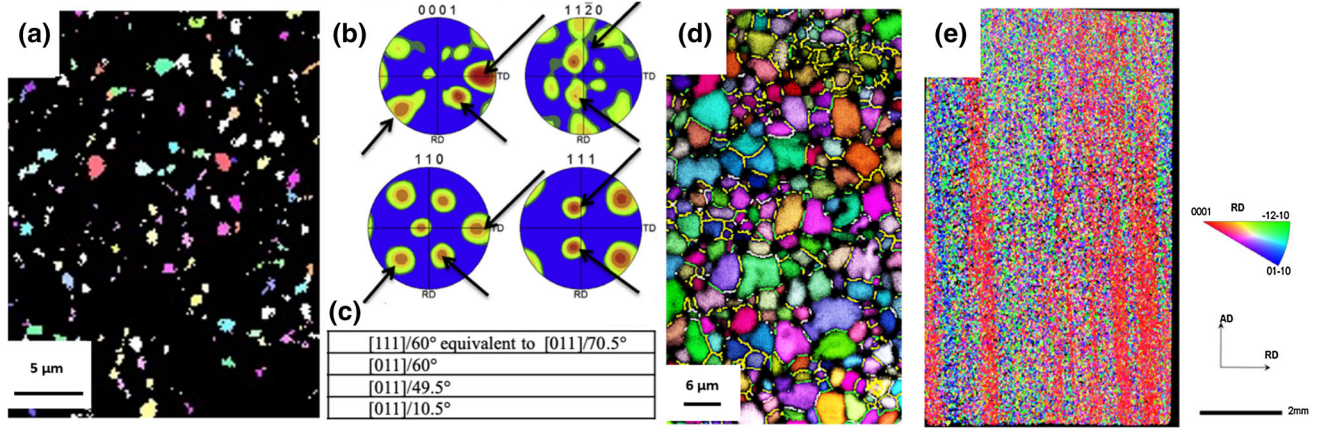


Fig. 4—(a) Phase partitioned image of equiaxed α , (b) pole figure showing overlap of (0001) and $[11\bar{2}0]$ α and $\{110\}$ and $\langle 111 \rangle$ β poles respectively from the recrystallized structure (reprinted with permission from Ref. [19]), (c) all special misorientations between the β grains shown in (d) by the β boundaries marked in yellow (reprinted from Ref. [14]), (e) macrozones or microtextured regions of similarly oriented α (reprinted with permission from Ref. [20]).

Table I. Elastic Constants for the α Phase Taken from Literature

Material	C_{11} (GPa)	C_{12} (GPa)	C_{13} (GPa)	C_{33} (GPa)	C_{44} (GPa)	E_{av} (GPa)	E_{min}/E_{max}	References
Ti	162	92.0	69.0	180	46.7	120	1.37	[23]
Ti	154	86.0	67.3	183	46.7	120	1.45	[25]
Ti-6Al	136	78.0	68.5	163	40.6	102	1.41	[24]
Ti-6242	141	76.9	57.9	163	48.7	114	1.41	[24]
Ti-7Al	165	81.2	62.9	175	48.2	127	1.21	[22]
Ti-6Al-4V	143	110	90	177	40	86	2.06	[26]
Ti-6Al-4V	169	89	62	196	43	128	1.50	[27]

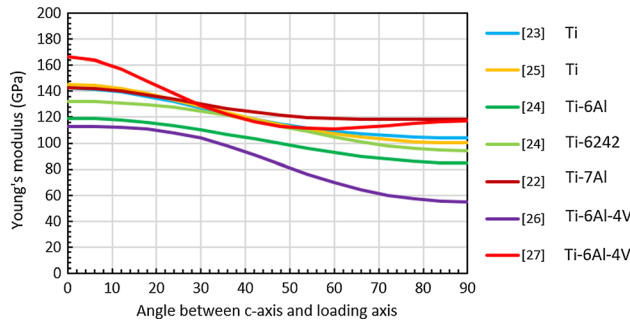


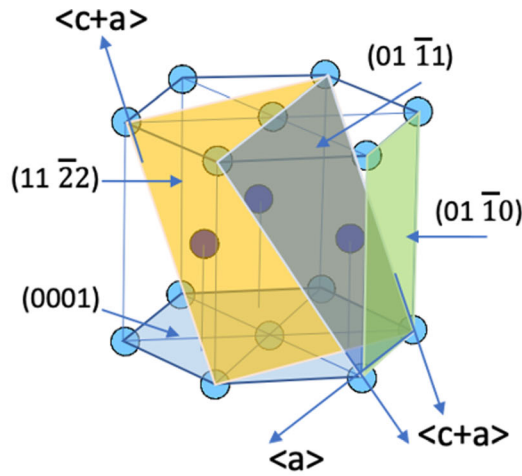
Fig. 5—Directional Young's modulus as calculated from elastic constants in Table I.

III. PLASTICITY IN THE A PHASE

A. Elasticity in the α Phase

Elastic anisotropy plays a critical role in the early slip activity in Ti alloys. Both α and β phases display a marked elastic anisotropy. Numerous sets of elastic constants have been proposed to describe the transverse isotropic behavior of the α phase, that is in directions perpendicular to the c -axis.^[21–27] Several datasets are presented in Table I and directional Young's moduli are plotted in Figure 5. C_{66} , which is not indicated, can be calculated as $(C_{11}-C_{12})/2$. Although a substantial scatter

in the values is observed, several authors found a good agreement with the early data reported by Fisher and Renken.^[21–23] It is interesting that this agreement holds for a Ti-7Al alloy, suggesting that no major effect of Al additions on elastic constants exists. Most of the datasets lead to a ratio of the maximum modulus to the minimum modulus around 1.4. However, a careful analysis raises several questions about whether any dataset can properly reproduce the elastic deformation behavior of α/β alloys. In order to assess this point, E_{av} , the Young's modulus for an average distribution of orientation (*i.e.*, obtained through integration over declination angles between 0 and 90 deg) was calculated and is indicated in Table I. It is worth noting that such an estimate does not reflect the pronounced influence of texture on Young's modulus values at the macro-scale.^[2,28] The Young's modulus of α and $\alpha + \beta$ Ti alloys is typically of the order of 115 ± 5 GPa. While most datasets provide similar average values, an average modulus as low as 86 GPa for Ti-6Al-4V or 102 GPa for Ti-6Al and as high as 127 GPa for Ti-7Al or 128 GPa from Ti-6Al-4V is unexpected. In particular, a Young's modulus about 100 GPa is reported in Turner *et al.* for polycrystalline Ti-7Al^[29] while the minimum Young's modulus (*i.e.*, for a $[10\bar{1}0]$ or $[11\bar{2}0]$ direction) that can be calculated with the associated dataset is 118 GPa. It is thus suggested that these datasets have to be considered



Slip system type	Burgers vector type	Slip direction	Slip plane	No. of slip systems
1	\bar{a}	$\langle 11\bar{2}0 \rangle$	(0001)	3
2	\bar{a}	$\langle 11\bar{2}0 \rangle$	$\{10\bar{1}0\}$	3
3	\bar{a}	$\langle 11\bar{2}0 \rangle$	$\{10\bar{1}1\}$	6
4	$\bar{c} + \bar{a}$	$\langle 11\bar{2}3 \rangle$	$\{10\bar{1}1\}$	12
5	$\bar{c} + \bar{a}$	$\langle 11\bar{2}3 \rangle$	$\{11\bar{2}2\}$	6

Twinning plane (1st undeformed plane) (K_1)	Twinning shear direction (η_1)	Second undeformed plane (K_2)	Direction of intersection of plane of shear with K_2 (η_2)	Plane of shear perpendicular to K_1 and K_2	Magnitude of twinning shear
$\{10\bar{1}2\}$	$\langle 10\bar{1}\bar{1} \rangle$	$\{\bar{1}012\}$	$\langle 10\bar{1}1 \rangle$	$\{1\bar{2}10\}$	0.167
$\{11\bar{2}1\}$	$\langle 11\bar{2}\bar{6} \rangle$	(0002)	$\langle 11\bar{2}0 \rangle$	$\{\bar{1}100\}$	0.638
$\{11\bar{2}2\}$	$\langle 11\bar{2}\bar{3} \rangle$	$\{11\bar{2}\bar{4}\}$	$\langle 22\bar{4}3 \rangle$	$\{\bar{1}100\}$	0.225

Fig. 6—Slip and twinning systems in the α phase.

with care for use with conventional Ti alloys. Retained β phase, which is generally more compliant than the α phase and associated with a fraction of 10 to 15 pct, is unlikely to account for such discrepancies. Finally, prior studies have shown that the oxygen additions induce an increased Young's modulus.^[30,31] Such considerations are very important as the onset of slip activity and the deformation behavior in the plastic regime are governed by these constants.

B. Deformation Modes

The α phase can deform by slip or twinning and these systems are illustrated in Figure 6. The earliest discussion on slip and twinning in the α phase appears to be that of Churchman in 1954.^[6] Hard sphere models of slip on various slip systems, estimates of critical resolved shear stress values (CRSS) and the effect of impurities are assessed in this article, and the extent to which this article anticipates current understanding is quite remarkable. Since extended screw orientations of $\langle a \rangle$ dislocations are commonly observed in pure titanium,^[32] the core structure of $\langle a \rangle$ screw dislocations has been

examined in some detail quite recently.^[33–35] While stacking fault energies and core structures can vary depending upon whether density functional (DFT) or embedded atom (EAM) techniques are used, there appears to be agreement that the cores of screw $\langle a \rangle$ dislocations are spread in prismatic planes in a metastable configuration and in a more stable configuration on first order pyramidal planes. The mobility of dislocations is however lower on pyramidal planes than on prismatic planes (Figure 7(a)), and there is a low barrier to cross slip from pyramidal to the prismatic planes. This leads to a 'locking-unlocking' mechanism of glide in which sessile screw dislocations immobilized on prismatic planes can unlock and glide on prismatic planes before locking again occurs. As a consequence lattice friction effects are prevalent even in high purity titanium at temperatures less than 150 K unlike in fcc metals.^[36] Perhaps non-intuitively for those familiar with slip in fcc metals, there is no stable core dissociation in basal planes of Ti, and as a consequence, glide in the basal plane has all the features of a Peierls mechanism where screw orientation can be locked by dissociation on either prismatic or pyramidal planes.^[37,38]

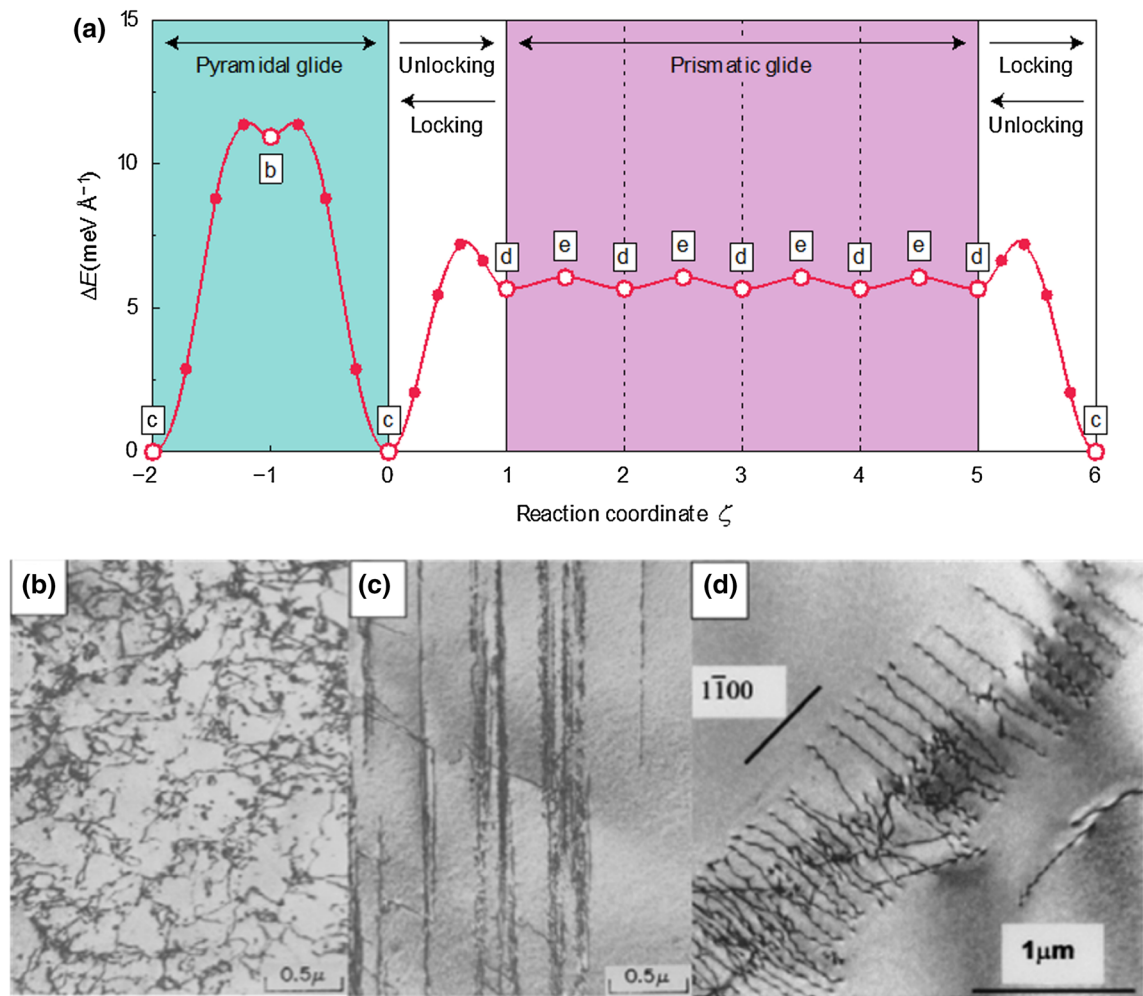


Fig. 7—(a) The energy barrier to the mobility of dislocations in pyramidal and prismatic glide (reprinted with permission from Ref. [34]), (b to d) the effect of O and Al on slip character in titanium: (b) pure Ti with 475 wppm O (reprinted with permission from Ref. [52]), (c) Ti with 5200 wppm O (reprinted with permission from Ref. [52]), (d) Ti-5 wt pct Al (reprinted from Ref. [53]).

Oxygen and aluminum are critical alloying additions that control strength and plasticity in the α phase. Oxygen is a potent strengthener of titanium and enhances thermally activated flow.^[39] Calculation and experiment show that there is a strong repulsive interaction between dislocations gliding in the prismatic plane and oxygen in octahedral sites, since such sites are destroyed by prismatic core dissociations.^[40,41] This results in enhanced transformation and locking of prismatic dislocations to the relatively sessile pyramidal core. Double cross slip processes that can arise from such interactions lead to the formation of jogged screw dislocations.^[42] A study of Al additions on core structures^[43] indicates that Al can promote basal glide by reducing the energy difference between the basal core, and prismatic and pyramidal cores.

A deviation from Schmid's law and related compression-tension asymmetry and orientation effects on CRSS are observed in titanium.^[32,44,45] Calculations show that tension or compression along the $[1\bar{1}00]$ direction, that is with non-shear stress components along the prismatic plane, can extend or contract core dissociation on the

prismatic plane respectively thus increasing or decreasing the CRSS for far-from-basal orientations of deformation.^[35] $\langle c + a \rangle$ slip in titanium preferentially occurs on the 1st order pyramidal planes but shows a strong-tension compression asymmetry.^[46–48] The stacking fault energy on the first-order pyramidal planes is about half that on 2nd order pyramidal planes. The CRSS is considerably lower in tension than in compression and cross slip to second order pyramidal planes is observed in compression leading to wavy slip.

Deformation twinning modes that allow extension along the c -axis or contraction (Figure 6) have been observed in pure titanium.^[2] This deformation mode is important for stress orientations along the c -axis because if the $\langle c + a \rangle$ slip mode does not operate because of its relatively high CRSS (as discussed in the next section) 5 independent slip systems are then not available for the compatible deformation of polycrystalline material. Recent publications have also explored the interaction of oxygen with twin boundaries in titanium.^[33,49] The propensity for twinning decreases with increasing temperature and decreasing strain rate

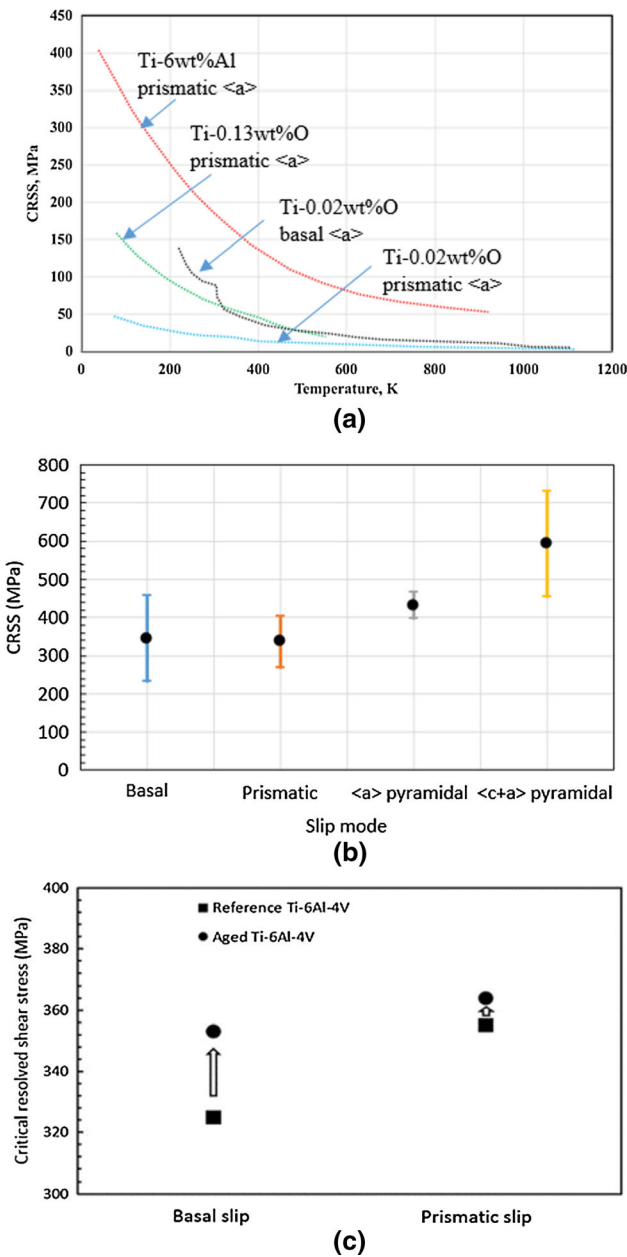


Fig. 8—(a) CRSS of prismatic and basal systems in the α phase with different O and Al contents from the data of [39] and, [53] (b) CRSS of various slip systems in the α phase at room temperature from the data of Table I and (c) influence of ageing on (a) basal and prismatic CRSS values (reprinted with permission from Ref. [68]).

and decreasing grain size (although decreasing strain rates increase twin width).^[50] However, twinning is commonly observed after significant amounts of applied strain in pure titanium^[51] and may not be relevant in the microplasticity regime in single phase α alloys. Alloying inhibits twinning such that twinning in the α phase is not a major deformation mode in commercial alloys of titanium containing high levels of Al or O.^[52,53] A more recent investigation also describes the effect of Al on the propensity for twinning.^[54]

Of considerable significance to the development of plasticity in titanium alloys is the substantial change of dislocation distribution in α with alloying. Williams and

coworkers^[52,53] showed that transitions from wavy to planar slip occurs with increasing O and Al content and planar slip persists to higher temperatures at higher O and Al levels (Figures 7(b) through (d)). It is believed that these transitions are related to the appearance of SRO at higher Al and O levels. Strain localization is discussed again in following sections on plasticity in dual phase structures.

C. Critical Resolved Shear Stresses in the α Phase

Critical resolved shear stresses in titanium have been measured in a variety of ways. Early work evaluated critical resolved shear stress in single crystals of α . More recently the statistics of slip on different slip systems determined using trace analysis and EBSD, nanoindentation and high energy X-ray diffraction have been employed in polycrystalline single phase, and 2-phase engineering alloys. An excellent description of the core techniques of each of these methods and a comparison of values measured by them is available in Reference 55.

Figure 8(a) shows early data on titanium as reviewed by Conrad in 1981.^[39] The CRSS for prismatic $\langle a \rangle$ slip is lower than that of basal $\langle a \rangle$ slip, in accordance with core structure studies described earlier. Oxygen has a strong strengthening effect and more so on prismatic glide, again in consistence with core interactions (Figure 8(a)). The first estimates of the CRSS for pyramidal $\langle c + a \rangle$ slip were made in Reference 56 using single-crystal microcantilever tests and are 2 to 3 times that of prismatic and basal slip.

Al effects on CRSS were evaluated by Williams *et al.*^[53] and indicate that Al has a stronger effect on the CRSS of prismatic slip than basal slip such that the two slip modes become equally probable at about 300 K in the Ti-6 wt pct Al alloy which serves as a prototype composition for the α phase of engineering 2-phase alloys. The CRSS for pyramidal $\langle c + a \rangle$ slip is about 4 times that for basal and prismatic $\langle a \rangle$ slip at 300 K in this data set in compression tested Ti-6 wt pct Al. A non-exhaustive overview of values reported in the literature for Ti alloys with 5 to 7 weight pct aluminum is given in Table II, and Figure 8(b) summarizes this data. The α phase in the Ti-6Al-4V alloy can include small amounts of V while that in the Ti-5Al-2.5Sn alloy contains Sn and in Ti6242 and Ti6246 alloys contains Mo, Sn and Zr. These values often include grain size related strengthening and may be higher than single-crystal values.^[14] CRSS estimation based on crystal plasticity simulations leads to values that are dependent on the other parameters used such as the elastic constants. Basal and prismatic CRSS values are notably lower than those of other deformation modes. Most CRSS datasets indicate very similar CRSS values for basal and prismatic slip. Basal slip is usually reported to occur first for such alloys.^[57-59] This is assisted by the elastic anisotropy of the α phase as grains well oriented (*i.e.*, with a Schmid factor of 0.5) for basal slip experience, in average, a higher stress than α grains well oriented for prismatic slip.^[60] As shown in Table II, most ratios of the $\langle a \rangle$ pyramidal CRSS to the prismatic CRSS ranges between 1 and 1.3. In contrast, values for

Table II. CRSS Values for Basal, Prismatic and Pyramidal Slip Systems with the Loading Mode and the Reference Indicated

Alloy (Wt Pct)	Basal CRSS (MPa)	Prismatic CRSS (MPa)	$\langle a \rangle$ Pyramidal CRSS (MPa)	$\langle c + a \rangle$ Pyramidal CRSS (MPa)	Tension/Compression	References
Ti-6.6Al	190 (0.95)	200	X	770 (3.9)	Compression	[53]
Ti-6Al	322 (1.01)	320	X	846 (2.6)	Compression	[101]
Ti-7Al	328 (0.96)	342	417 (1.2)	349 (1.0)	Tension	[171]
Ti-6Al-4V	X	376	X	441 (1.2)	Tension	[46]
Ti-6Al-4V	444 (1.13)	392	404 (1.0)	631 (1.6)	Compression	[46]
Ti-6Al-4V	330 (0.83)	396	X	561 (1.4)	Tension	[102]
Ti-6Al-4V	353 (0.89)	397	X	593 (1.5)	Tension	[217]
Ti-6Al-4V	290 (0.91)	320	430 (1.3)	440 (1.4)	Tension	[26]
Ti-6Al-4V	385 (0.94)	410	420 (1.0)	430 (1.0)	Tension	[26]
Ti-6Al-4V	420 (1.14)	370	490 (1.3)	590 (1.6)	Tension	[173]
Ti-6Al-4V	350 (1.27)	275	470 (1.7)	570 (2.1)	Both	[163]
Ti-6Al-4V	494 (1.25)	395	395 (1)	494 (1.3)	Tension	[218]
Ti-6Al-4V	513	X	X	612	Compression	[218]
Ti-6Al-4V	338 (0.96)	352	X	X	Tension	[100]
Ti-5Al-2.5Sn	(1.23)	(1)	(23)	(43)	Tension	[219]
Ti-6242	270 (1.13)	240	X	X	Compression	[220]
Ti-6242	385 (1.05)	365	X	640 (1.8)	Tension	[110]
Ti-6242	430 (0.92)	465	X	760 (1.6)	Compression	[110]
Ti-6242	335 (0.92)	364	X	X	Tension	[57]
Ti-6246	362 (0.88)	410	X	X	Tension	[57]

Normalized values with respect to the prismatic CRSS are given in parenthesis.

Table III. Elastic Constants for the Body Centered Cubic β Phase from the Literature

Material	C_{11} (GPa)	C_{12} (GPa)	C_{44} (GPa)	A	References
Ti-7.5Cr	160	87	54	1.5	[221]
Ti-10Cr	133	95	43	2.2	[221]
Ti-15Cr	140	114	44	3.4	[221]
Ti-30Cr	159	94	48	1.5	[221]
Ti-40Nb	157	112	40	1.8	[222]
Ti-6242	135	113	55	5	[24]
Ti17	174	116	41	1.4	[223]
Ti17	167	115	44	1.7	[223]
Ti-29Nb-Ta-Zr	65	41	32	2.6	[224]
Ti-25Nb-Ta-Zr	91	56	36	2.1	[224]
Ti-40Nb	144	119	33	2.7	[225]
Ti-15Mo-2.7-Nb-3Al-0.2Si (Beta-21S)	153	101	57	2.2	[226]
Ti-15Mo-2.7-Nb-3Al-0.2Si (Beta-21S)	154	110	42	1.9	[223]
Ti-30Nb	137	110	33	2.4	[227]
Ti-36Nb-5Zr	133	99	26	1.5	[228]
Ti-4.5Fe-6.8Mo-1.5Al (Ti-LCB)	246	44	21	0.2	[229]
Ti-10V-2Fe-3Al	140	128	50	8.3	[230]

$\langle c + a \rangle$ pyramidal slip exhibit a substantial scatter and vary from 1 to 4 for most datasets. However, one may notice a high density of values between 1 and 1.8 in tension. Finally, one has to keep in mind the well-known tension-compression asymmetry in yield strength of titanium alloys for both $\langle a \rangle$ and $\langle c + a \rangle$ slip, as described earlier.

The effect of other alloying elements of the α phase has been less investigated. However, recent studies highlighted that their effect could be limited on the CRSS values and basal/prismatic CRSS ratios.^[61] The main reason invoked is that the α phase contains very small amounts of β stabilizers and that aluminum and O are the main alloying elements present in solution in the

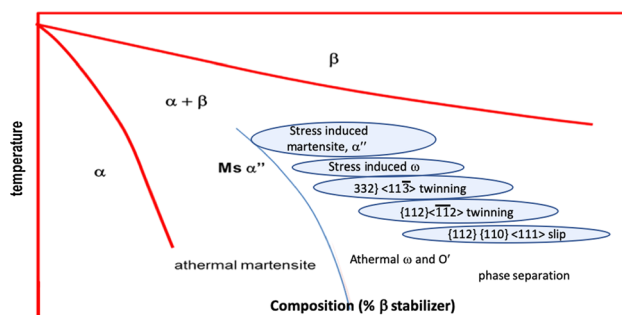
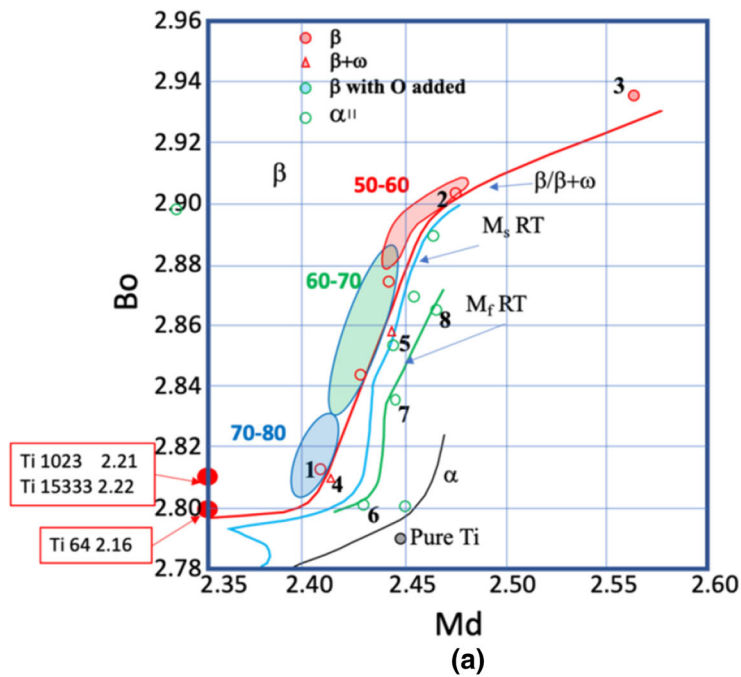


Fig. 9—Trends in deformation modes in β phase as a function of composition. Various domains of deformation overlap.



1	Ti-15Mo
2	Ti-64Ta
3	Ti-50Ta-20Zr
4	Ti-14Mo
5	Ti-35Nb-0.2O
6	Ti-7.5Mo
7	Ti-25Nb
8	Ti-50Ta

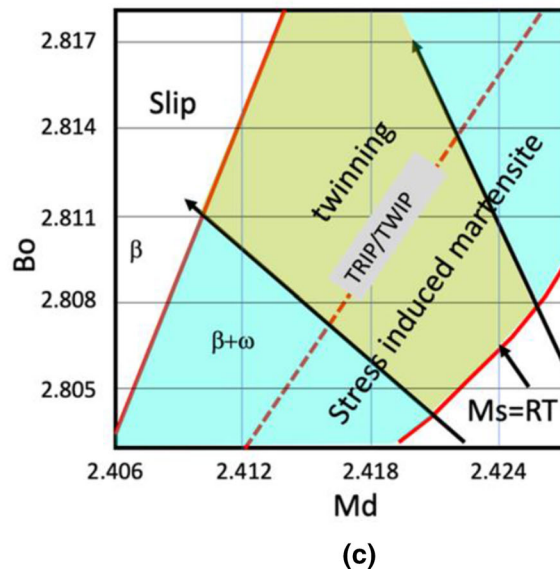
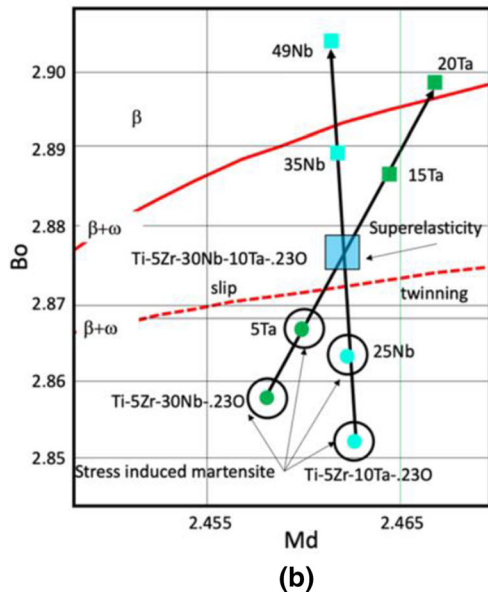


Fig. 10—(a) The B_o - M_d diagram adapted from Ref. [75]. A few illustrative compositions are indicated in the table and numbered in the figure. Modulus domains (GPa) are shown as hatched areas. The red dots are M_d values for the three alloys indicated for their β compositions at 500 °C. The B_o values are indicated within the boxes. (b) The B_o - M_d diagram in the composition region of gum metal adapted from [75]. The $\beta/\beta + \omega$ curve moves from the solid line to the dashed line by alloying with Zr and O, and the nominal gum metal composition is encircled by the large square. (c) The B_o - M_d diagram in the composition domain of some TRIP-TWIP alloys, adapted from Ref. [72] with permission. The arrows indicate alloying vectors of B_o - M_d values on the diagram with Mo and W additions to Ti. The green hatched region indicates a domain of ternary Ti-Mo-W alloys where TRIP/TWIP effects may be observed, and the dashed line indicates compositions where both effects may be simultaneously seen (Color figure online).

α phase. The composition of the α phase in dual-phase engineering alloys of titanium is such that precipitation of α_2 can occur (Figure 1(c)). The solvus for α_2 is between 550 °C and 600 °C for Ti-6Al-4V, about 650 °C for Ti-6242 and about 750 °C for IMI834.^[2] This phase precipitates for prolonged ageing treatments at low temperatures^[62–64] or low cooling rates.^[65] A slight

reduction in the c/a ratio and a noticeable increase in Young's modulus have been reported during ageing below these temperatures.^[66,67] It was found that the basal/prismatic CRSS ratio increases with longer ageing treatments.^[68] The change in values for Ti-6Al-4V with a bi-modal microstructure after 840 hour heat treatment at 500 °C is shown in Figure 8(c). For such ageing

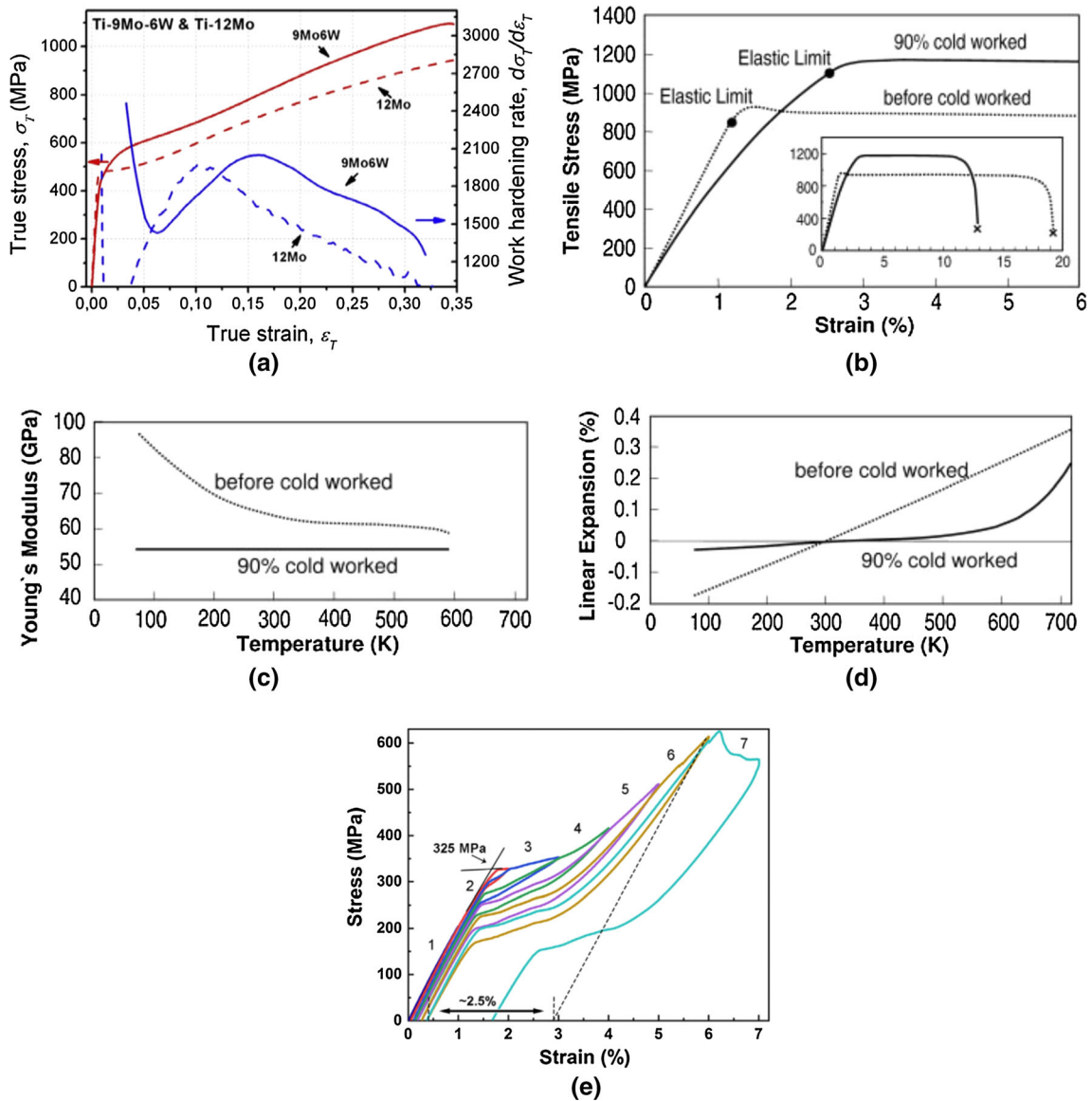


Fig. 11—(a) Stress-strain behaviour in the TRIP-TWIP domain (reprinted with permission from Ref. [72]), (b) stress-strain behaviour of gum metal and the (c) elinvar and (d) invar effects. (b) to (d) reprinted with permission from Ref. [73], (e) strain reversal arising from an ω transformation (reprinted with permission from Ref. [88]).

conditions, basal and prismatic slip activation proceeds at similar applied stress levels in contrast with the as-received material which shows basal slip activity first.^[68] A potential explanation for this could be elemental partitioning between the α and α_2 phases.^[62] A lower Al content is found in the α phase, where dislocations would be expected to be emitted, which favors the operation of prismatic slip over basal slip. The change in slip activation kinetics due to the ageing treatment contributes to a modified stress-strain curve with a sharper transition between elasticity and plasticity, a reduced hardening rate and a lower ductility.^[68] also promoted by increased slip planarity and enhanced slip localization.

IV. PLASTICITY IN THE β PHASE

A. Elasticity in the β Phase

A realistic and accurate simulation of the experimental elastic deformation behavior of the β phase is more difficult than for the α phase. Numerous sets of elastic constants have been reported, but a large scatter in the values exists. This is illustrated in Table III where a selection of elastic constants at room temperature for the β phase is presented. The Zener anisotropy ratio (A) was calculated for each dataset and also reveals a substantial scatter as it ranges from 0.2 to 8.3. Thus, the elastic deformation behavior of the β phase shows a marked sensitivity to the composition.

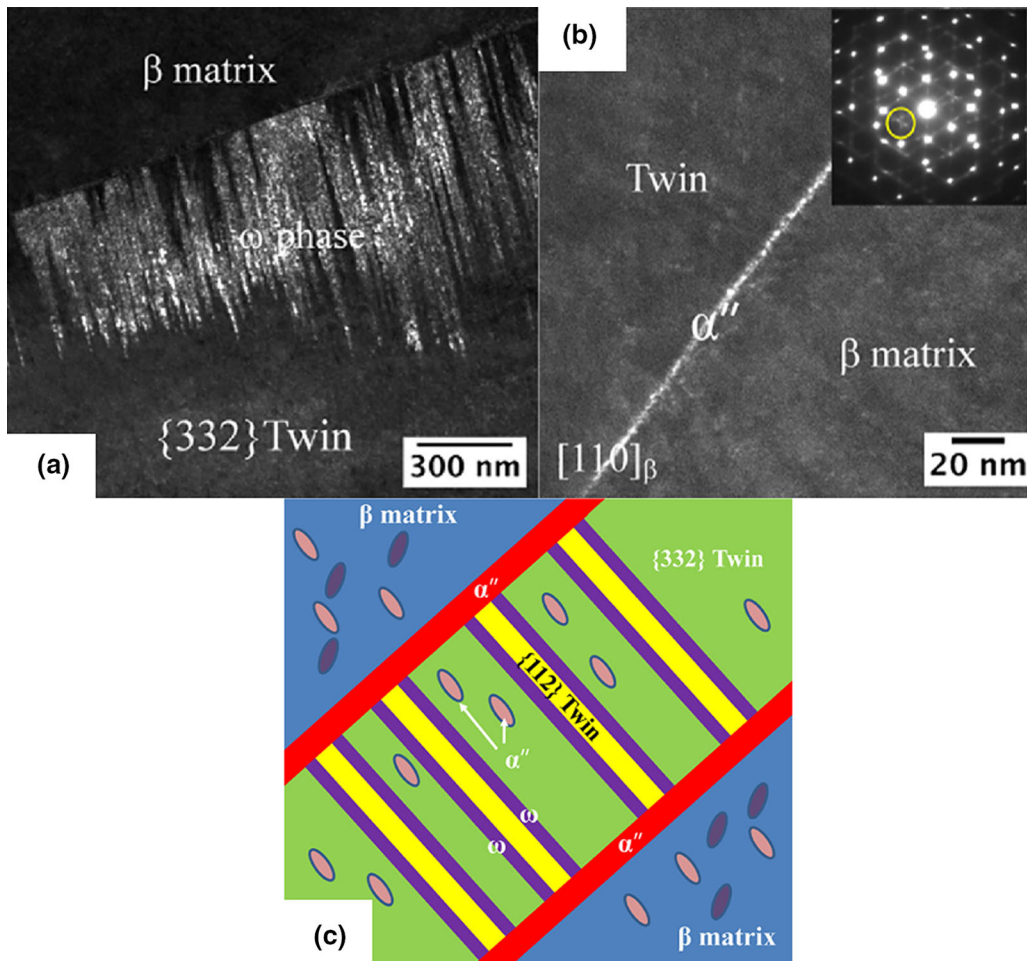


Fig. 12—Substructure of primary $\{332\}\langle 113 \rangle_{\beta}$ deformation twin in 5 pct cold rolled Ti-24Nb-4Zr-8Sn showing the complexity of stress induced products in β phase deformation: (a) Dark field image showing secondary $\{112\}\langle 111 \rangle_{\beta}$ deformation twin and ω phase in the interior of primary $\{332\}\langle 113 \rangle_{\beta}$ twin, (b) diffraction contrast dark field image showing a thin layer of stress induced α'' martensite and (c) schematic drawing showing the four different deformation modes activated (reprinted with permission from Ref. [76]).

Certainly in part this is due to various nanoscale instabilities that exist and are strongly composition dependent as described in the previous section. This significantly complicates the characterization and the simulation of the elastic behavior as the composition of the β phase differs significantly from the average composition due to elemental partitioning. As a consequence, inverse methods are often employed to extract the elastic deformation behavior for each phase but the composition of the β phase is rarely available with reliability as the small dimensions of residual β make it difficult to characterize. Therefore, extrapolation to new alloys is difficult with the current state of understanding. More importantly, a significant scatter even exists for a given alloy and renders difficult the choice of a dataset as well. This lack of confidence into the β elastic constants to be employed for various alloy compositions and processing history presents a serious challenge in the simulation of the behavior of dual phase structures and represents a major limitation to overcome in the future.

B. Deformation Modes

The β can be retained at room temperature by quenching from the single phase region if the M_s temperature is below room temperature (Figure 1(b)). The shape memory effect arising from the martensitic transformation in this class of titanium alloys has been described for example in References 69, 70. Both twinning induced plasticity (TWIP) and transformation induced plasticity (TRIP) have been explored recently in the design of high strength, high work hardening alloys.^[71,72] The unique properties of gum metal (Ti-Nb-Ta-Zr-O alloy)^[73] include non-linear superelasticity combined with the invar and elinvar effects. Significant effort has been expended in defining non-toxic Ti alloy compositions with low modulus that are closer that of bone for biomedical application.^[74]

Figure 9 shows schematically possible deformation modes of the β phase, which have been utilized in the studies referred to above. While various stress induced transformations and dislocation-based plasticity can

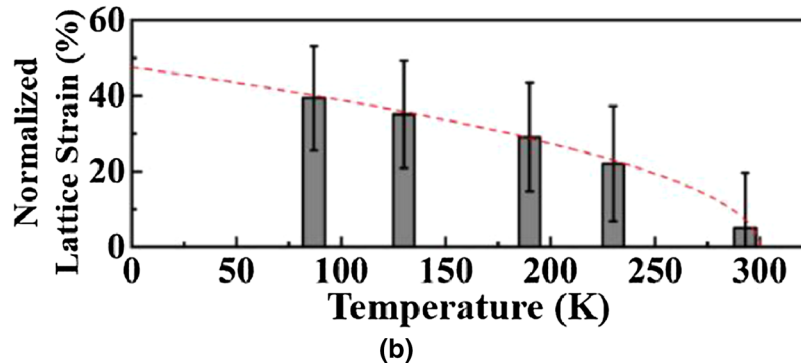
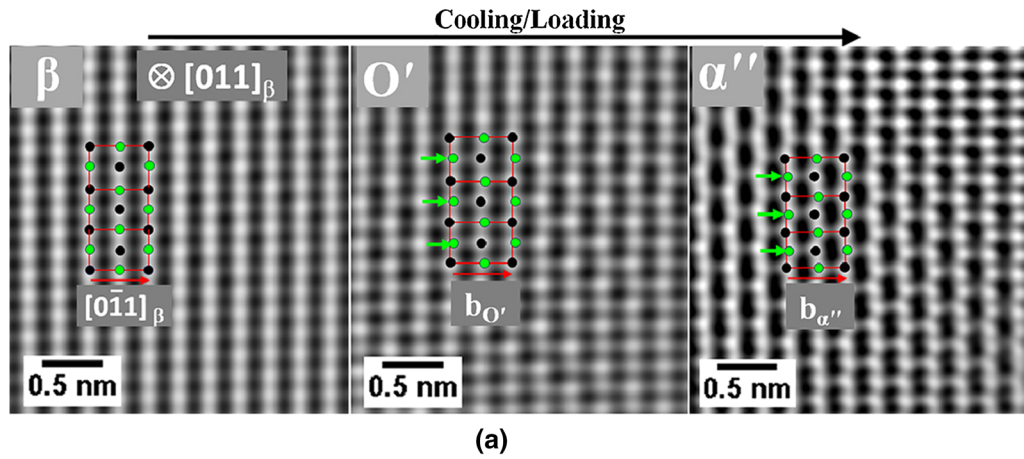


Fig. 13—(a) Nanodomain of orthorhombic α'' formed from O' . (b) The resultant lattice strain as function of temperature (reprinted with permission from Ref. [90]).

overlap, the figure indicates the increasing propensity for each of these modes with increasing β stabilizer content. The presence of the nanoscale, metastable phases O' and ω influences the deformation mode in ways that are far from being completely understood, although there has been an explosion of recent research that explores these effects in relation to mechanical behaviour of β . We offer only a selective summary in this section. The Bo-Md diagram^[75] has provided the basis of classifying deformation response of the metastable β phase in all recent work. Figure 10(a) shows this diagram which is a plot of B_o , the bond order that measures the covalent bond strength between Ti and any other metal, and M_d , the d orbital energy level of the alloying metal. The diagram defines the stability of the martensite and ω phases and also delineates regions of stress induced responses and slip, together with domains of varying modulus. The diagram does not indicate the stability region of the O' phase or the domain over which stress induced ω can form. The anomalous effect of O, Al, Sn (α stabilizers) in suppressing the Ms temperature is also not accounted for as mentioned by the authors. Figures 10(b) and (c) indicate the composition domains for gum metal and TRIP-TWIP effects respectively. The superelastic properties associated with gum metal lie in a Bo-Md region in which the β phase is least stable with respect to athermal omega, and in principle deforms by slip. Figure 10(b)

also indicates how the boundary between the β and $\beta + \omega$ region shifts, as experimentally observed, with the addition of oxygen. The stress strain curves associated with these effects are shown in Figure 11 and the current understanding of gum behaviour is described later in this section. The TRIP-TWIP response lies in a Bo-Md region which in which $\beta +$ athermal ω occurs on quenching, as shown in Figure 10(c), and results in a plateau in these stress-strain curves that does not appear in gum metal (Figure 11(a)). The variety and complexity of stress induced response that emerges in the magnified region of the diagram illustrated in Figure 10(c) is described for example in References 76, 77 and illustrated in Figure 12. Intricate patterns of $\{332\}\langle 11\bar{3}\rangle$ and $\{111\}\langle \bar{1}\bar{1}2\rangle$ twins along with stress induced ω and α'' appear and evolve with strain in a manner that remains incompletely understood.

The presence of athermal or isothermal ω mediates the stress induced response in complex ways. Beyond the composition regime at room temperature at which stress induced martensite forms, the stability of the ω phase appears to dictate whether twinning or slip occurs. Hanada and coworkers in the eighties^[78–80] described athermal ω in terms of the extent of collapse of the $\{111\}$ planes of β and related the reciprocal spacing ratio $d_{0002}^* \omega / d_{222}^* \beta$ to this displacement. The hexagonal ω forms at the ideal ratio of 0.667 and it was observed that stress induced ω forms at that β

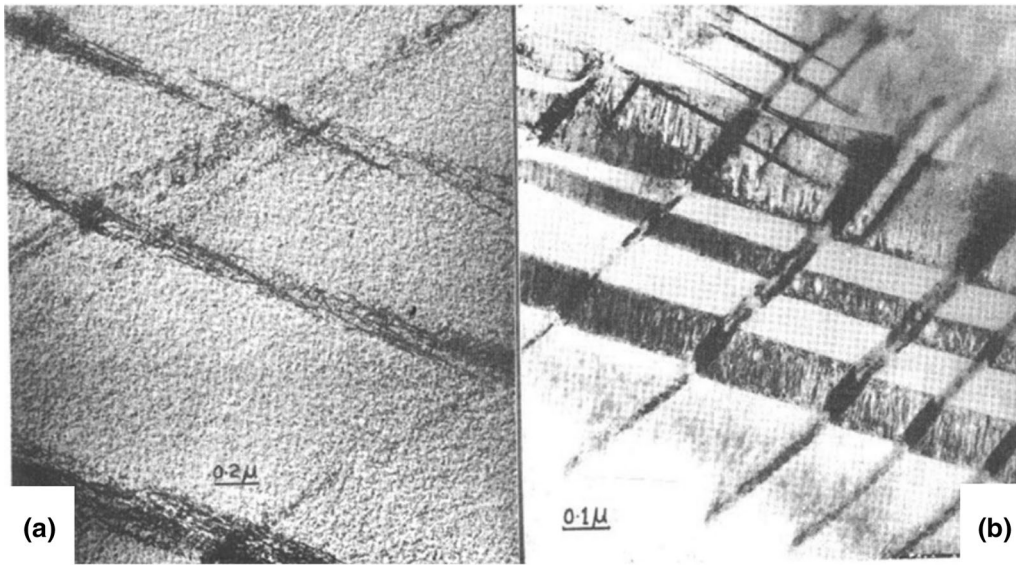


Fig. 14—Slip and twinning in a Ti-15V-3Al-3 Cr-3Sn alloy deformed at (a) room temperature and (b) 83 K, respectively (reprinted with permission from Ref. [1]).

Table IV. CRSS Values for Slip Systems of the β Phase with the Associated CRSS for Prismatic Slip in the α Phase

Alloy	{110}<111> CRSS (MPa)	{112}<111> CRSS (MPa)	{123}<111> CRSS (MPa)	Prismatic α CRSS (MPa)	References
Ti-6242	250	210–230	201–251	240	[110]
Ti-6242	435–534	395–534	386–534	356–394	[141]
Ti-6242	240	X	X	280	[111]
Ti-6Al-4V	290	310	350	350	[231]
Ti-6Al-4V	360	365	370	320	[26]
Ti-6Al-4V	387	387	387	410	[26]

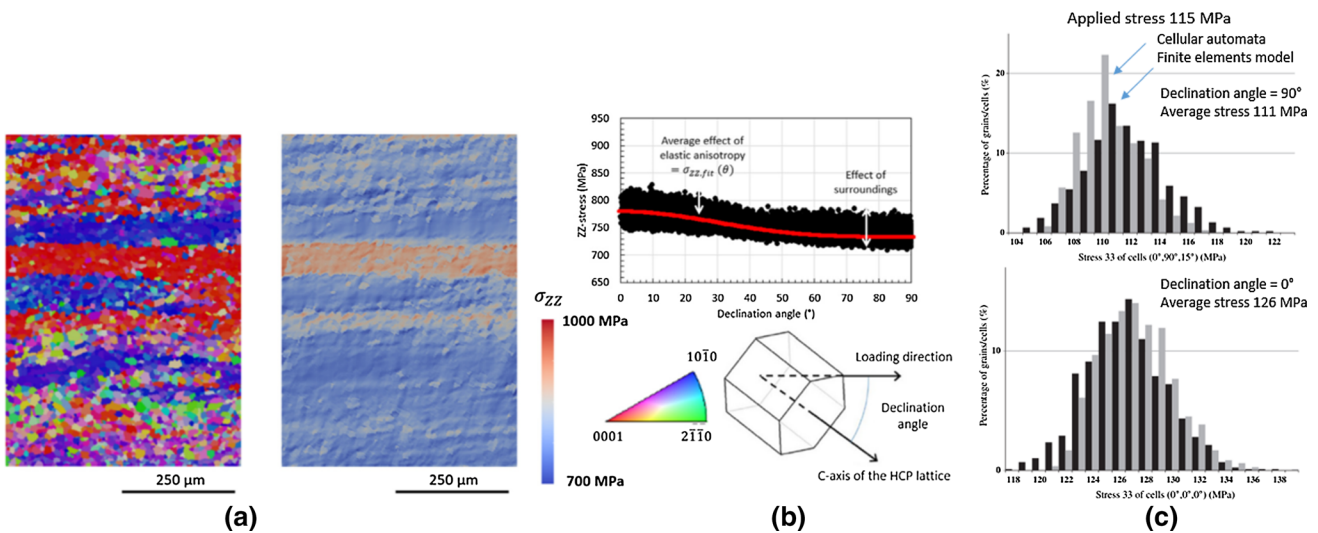


Fig. 15—(a) Crystallographic orientation along the loading direction and the corresponding stress magnitude along the loading direction as calculated using fast-Fourier transforms (b) The grain averaged stress magnitude is plotted against the declination angle from the c -axis (reprinted with permission from Ref. [99]), and (c) Stress scatter for two different orientations as calculated using finite element modeling and cellular automata (reprinted with permission from Ref. [104]).

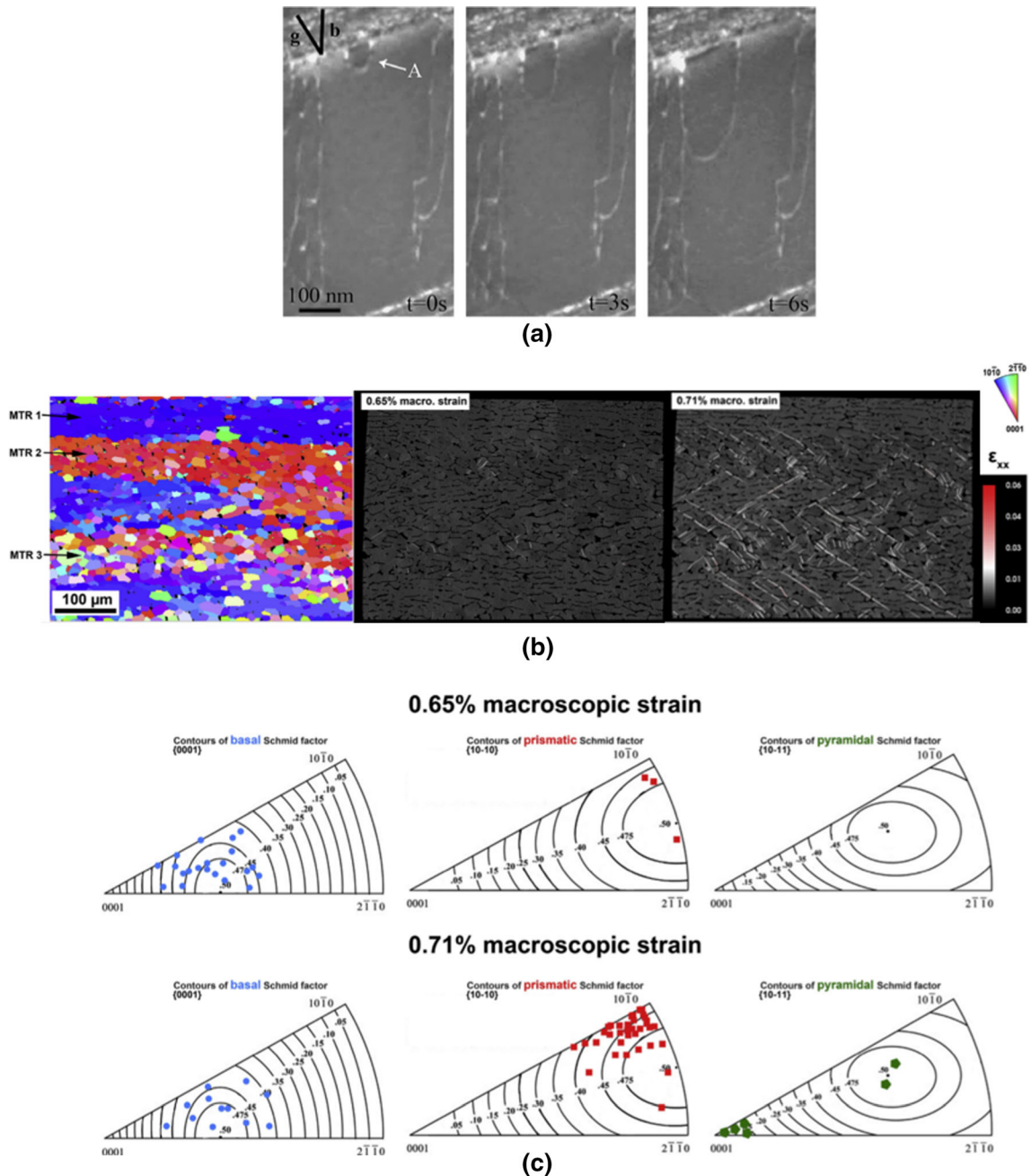


Fig. 16—(a) *In situ* TEM observation of dislocation loop emission from an α/β interface in Ti-6Al-4V with a bi-modal microstructure (reprinted with permission from Ref. [109]), (b) crystallographic orientation along the loading direction and sub-grain scale strain maps at two different loading steps in Ti-6Al-4V with an equiaxed microstructure, and (c) crystallographic orientation along the loading direction of α grains from (b) with basal (in blue), prismatic (in red) or pyramidal (in green) slip activity (reprinted with permission from Ref. [115]) (Color figure online).

composition in which ω has the hexagonal symmetry. At β stabilizer contents beyond this value, the ratio decreases such that the partial displacement leads to ω with trigonal symmetry and under these conditions $\{332\}\langle 11\bar{3}\rangle$ twinning is observed. Slip occurs at values less than 0.662 irrespective of the alloy content. Alternative hypothesis have also been proposed for the origin of $\{332\}\langle 11\bar{3}\rangle$ twinning. It has been suggested that the $\{110\}\langle 110\rangle$ shuffles associated with the O' phase will promote $\{332\}\langle 11\bar{3}\rangle$ twinning over $\{111\}\langle \bar{1}\bar{1}2\rangle$ twinning.^[81] In alloys containing athermal

or isothermal ω , a transition from twinning to slip can occur and a variety of possibilities ranging from ω size to composition partitioning on aging and the structure of the aged ω have been proposed to explain this transition.^[82–84] The transition is important since high strengths with ductility can be obtained in ω containing β phase when twinning is the major deformation mode.^[85,86] The embrittling effect of ω induced intense slip planarity, when deformation is carried by dislocations, has been known for a long time.^[87] It has also been shown very recently that the omega

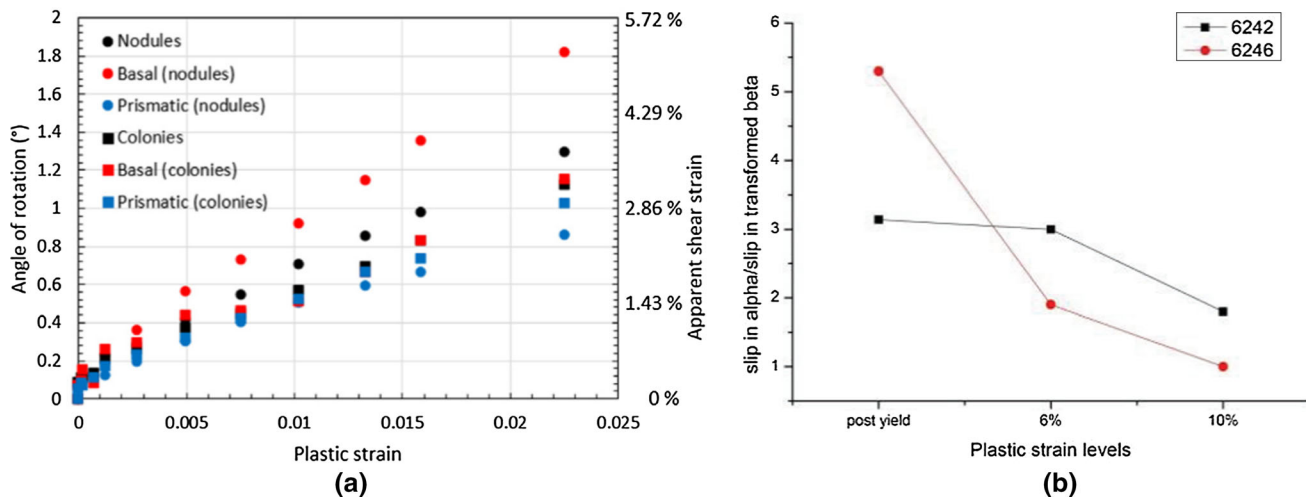


Fig. 17—(a) Grain averaged apparent shear strain depending on the microstructural elements and active slip systems in Ti-6Al-4V with a bi-modal microstructure (reprinted with permission from Ref. [113]). (b) The ratio of slip in equiaxed α and transformed β in bimodal structures of Ti6242 and Ti6246 (reprinted with permission from Ref. [122]).

transformation can also be associated with significant strain reversibility^[88] (Figure 11(e)).

A unique nano strain mode akin to strain glass formation has also been detected in metastable β alloys containing the O' phase. The martensitic transformation in titanium alloys has two distinct mechanistic steps, a $\{112\}\{111\}$ shear that is associated with the Bain strain that transforms the bcc lattice to a hexagonal lattice and a $\{110\}\{110\}$ displacement or shuffle on every alternate $\{110\}$ plane to realise the ABAB stacking of the hexagonal α' martensite. The orthorhombic α'' martensite represent an intermediate extent of shear and shuffle. The Bain shear is associated with the activation energy of transformation that leads to the plate of martensite, once the nucleation barrier is overcome, with its associated macroscopic long-range shape strain. In high resolution TEM observations of the O' phase^[3] it was noted that the structure of this phase could be explained by purely the $\{110\}\{110\}$ displacement if this instability preceded the Bain strain. Thus the O' phase contains one component of the martensitic transformation and serves as nucleus for the martensite. It has recently been seen^[89,90] that cooling a structure with nano domains of the O' phase leads to a continuous increase in both the shear component and shuffle displacement within the domains leading to a nano distribution of the α'' martensite (Figure 13). This has all the characteristics of a 'strain glass' transformation in which nano domains of localised strain order form in a continuous manner with stress or temperature changes and can lead to phenomena such as superelasticity or the invar or elinvar effects.^[89] Indeed, such a stress/temperature induced continuous nanotransformation serves as template for gum-metal like behaviour that is discussed below.

Gum metal compositions, which are based on Nb, Ta, Zr and O additions to Ti (Figure 10(b)), in contrast to those that exhibit stress induced transformation products, appear to lie in a domain that would favor slip (Figure 10(c)), and are coupled with Bo-Md

combinations that promote a low modulus. Indeed, tensile deformation of such compositions show no indicators of stress induced products (Figure 10(b)) such as a stress plateau. As quenched gum metal compositions appear to be free of athermal ω ,^[91,92] also in accordance with Figure 10(b). The remarkable properties of gum metal develop only after heavy cold work (Figures 11(c), (d)). Giant faults are observed in the worked material, that were in the first instance attributed to dislocation free shearing suggested to operate at the near ideal shear strength of the material.^[73,93] Subsequently a variety of stress induced products have been observed in heavily worked materials that include $\{111\}\langle\bar{1}\bar{1}2\rangle$ twinning that has been directly related to the faulted bands,^[94,95] stress induced omega formation and O' .^[90,93] It has been shown that tensile deformation of heavily worked material results in reversible α'' formation through *in-situ* synchrotron radiation.^[94] These observations are not inconsistent with the observations of a strain glass effect described earlier.

Oxygen plays a critical role in controlling β phase stability and suppresses athermal martensite and ω formation, as does Al, Sn and Zr to various extents. It has been speculated that all these elements promote the $\{110\}\{110\}$ shuffle, that arises from a softening of c' or $(c_{11}-c_{12})/2$ with decreasing temperature, and thus the O' phase,^[3,96] although it has been established that O' formation occurs in binary as well as very low O alloys.^[97]

Beyond the β stabilizer levels at which these effects are observed, the β phase deforms by $\langle 111 \rangle$ slip predominantly on $\{112\}$ planes. Unusually for bcc metals slip is planar as shown in Figure 14 and the origin of planarity is not clear. The same alloy deformed at lower temperatures shows twinning due to either ω or O' formation. In an *in situ* investigation of $\langle 111 \rangle$ glide it has been shown that screw dislocations as in other bcc materials have a low mobility.^[98] Of interest is the stability of the retained β compositions in engineering titanium alloys

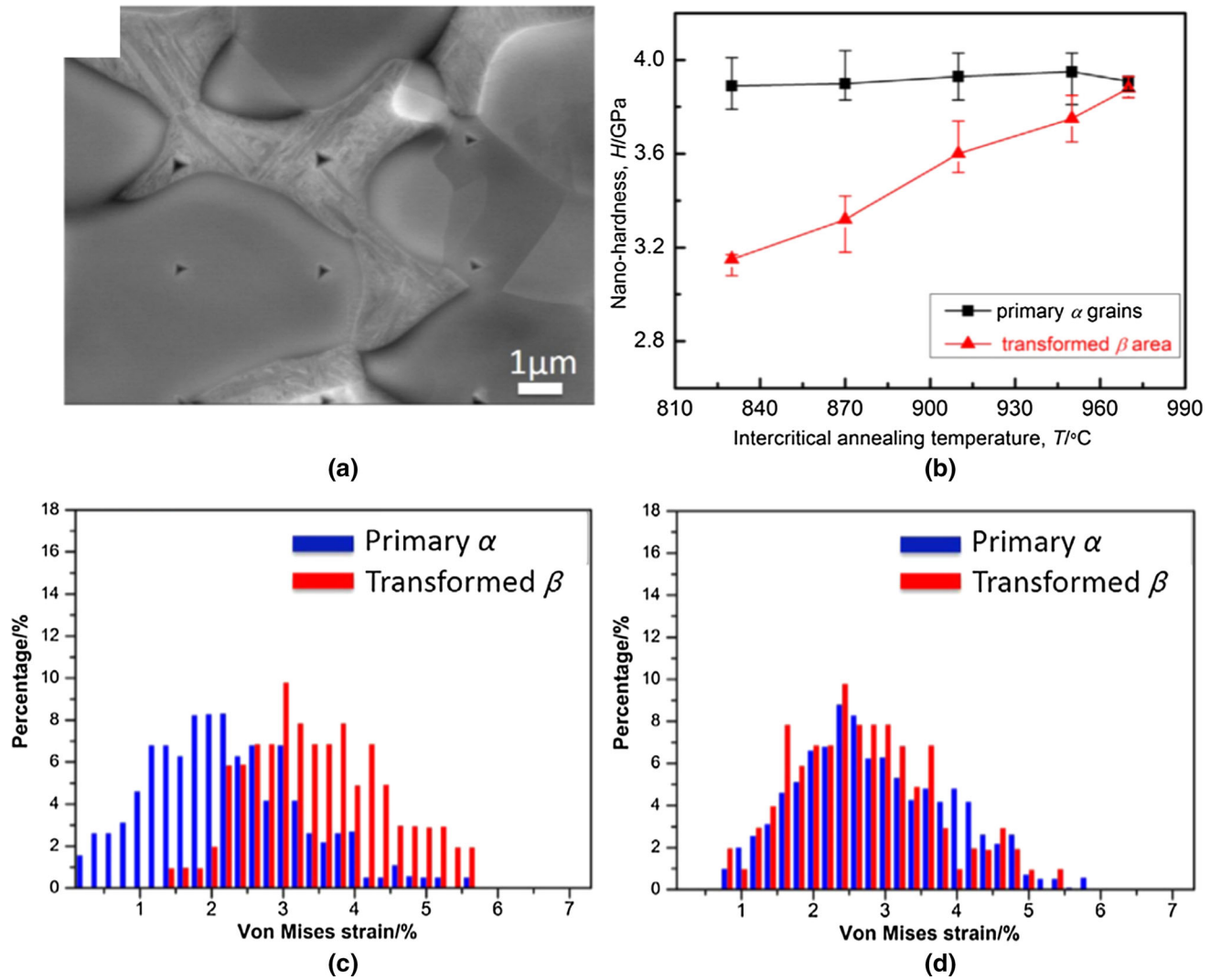


Fig. 18—(a) Nano-hardness indents in bimodal structure of Ti-6Al-4V, (b) average nano-hardness plotted as a function of the sub transus annealing temperature (c) and (d) show the partitioning of strain in equiaxed α and transformed β at two annealing temperatures corresponding to 870 °C and 950 °C (reprinted with permission from Ref. [124]).

heat treated in the 2-phase region. The B_0 / M_d values for the retained beta phase derived from ThermoCalc calculated compositions (The β composition of Ti64 is approximately Ti-50 wt pctV, that of Ti1023 is Ti-30 wt pctV-6 wt pctFe while that of Ti5553 is Ti-15 wt pctMo-15 wt pctV-8 wt pctCr-1 wt pctFe) at 500 °C for some typical alloys are shown as red circles in Figure 10(a) and their values indicate that these retained β compositions should deform by slip.

C. CRSS of the β Phase

Experimental data related to CRSS of β phase are scarcer than for the α phase. Numerous challenges are associated with the characterization of the deformation behavior of this phase for $\alpha + \beta$ alloys such as Ti-6Al-4V or Ti-6242. The small size of the ligaments that are present between α grains or α plates also leads to difficulties in the characterization of the mechanical response and the low β volume fraction leads to a weak

sensitivity of the overall response to its behavior. Several CRSS datasets available in the literature are given in Table IV. bcc metals exhibit tension-compression asymmetry on slip modes other than $\{110\}\{111\}$. The data in Table IV indicates that slip strength in the β phase is roughly similar to the prismatic slip strength in the α phase. We note that the β phase is more compliant than the α phase. As a consequence, the stress experienced by the β phase is, in average, lower than the one experienced by the α phase for a given strain state.

It is quite evident that much remains to be understood in evaluating β phase dislocation or transformation-induced plasticity. There are sometimes contradicting descriptions of the same compositions. Complicating the picture is the difficulty of homogenisation of alloy composition gradients arising from solidification induced microsegregation of slow diffusing species, and the lack of attention to various possible thin foil artefacts in TEM characterisation that includes stress relaxation in thin foils (particularly important in the

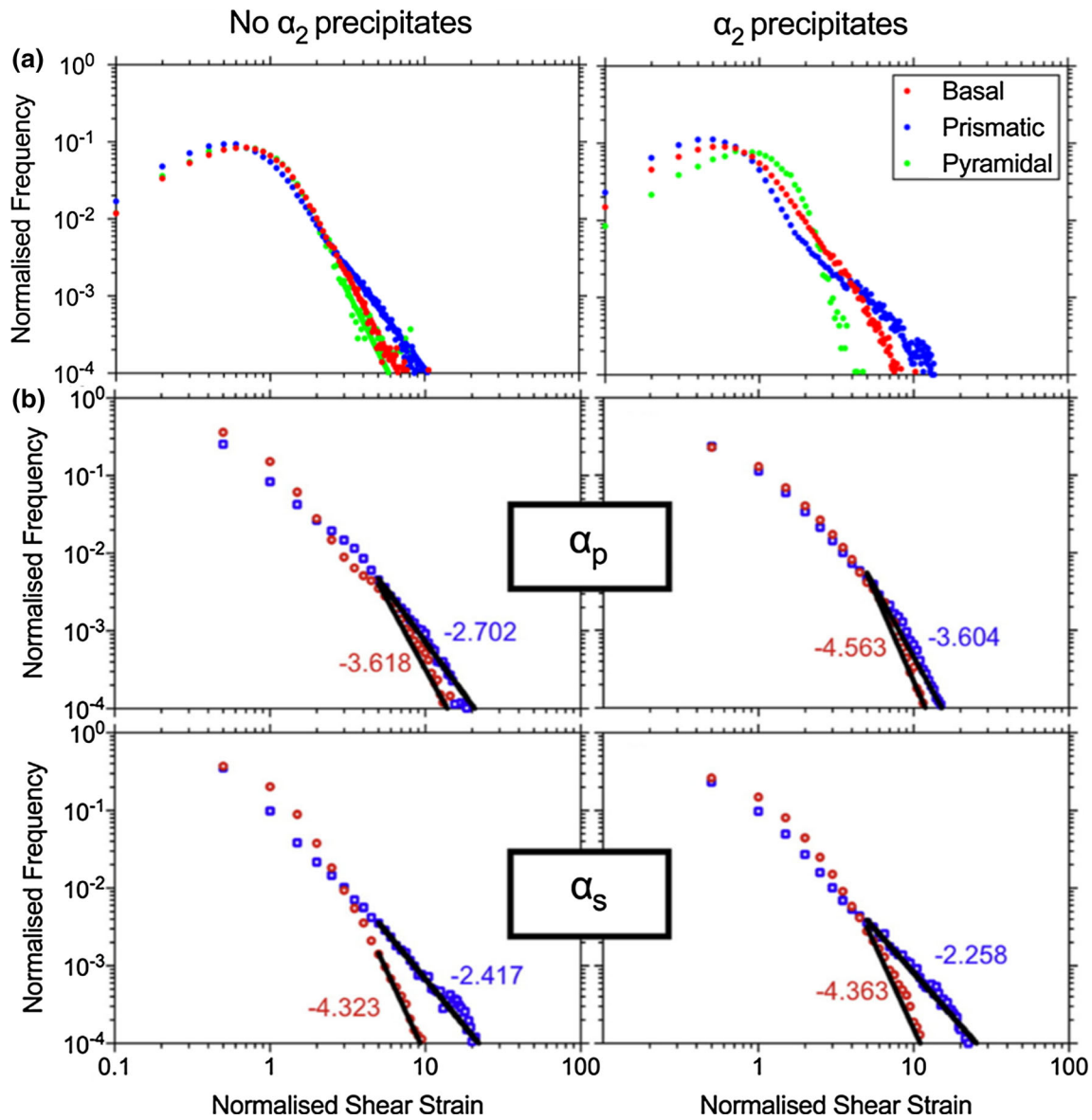


Fig. 19—(a) Normalized frequency vs. normalized shear strain showing slip intensity for basal, prismatic and pyramidal slip systems in equiaxed α in Ti-6Al-4V (reprinted with permission from Ref. [114]), (b) normalized shear strain showing the more pronounced strain localization in transformed β regions, especially after ageing to promote α_2 formation. The numbers indicate the slopes as indicators of strain localization (reprinted from Ref. [126] under the terms of the Creative Commons BY 4.0).

situation where stress induced products are being analysed), foil preparation by electropolishing that is carried out at sub-zero temperatures (in the situation that β phase stability changes with temperature) and well known H ingress during electropolishing and its effect on phase stability.

V. MICROPLASTICITY IN DUAL PHASE STRUCTURES AND SLIP TRANSFER PROCESSES

A. Elasticity and Incipient Slip

The α phase exhibits anisotropic elastic behavior with declination from the c -axis but is isotropic in directions

perpendicular to the c -axis. Therefore stress heterogeneities are expected within polycrystalline α loaded in the elastic regime. The stress experienced by a given grain embedded in a polycrystalline aggregate depends on its own orientation among other factors such as its neighborhood. This is illustrated for a significant number of grains in Figure 15 taken from Reference 99. The elastic constants from Reference 23 were used in the simulations. In average, the stress is higher for grains with their c -axis well aligned with the loading axis, which are well oriented for $(c + a)$ pyramidal slip or twinning, and lower for grains with their c -axis normal to the loading axis, which are well oriented for prismatic slip. Grains well oriented for basal slip experience an intermediate stress state. However, the difference in average stress magnitude between stiff and compliant

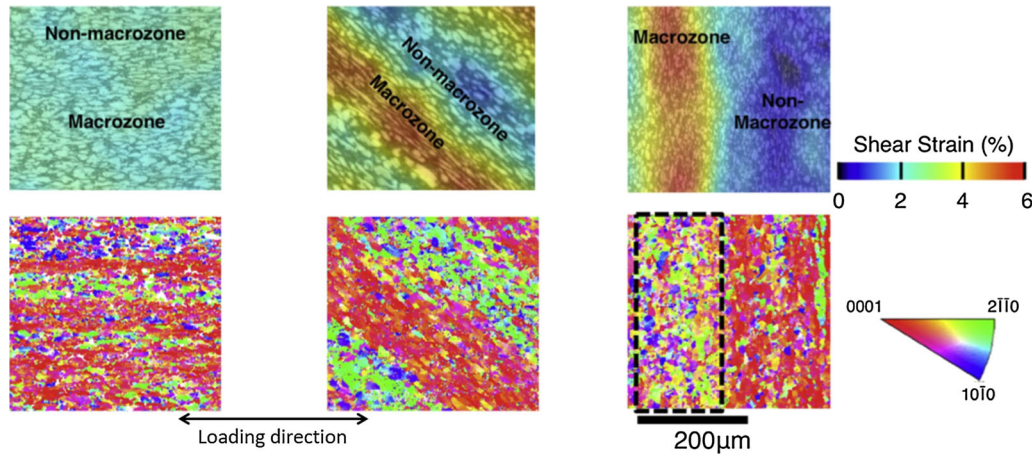


Fig. 20—Shear strain maps with the crystallographic orientation indicated showing strain heterogeneity in relation to MTRs (reprinted with permission from Ref. [132]).

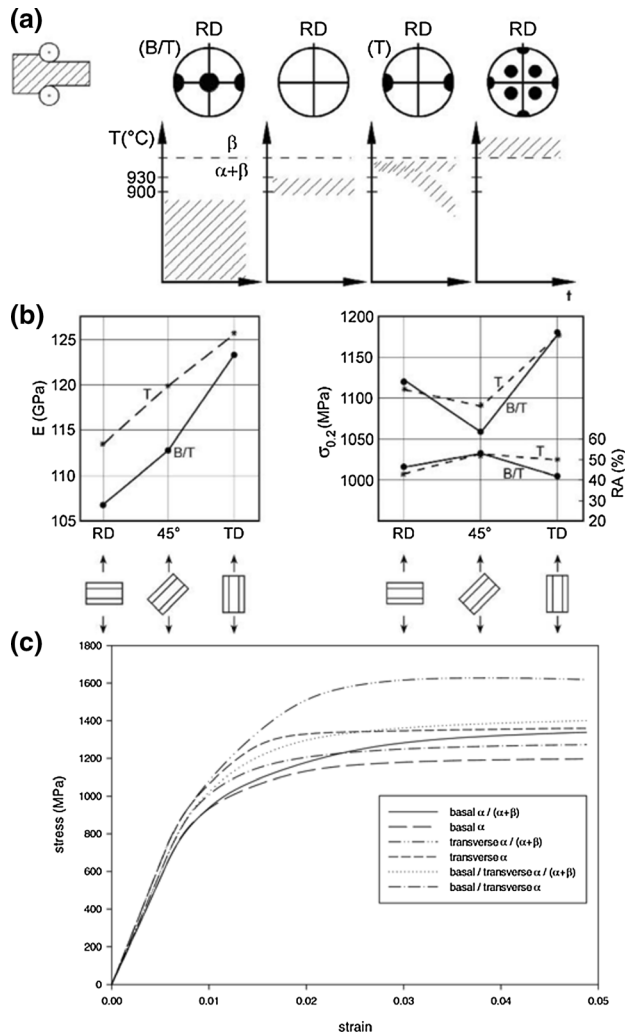


Fig. 21—(a) Schematic representation of basal and basal/transverse textures commonly obtained is shown in (0001) pole figures (reprinted with permission from Ref. [2]), (b) influence of loading direction on the tensile behavior of Ti-6Al-4V with a transverse (T) or basal transverse (B/T) textures (reprinted with permission from Ref. [2]), (c) stress–strain curves depending on the texture and the microstructure (equiaxed/bi-modal) of a Ti-6Al-4V alloy (reprinted with permission from Ref. [134]).

orientations is roughly in the 10 percent range for uniaxial loading.^[100] As a consequence, a fair insight into activation of different slip modes can be obtained simply considering the magnitude of the CRSS. For instance, in commercial Ti alloys with about 6 wt pct Al, pyramidal slip modes are activated after basal and prismatic slip. However, if the difference in slip strength is more subtle, such as for basal and prismatic slip,^[100–103] the higher stress experienced in average by grains well oriented for basal slip contributes to the experimental observation of basal slip activity at lower applied stress than prismatic slip.^[57,58]

However, one has to keep in mind that CRSS estimation from polycrystalline samples is dependent on the elastic constants used to account for elastic anisotropy. From the plot of Figure 15(b), one can also extract the typical scatter due to the grain neighborhood in the elastic regime. Such scatter is also illustrated in Figure 15(c). It is within ± 10 pct of the applied stress.^[99,104] The limited effect of elastic anisotropy previously discussed is consistent with the proper description of slip activation using a global stress state.^[105]

Elastic interactions between α and β phases are believed to influence the initiation of slip at phase interfaces according to the studies performed by Ankem and Margolin.^[106] Less apparent structural units at different length scales such as MTRs or beta grains also significantly influence the onset of slip activity. The effect of MTRs is further discussed in the following sections. In metastable β alloys such as Ti5553, the crystallographic orientation of the β matrix has a major effect on slip initiation in the α phase through generating a heterogeneous stress field in relation with the β grain orientation. In particular, slip activity appears difficult in grains oriented with a $\langle 111 \rangle$ direction aligned with the loading axis.^[59] As a consequence, the study of plasticity in relation to mechanical fields in metastable β alloys such as Ti5553 or Ti1023, where the β grain size is in the millimeter range and lamellas are a few tens of

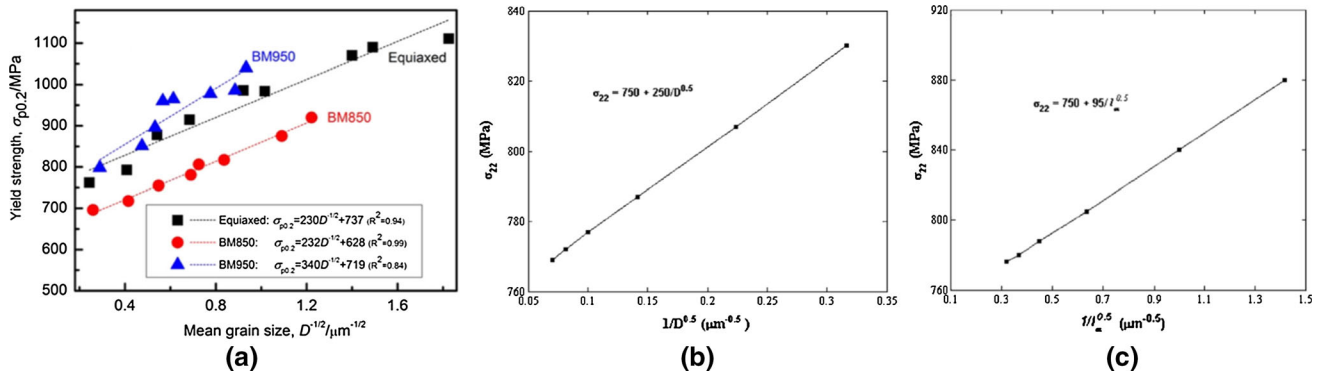


Fig. 2—(a) Grain size dependence of the yield strengths for Ti-6Al-4V with equiaxed or bi-modal microstructure with different transformed β fractions from experiments (reprinted with permission from Ref. [140]), (b) from crystal plasticity simulations considering Ti-6242 with a bimodal microstructure (reprinted with permission from Ref. [141]), (c) lath thickness dependence of the yield strength from crystal plasticity simulations considering Ti-6242 with a lamellar microstructure (reprinted with permission from Ref. [141]).

nanometers thick, is a significant challenge. Indeed, these different length scales have to be carefully considered.

B. Slip Initiation

According to *in situ* TEM investigations carried out on tension tested Ti-6Al-4V with a bi-modal microstructure, plasticity begins in the α phase with dislocations emitted from α/β interfaces in lamellar regions^[107] while intragranular sources were observed to generate dislocations in equiaxed α .^[108] The emission of a dislocation loop from an α/β interface is shown in Figure 16(a). In such microstructures, the first slip bands are usually observed in the primary α phase.^[57,68,105] The α phase deformation is mainly controlled by screw segment movements of $\langle a \rangle$ -type dislocations.^[109] As discussed previously, it is interesting that several studies reported a slip strength in the β phase which is close to that of the α phase.^[26,110,111] Size effects are then expected to play a major role on the plasticity development in relation to microstructure. As the β phase is finely distributed in typical dual phase structures of $\alpha + \beta$ alloys such as Ti-6Al-4V, the strength of the α phase may be lower than that of β .

Multiple slip modes were found to be active in the micro-plasticity regime of $\alpha + \beta$ polycrystalline Ti alloys. Basal slip was observed to be activated first in 6 weight pct Ti alloys such as Ti-6Al-4V, Ti-6Al-2Sn-4Zr-2Mo and Ti-6Al-2Sn-4Zr-6Mo.^[57,58,68,112] Prismatic slip emerges next, still below the 0.2 pct proof stress. This is illustrated in Figures 16(b) and (c) where the orientation and strain dependence in the incipient slip regime of various slip systems is shown. This feature can, at least partially, explain the higher plastic strain experienced in average in α grains where basal slip operates in comparison to α grains where prismatic slip operates.^[113] In addition, Lunt *et al.* showed that prismatic slip seems associated with more intense strain localization than basal slip.^[114] Basal and prismatic slip modes are found active in distinct crystallographic orientation domains that favor a high resolved shear stress. Considering a global stress state, the resolved shear stress for

basal slip is maximum with a misorientation of 45 deg between the loading and the c-axes. Experimental data and local stress calculations including elastic anisotropy show values slightly lower than 45 deg. In contrast, the resolved shear stress for prismatic slip is maximum with a misorientation of 90 deg between the loading and the c-axes. As a consequence, no competition between these slip systems is observed at low strain.^[58] The operation of pyramidal $\langle a \rangle$ and $\langle c + a \rangle$ slip was also reported at higher applied stress values.^[105,115] It is worth mentioning that their activity is usually associated to a restricted number of occurrences below the 0.2 pct proof stress of the material. Pyramidal $\langle a \rangle$ slip was observed to result from cross slip from basal or prismatic planes.^[108] The operation of $\langle c + a \rangle$ pyramidal slip has been frequently observed in grains with their c-axis well aligned with the loading direction. Since $\langle c + a \rangle$ pyramidal slip or twinning is essential to accommodate c-axis deformation, these deformation modes play an important role. While twinning is inhibited by the high aluminum content occasional occurrences were found under cyclic loading at relatively low plastic strain (*i.e.*, 2.5 pct).^[116] In this case, $\{1012\}\langle 10\bar{1}1 \rangle$ tension twins were observed and operate concurrently with $\langle c + a \rangle$ pyramidal slip. While pyramidal slip traces extend across the whole grain, the twins are generally much smaller and accommodate intergranular deformation incompatibilities due to heterogeneous slip activity. The occurrence of twinning was also reported in Ti-6Al-4V submitted to quasi-static tension for higher amounts of plastic strain.^[117]

1. Microscale strain rate sensitivity

Most of the data previously presented has been gathered with low strain rate or so-called quasi-static strain rate tests. However, Ti alloys are well known to exhibit strain rate sensitive deformation behavior. The rate sensitivity associated with each slip mode is not well known although it is clearly identified as a key parameter for modeling of dwell-fatigue for instance.^[118] Hence, it has attracted a lot of interest in the recent years, especially for basal and prismatic slip that are the main deformation modes. An anisotropy in strain rate

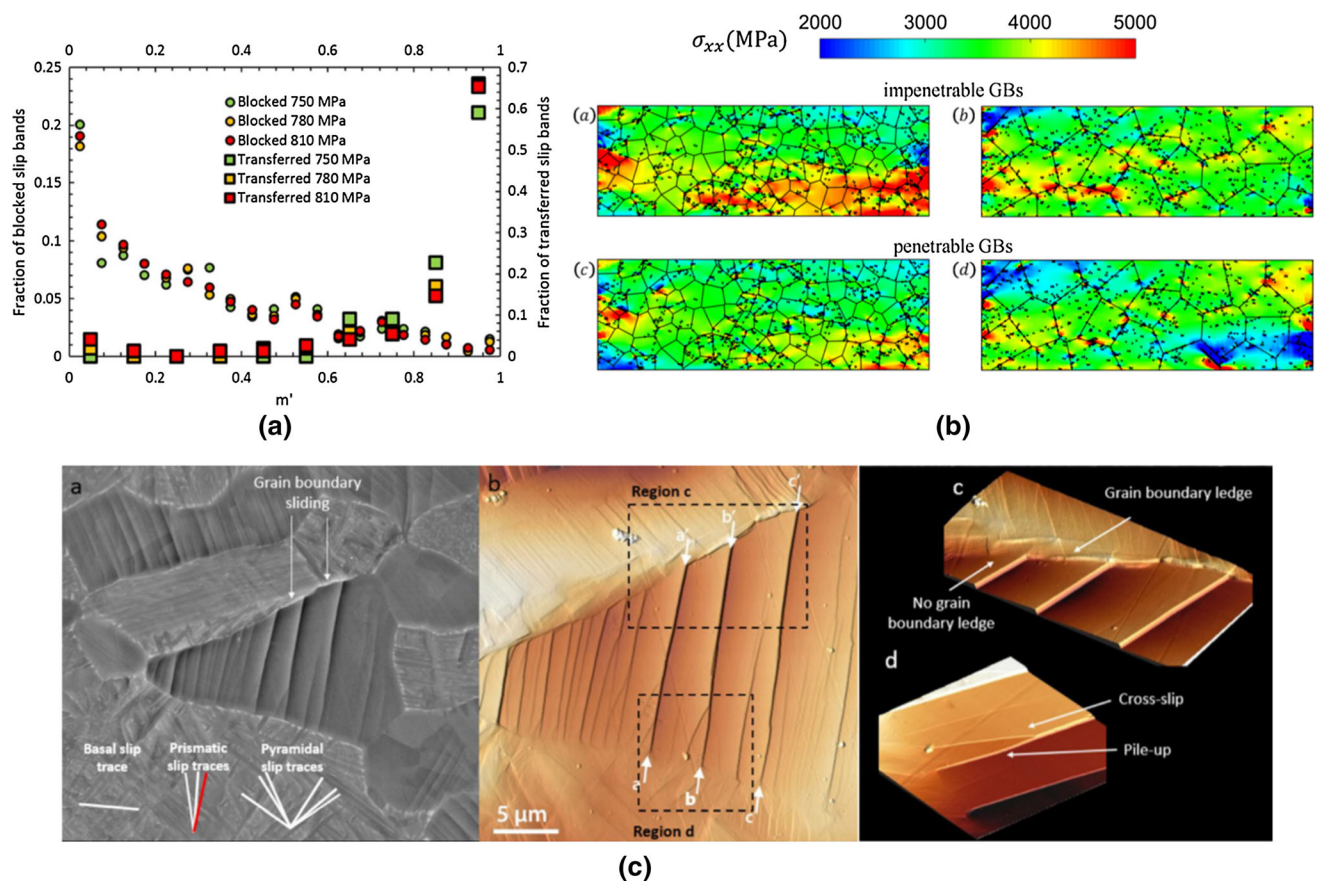


Fig. 23—(a) m' distribution frequency for slip transfer occurrences and blocked slip bands (reprinted with permission from Ref. [133]), (b) stress magnitude along the loading direction for small grains and coarse grains with impenetrable and penetrable grain boundaries (reprinted from Ref. [147] under the terms of the Creative Commons BY 4.0), (c) examples showing the occurrence of grain boundary sliding in Ti-6Al-4V with a bi-modal microstructure (reprinted with permission from Ref. [148]).

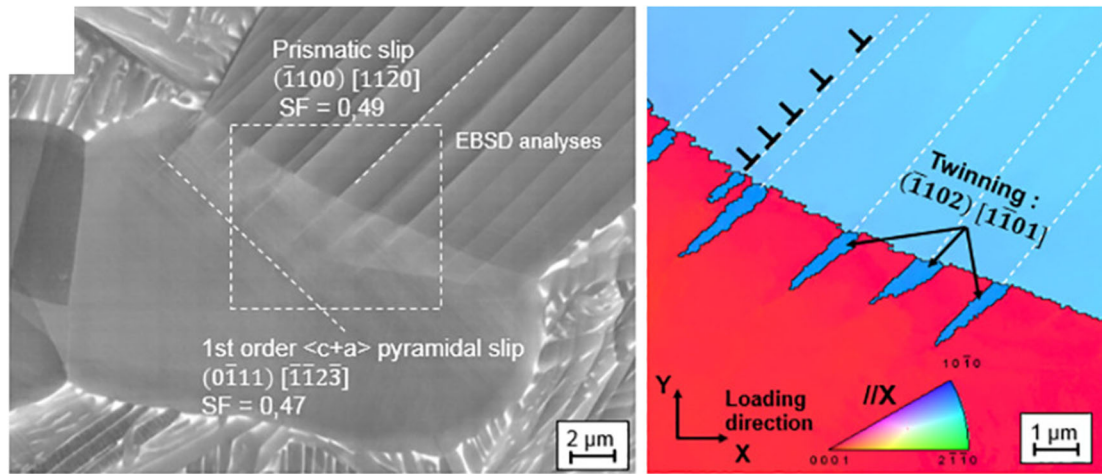
sensitivity (SRS) was first seen using nano-indentation^[119] and then thoroughly characterized using micropillar compression combined with EBSD characterization and crystal plasticity simulations.^[120] Basal slip was shown to be more strain rate sensitive than prismatic slip in compression. A different approach involving far field high energy diffraction microscopy was also applied on Ti-7 pctAl tested in tension. SRS of 0.02 and 0.04 were reported for basal and prismatic slip systems.^[121] The origin of these different trends is not clear yet in spite of a potentially critical role in creep and dwell-fatigue behavior.

2. Slip activity in relation to microstructure and composition

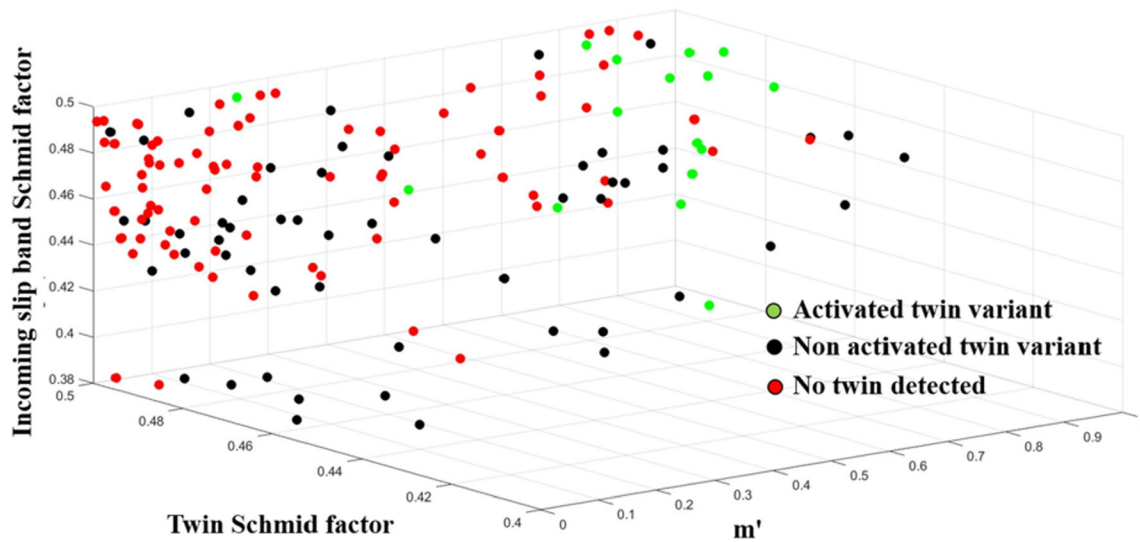
The preceding discussion makes the description of the onset of slip activity straightforward for fully lamellar and equiaxed microstructures. However, strain partitioning is a key phenomenon for the deformation behavior of bi-modal microstructures. In a recent study, lattice rotations were quantified *in situ* using EBSD and linked to the shear magnitude in the different microstructural elements of bi-modal Ti-6Al-4V. It was shown (Figure 17(a)) that nodules experience a higher plastic strain than colonies.^[113] Although not directly comparable, this is consistent with the ratio of

the number of grains in which slip is observed in equiaxed α to that in colonies as a function of strain (Figure 17(b)).^[122] The data suggest that there is a strength differential between equiaxed α and colony structures.

Strain partitioning can be significantly influenced by a variety of other effects, which include the scale and variant distribution characteristics of α laths in the transformed β constituent, the volume fraction and composition of the equiaxed α and transformed β , and the volume fraction of β in the transformed β , as determined by annealing temperatures. The α phase is enriched in α stabilizing elements such as Al, O and Sn upon annealing in the $\alpha + \beta$ domain and may contain Zr, and small amounts of β stabilisers such as V or Mo depending on the alloy chemistry. Elemental partitioning, tailored through carefully designed thermal treatments, was recently demonstrated to significantly influence the strength and local deformation.^[123,124] It is however difficult to decouple solid solution effects and microstructural scale effects that change simultaneously with annealing treatment. An example of annealing treatment effects on the relative strength of equiaxed α and transformed β in Ti-6Al-4V is shown in Figure 18. It is worth noting that a dual phase α - α' microstructure may result from the final water quench applied by the



(a)



(b)

Fig. 24—(a) SEM micrograph and crystallographic orientation map along the loading direction showing the occurrence of prismatic slip stimulated twinning (reprinted with permission from Ref. [116]). (b) Twinning occurrence as a function of the m' values, the twin Schmid factors and the Schmid factor of the incoming slip bands (reprinted with permission from Ref. [112]).

authors^[125] and be the origin of the differences with trends from Figure 17. This illustrates the difficulties in drawing any general conclusions on strain partitioning, particularly in view of the other effects on plasticity discussed below.

In addition SRO and α_2 precipitation state, which is influenced by both elemental partitioning and different heat treatment steps, also influence the strength.^[68,126,127] As shown in Figure 8 and discussed previously, basal and prismatic slip strengths are increased but the basal/prismatic CRSS ratio increases with SRO and α_2 precipitation.^[68] According to *in situ* TEM tension experiments performed on the equiaxed α phase of Ti-6Al-4V (which contains about 6 wt pct Al), SRO was found to inhibit cross-slip, favor pile-ups and pairs of dislocations, reduce the velocity of screw segments of paired dislocations and provide an additional strengthening.^[108] The diffuse antiphase boundary

energy due to the fault created when a single dislocation glides in the short-range ordered lattice was estimated to be about 11.6 mJ m^{-2} , which corresponds to a stress increment of about 40 MPa. The resistance caused by this fault inhibits the motion of single dislocations and paired dislocations, moving in a correlated way, are needed to overcome it. In SRO containing equiaxed α grains, cross-slip was only observed in large dislocation pile-ups with similar prismatic and pyramidal Schmid factors where glide of dislocations is impeded their initial plane because of a high density of dislocations in this plane. In contrast, frequent cross slip from basal or prismatic plane to pyramidal planes was reported to result in wavy slip traces in colonies where the magnitude of SRO is weaker.^[108] Figure 19(a) illustrates that aging promotes a greater degree of strain localization for prismatic slip, and that the strain localization can be different in equiaxed α and transformed β

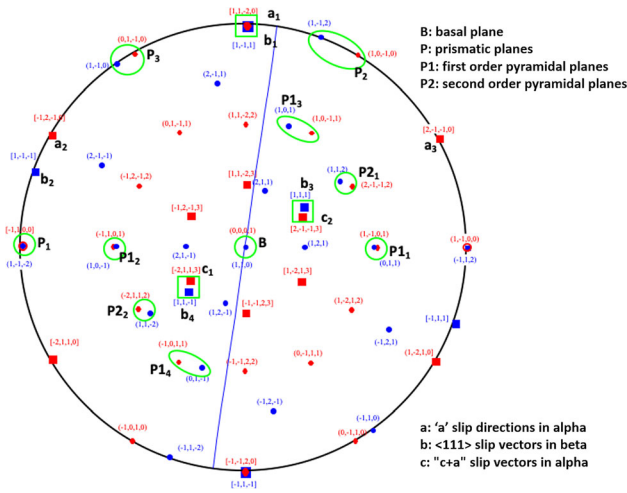


Fig. 25—A stereographic projection showing the alignment of slip planes and directions (encircled) in the α and β phases related by the BOR. The trace of the habit plane of α laths is also indicated (reprinted with permission from Ref. [1]).

(Figure 19(b)). This is shown in the distribution frequency of the normalized shear strain. While deformation mechanisms are affected by SRO and α_2 precipitates, Radecka *et al.* have not found a substantial effect on the deformation behavior at the level of grain averages.^[67] Finally it is worth noting that Al concentrations in excess of about 8.5 wt pct cause embrittlement of the α phase.^[128]

C. Microtexture, and Texture Effects

Slip activity can be significantly influenced by the non-random spatial distribution of crystal orientations due to thermomechanical processing of Ti alloys. Thermomechanical processing can induce millimeter sized regions with sharp textures.^[129] These microtextured regions (MTRs) have important consequences on the performance under a large variety of loading conditions such as fatigue,^[130] dwell-fatigue^[131] and monotonic tension.^[99] It is then important to distinguish microtexture, which refers to the local crystallographic orientation environment, from the global texture. The decorrelation of the respective effects of texture at these different scales is a significant experimental challenge as tuning of processing steps to change the degree of microtexture usually has an effect on the global texture as well. Despite this difficulty, numerous efforts have been put into the understanding of the influence of these microstructural features on the material behavior. For instance, Lunt *et al.* have linked plastic strain localization with the presence of MTRs as shown in Figure 20, which shows strain distribution in relation to MTRs.^[132] Several causes have been identified. Firstly, the low misorientation between neighboring α grains favors an easy slip transfer and long range slip localization.^[115] As a consequence, slip bands extend across multiple grains that are similarly oriented in the microplasticity regime due to the presence of MTRs (Figure 16(b)). It was shown recently in Ti-6Al-4V that slip transfer proceeds

at stress levels well below the yield stress and that it occurs almost systematically if slip systems on both sides of the boundaries are well aligned and experience a sufficiently high-stress magnitude.^[133] As discussed in the following sections, any potential very thin residual β layer at boundaries is not expected to inhibit slip transfer. The effective slip length is then increased as it is not set by the α grain size but the MTR size. Secondly, there is an interplay between the non-random spatial distribution of crystallographic orientations and the elastic and plastic anisotropies of α titanium. In particular, an increasing degree of microtexture leads to an exacerbated stress heterogeneity^[60,99] and an early onset of slip activity.^[99] Stress and plastic strain hotspots were found to be located within MTRs with a dominant [0001] orientation. Stress hotspots correspond to α grains well oriented for basal slip, which can be within the MTRs in isolated instances. An important feature is thus the presence of α grains misoriented with respect to the MTR dominant orientation. This is illustrated in Figure 16(b) where grains well oriented for basal or prismatic slip are present in a MTR with a dominant [0001] orientation (MTR 2). At low applied stress, the onset of slip activity is found to be favored in these grains, while similarly oriented grains can be found outside of such MTRs and display a delayed plastic activity.^[58] Long range mechanical effects, that are suspected to trigger crack nucleation at interfaces between MTRs under certain conditions, have also been found. These exacerbated stress and strain heterogeneities, which allow an early onset and development of plasticity, also lead to a lower yield stress of the material with an increasing degree of microtexture.^[99]

The global texture, which is different from the degree of microtexture, strongly influences the deformation behavior as well.^[134–137] This is particularly relevant for equiaxed and bi-modal microstructures as heavy deformation is usually implemented during the processing to realize such microstructures. Schematic representation of basal / transverse textures commonly obtained is shown in (0001) pole figures in Figure 21. For further details about processing conditions associated with these textures the reader is referred to Reference 2. Using different machining directions, the effect of textures was investigated experimentally while keeping other microstructural features constant. The Young's modulus, the yield and ultimate tensile strengths were found influenced by texture, while the ductility is relatively insensitive.^[2,135] The trends are illustrated in Figure 21. Crystal plasticity simulations have successfully reproduced experimental findings and related the different deformation behavior to the activity of the different slip modes for both equiaxed and bi-modal microstructures.^[134] It was showed that plastic anisotropy is a function of the angle between the c -axis of the grains composing the polycrystal and the loading direction. High strengths are obtained for loading direction parallel or nearly parallel to the c -axis as a low resolved shear stress applies on soft slip modes in most grains. In contrast, low strength are obtained if the c -axis is perpendicular to the loading direction in a

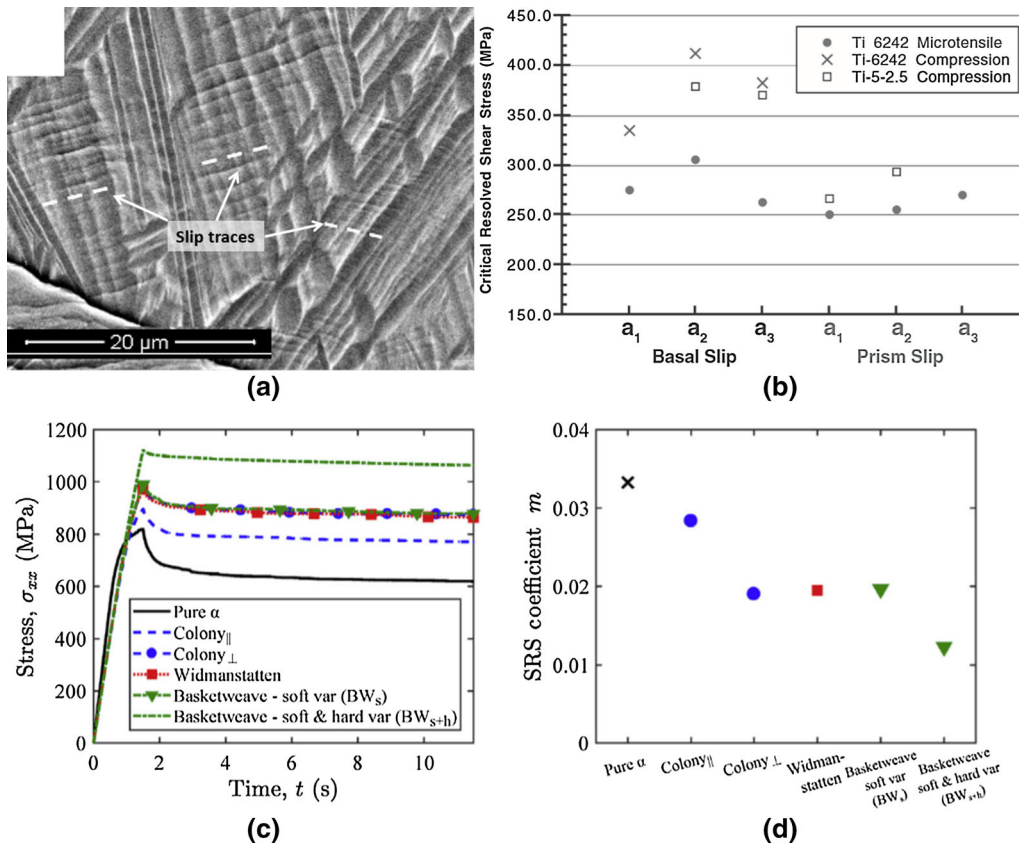


Fig. 26—(a) Basal slip lines restricted by colony size (reprinted from Ref. [14]), (b) CRSS calculated for tension and compression testing of single colony specimens showing plastic anisotropy (reprinted with permission from Ref. [155]), and (c) stress–strain curves and (d) apparent strain rate sensitivity depending on the type of microstructural elements considered (reprinted from Ref. [158] under the terms of the Creative Commons BY 4.0). The reader should consult the reference for an explanation of the microstructures associated with various designations.

majority of the grains, which enables deformation on soft slip modes.^[2,134,136]

D. Interactions of Slip Activity with Interfaces and Boundaries

Grain boundaries are the origin of a major strengthening effect for polycrystals, and is referred to as the Hall–Petch effect.^[138,139] This effect is frequently attributed to the ease of strain transfer across grain boundaries. In a recent study, specific thermo-mechanical treatments were applied to obtain controlled equiaxed and bimodal microstructures in Ti-6Al-4V in order to experimentally characterize the grain size dependence of the yield strength.^[140] In bimodal structures the Hall–Petch effect may relate to slip transfer between equiaxed α and the transformed β constituent of the structure. The resulting data are reported in Figure 22. The Hall–Petch coefficient is found to be about 230 MPa $\cdot\mu\text{m}^{1/2}$ for fully equiaxed microstructures or bimodal microstructures with a low transformed β fraction (≈ 25 pct). Similar orders of magnitude were found using crystal plasticity simulation with values ranging between roughly 200 and 350 MPa $\cdot\mu\text{m}^{1/2}$ for Ti-6Al-4V with a bimodal microstructure.^[141,142] An example is shown in Figure 22. Both experimental and simulation approaches have been used in order to evaluate the

effect the lamella thickness in colony structures on the microscopic and macroscopic responses.^[141,143] Both studies report a weaker size effect than for equiaxed α grains showing that α/β interfaces are soft barriers to dislocation glide. In particular, the Hall–Petch coefficient was found equal to 95 MPa $\cdot\mu\text{m}^{1/2}$ for Ti-6242. The evolution of the yield strength with the lamella thickness is presented in Figure 22. While α/β interfaces in lamellar colonies are considered soft barriers to dislocation glide, colony boundaries are more effective barriers to slip transfer. A combination of strengthening due to α/α grain boundaries and α/β interfaces exists in Ti alloys depending on the microstructure.

1. α - α grain boundaries

Once emitted by sources, dislocation glide is stopped by obstacles such as grain boundaries. Dislocation pile-ups can be formed against grain boundaries. This phenomenon is favored by the slip planarity observed in high Al titanium alloys where cross slip is inhibited by SRO and nanoscale α_2 precipitates. Prior studies reported the occurrence of cross slip in dislocation pile-ups due to the high stress experienced by dislocations. In particular, $\langle a \rangle$ -type first order pyramidal slip is observed to operate.^[108] These pile-ups are important for crack nucleation^[144] because of the resulting stress concentrations. Arrested slip bands were also found

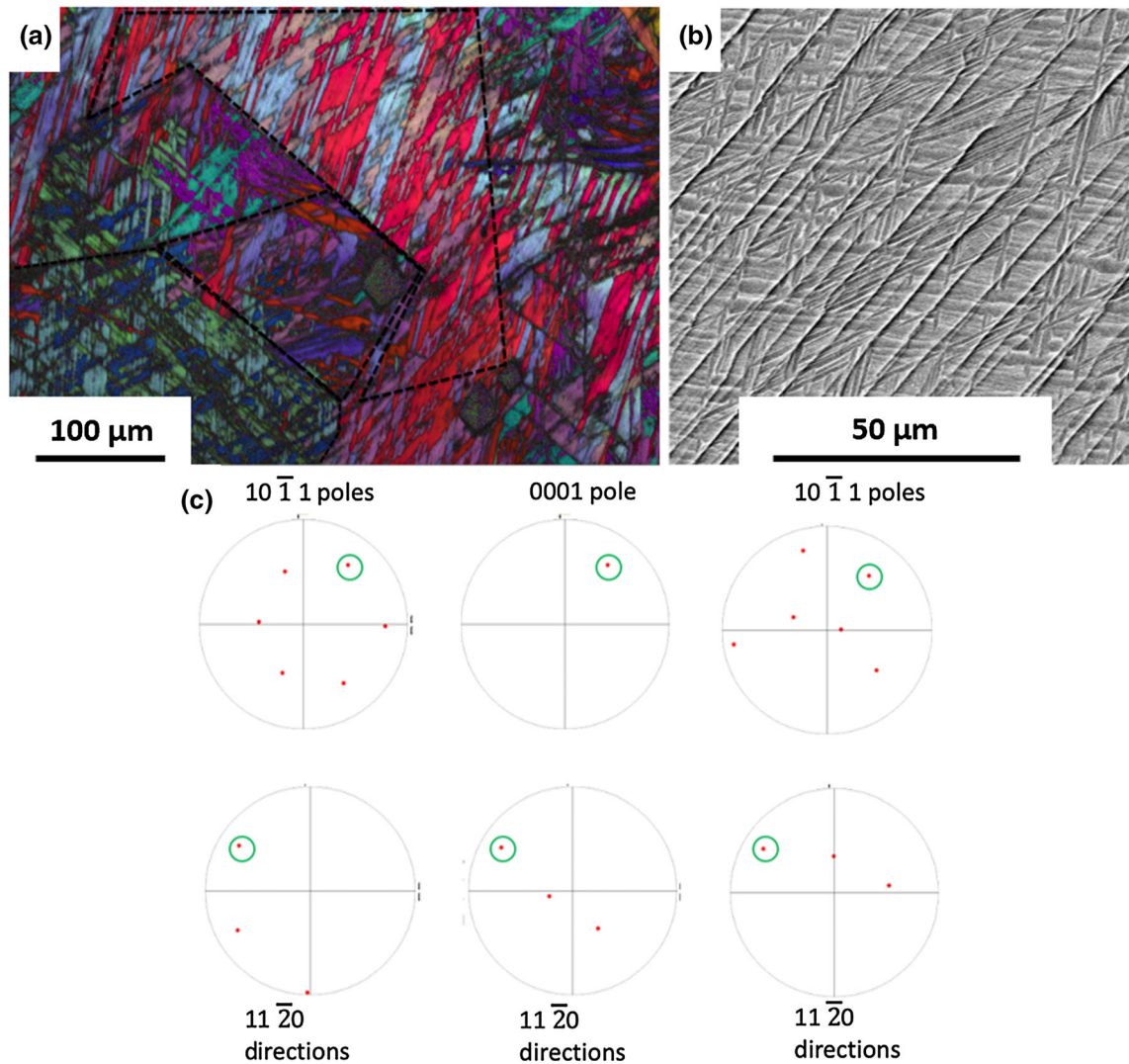


Fig. 27—(a) Groups of trivariant cluster that share a common $\langle 11\bar{2}0 \rangle_\alpha$ axis parallel to the a parent $\langle 111 \rangle_\beta$ outlined by the black lines, (b) slip bands running across a trivariant group, and (c) the pole figures show the parallel slip planes and slip direction of each variant in such a group (also refer to Fig. 2(e)) (reprinted from Ref. [14]).

associated to twinning in a neighboring grain which cannot deform by basal or prismatic slip.^[112,116]

Besides slip blocking at interfaces, the most frequent interaction is slip transfer across interfaces. For equiaxed or bi-modal microstructures, the consideration of slip transfer across α/α boundaries is essential to account for the deformation behavior. Ding *et al.*^[145] carried out a thorough characterization of dislocation—grain boundary interactions in Ti-6 pct wt. Al, showing complex interactions involving incoming, outgoing, reflected and grain boundary dislocations. As these processes are difficult to simulate and to account for using mesoscale crystal plasticity simulations, the occurrence of slip transfer was also examined during deformation of a specimen with a statistically relevant number of observations. It was shown that slip transfer occurs well below the yield stress of the material. The m' parameter, introduced by Luster and Morris,^[146] was used as a metric to assess slip systems alignment on both sides of the boundaries. It is calculated as the product of

cosines between slip plane normals and between slip directions. Hence, $m' = 1$ indicates a perfect alignment between deformation systems on both sides of the grain boundaries. A good correlation between m' values and slip transfer occurrences was found. Interestingly, the m' distribution is not sensitive to the stress/strain state. This is shown in Figure 23(a). Albeit not systematic, very frequent slip transfer was observed for m' values higher than ≈ 0.8 .^[133] Simulation of slip transmission was also successfully undertaken using 2D dislocation dynamics, and demonstrated a limited effect on the overall mechanical response while the microscale fields are deeply affected.^[147] This is illustrated in Figure 23(b). Slip band deviation along interfaces was recently evidenced in Ti-6Al-4V.^[112,148] An example is shown in Figure 23(c). This observation suggests that dislocations can be absorbed and induce sliding along interfaces. Several parameters were identified as influential: the slip mode, the anisotropy or the orientation of the slip band. A recent TEM study found similar

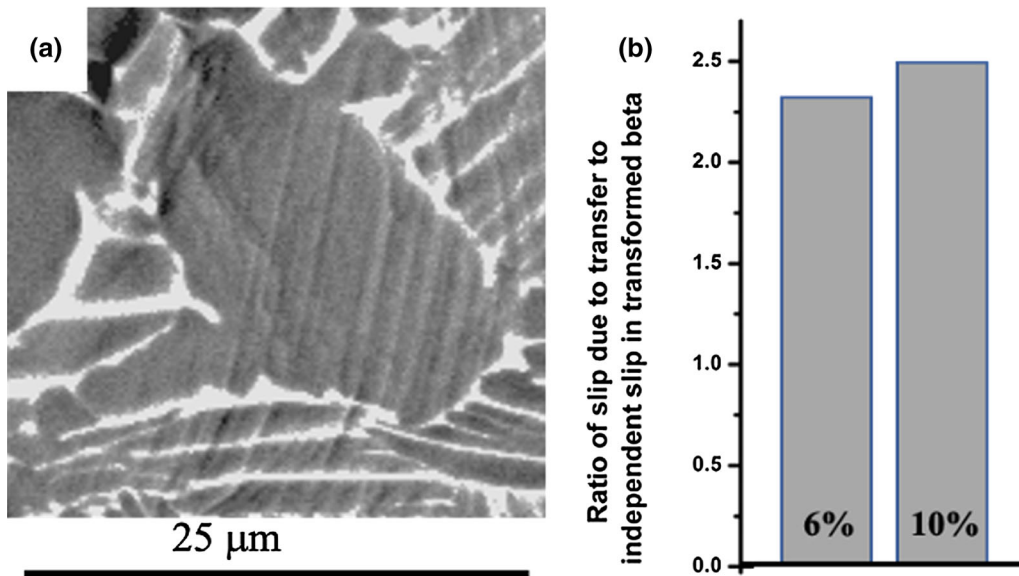


Fig. 28—(a) Slip transfer from equiaxed α into colony transformed β in Ti6242, (b) the ratio of slip in transformed β due to slip transfer to independent, global Schmid factor determined slip as a function of strain (reprinted with permission from Ref. [122]).

processes such as blocked slip, slip transfer and dislocation incorporation into α/α grain boundaries to occur under low cycle fatigue loading of Ti-6Al-2Sn-4Zr-2Mo-0.1Si.^[149] The activation of dislocation sources due to a dislocation pile-up in a neighboring grain was also observed to accommodate strain incompatibilities.

2. Competition with twinning

As discussed previously, the operation of twinning in the α phase is strongly dependent on the aluminum content of Ti alloys. However, it was reported to occur in Ti-6Al-4V and is thus expected to be potentially active in any Ti-6Al alloy. As only $\{10\bar{1}2\}10\bar{1}1$ was reported up to moderate strains, only this twinning mode is discussed in the following. Fitzner *et al.* tested binary Ti-Al alloys in compression at room temperature and showed first an increase in twinning activity, facilitated by the aluminum additions, while this activity was found to drop suddenly with the formation of SRO and α_2 .^[54] Its occurrence was also reported under tension and cyclic loading.^[116,117] Dynamic loading exacerbates the twinning activity.^[150] The reported data suggests that the early twinning activity proceeds after a few percent strain.^[54,112,116,117,151] While under compression loading twins are located in grains with their c -axis nearly normal to the loading axis, Lavogiez *et al.*^[116] found twins in grains with their c -axis within 20 deg from the loading axis. In grains with such orientations, activation of basal or prismatic slip is difficult and $\langle c + a \rangle$ pyramidal slip was found to operate. The intense pyramidal slip activity noticed suggests that they experience high stress prior to twin formation. This observation is consistent with the CRSS values for $\langle c + a \rangle$ pyramidal slip and twinning reported for compression tested Ti-6Al-4V up to a strain of 20 pct.^[150] Besides, these twins were systematically found to result from the

interaction between a slip band and a boundary.^[116] An example of prismatic slip stimulated twinning is presented in Figure 24(a). In agreement with other studies focusing on CP-Ti,^[152] the alignment between slip systems is an important factor. The Schmid factor of the active twinning variant, but also the one of the incoming slip system which qualitatively indicates the possibility of the neighboring grains to experience plastic strain, are important factors as well. This is illustrated in Figure 24(b) where observed twinning occurrences are displayed as a function of the m' parameter introduced by Luster and Morris and the Schmid factors.^[116] Most occurrences are found for m' values higher than ≈ 0.8 and twin Schmid factors higher than 0.46. It is interesting to notice that this m' threshold is similar to the one obtained for slip transfer, which confirms the relation between the occurrence of twinning and slip transfer suggested by Wang *et al.* on CP-Ti.^[152] Twinning seemingly enables the accommodation of deformation incompatibilities and high stresses generated near the boundary. However, such type of interaction between slip bands and grain boundaries were found to be quite rare.

3. Slip transfer at α - β interfaces

Figure 25 illustrates the parallelism of slip systems between the α and β phases when they are related by the BOR. A $\{110\}_\beta$ slip plane is aligned with the $(0001)_\alpha$ plane. An a direction of the α phase, denoted as a_1 , is closely aligned with a $\langle 111 \rangle_\beta$ direction. As a consequence, a_2 deviates from another $\langle 111 \rangle_\beta$ direction by about 10 deg. Finally, a_3 has no matching $\langle 111 \rangle_\beta$ direction. These orientation relationships also imply that a $\{112\}_\beta$ plane is closely aligned with that prismatic plane which is nearly parallel to the habit plane of the plates whose trace is indicated on the

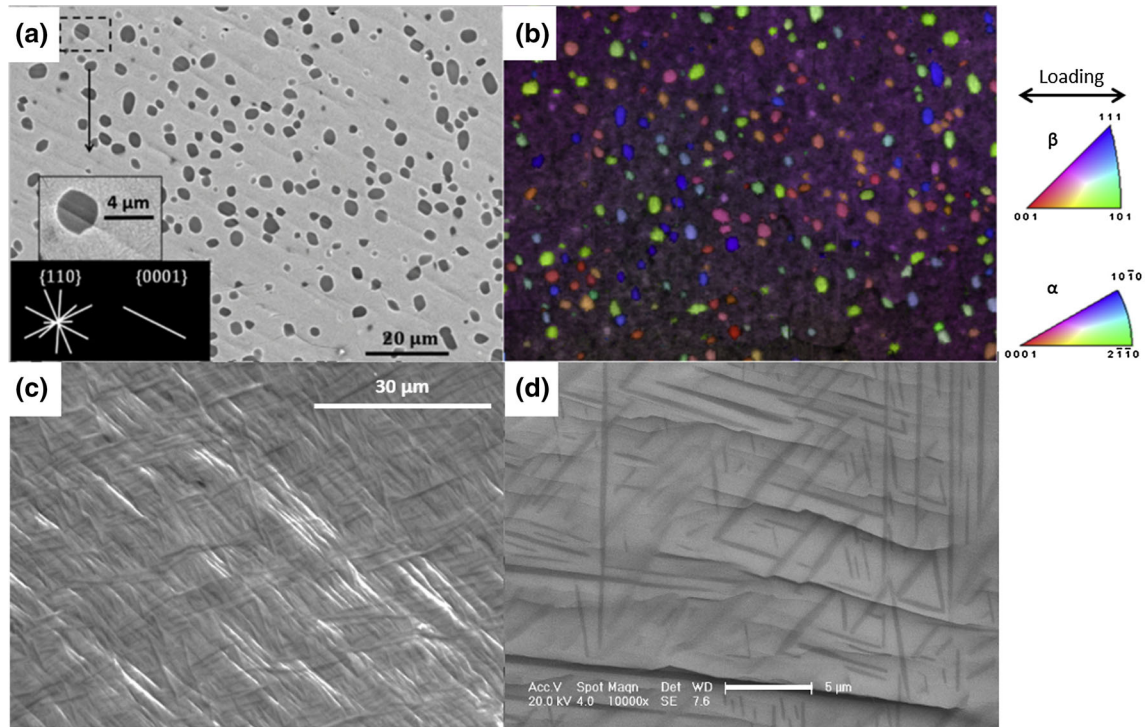


Fig. 29—(a) Slip traces showing extension of basal slip initiated in equiaxed α across transformed β matrix along a $\{110\}$ plane. Both α and β slip systems are well-aligned and exhibit high Schmid factors, (b) the associated crystallographic orientation map along the loading direction (reprinted with permission from Ref. [59]), (c) surface slip offsets after compression at room temperature in the metastable β Ti5553 alloy with a multivariant structure shows restricted slip lengths in the multivariant structure (d). Detail of (c) showing that slip lines shear some α plates but are blocked at others. Slip parallel to α/β interfaces is also observed. (reprinted from Ref. [14]).

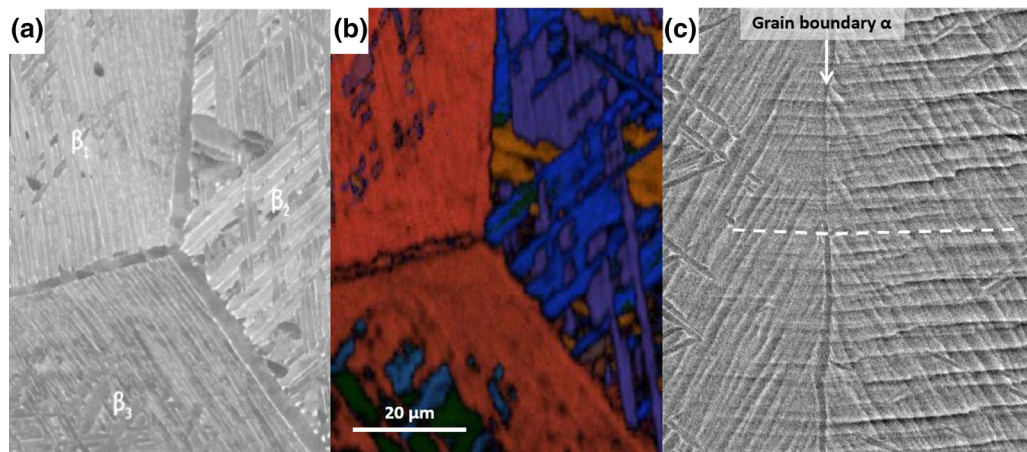


Fig. 30—(a) Grain boundary and Widmanstätten sideplates, (b) the EBSD image shows that the grain boundary α and sideplates in either grain have an identical crystallographic orientation, courtesy Adam Pilchak, (c) slip transfer across grain boundary α (reprinted from Ref. [14]).

figure. Other $\{110\}_\beta$ slip planes also lie nearly parallel to first order pyramidal planes and contain $\langle 111 \rangle_\beta$ directions that are closely aligned to an a_1 or a_2 direction or a $\langle c + a \rangle$ direction. Some $\{112\}_\beta$ planes lie nearly parallel to second order pyramidal planes and these contain a $\langle 111 \rangle_\beta$ slip direction that is nearly parallel to a $\langle c + a \rangle$ slip direction. The magnitude of

the undissociated $\langle c + a \rangle$ vector is nearly double that of $\langle 111 \rangle_\beta$.

The parallelism of slip planes and directions allows easy slip transfer between BOR related α and β phases. However, the orientation relationships can deviate from the exact BOR and yet allow slip transmission across such interfaces.^[153] We first describe some geometric

features that define mean free paths for slip for different α variant distributions.

Colony structures as shown in Figure 2(a) consist of crystallographically identical α variants that are aligned parallel to one other with thin ribs of retained β between them. *In situ* TEM tension testing revealed that the β layers do not inhibit the dislocation movement in such colonies.^[107] Thus, a single colony effectively behaves like a single crystal of the α phase defining the colony size as the slip length (Figure 26(a)). However, slip transmission mechanisms vary depending on the slip direction considered (\mathbf{a}_1 , \mathbf{a}_2 and \mathbf{a}_3) and thus introduces an anisotropy in the mechanical behavior at the colony scale. This is illustrated in Figure 26(b). The different mechanisms controlling slip transmission across α/β interfaces and the associated effect on the mesoscale behavior have been thoroughly investigated, in particular using TEM and single colony specimens tested in both tension and compression.^[154–156] Phase field simulations were recently shown to be a powerful tool to understand slip transmission across α/β interfaces.^[157] Due to the complexity of such mechanisms, the reader is referred to these references for further details. It may also be highlighted that other parameters influence the ease of slip transfer and the colony scale mechanical response: the magnitude of the residual Burgers vector, elastic anisotropy between both phases, the mean free path for dislocation glide in each phase and the interaction of mobile dislocations with the geometrically necessary dislocations at the interface.^[1] The mesoscale mechanical behavior is deeply affected by the morphological and crystallographic features of α/β arrangements.^[158] This is illustrated in Figure 26(c). It is worth noting

that the authors also found a strong effect on the apparent strain rate sensitivity (Figure 26(d)).

It has quite recently been found that that other variant distributions are transparent to slip apart from the colony structure.^[14] Thus the basket weave structure of Figure 2(b) in large area EBSD patterns (Figure 27(a)) show distinct groups (outlined by the dark lines) of tri-variant clusters that share a common $\langle 11\bar{2}0 \rangle_\alpha$ axis parallel to a parent $\langle 111 \rangle_\beta$ as shown in Figure 2(e). Slip bands are observed to extend across such groups (Figure 27(b)) and this is possible because such slip bands lie parallel to $\{110\}$ and $\{0001\}$ slip planes of each variant in such a trivariant cluster, are parallel to a $\{110\}_\beta$ parent, and share the common slip direction. This is illustrated in Figure 27(c). The effective slip length is, therefore, equivalent to the ‘colony’ size where the ‘colony’ now represents the size of these specific multivariant groups with a common $[11\bar{2}0]$ direction rather than the size of a group of similarly oriented variants shown in Figure 27.

It has generally been assumed that well recrystallized equiaxed α structures are not in a BOR with adjacent β grains. However, the epitaxial recrystallisation process during thermomechanical processing described earlier (Figure 4(a)) results in equiaxed α that can be in a near BOR with some of the surrounding β grains. As a consequence it has been observed^[59,122] that a significant fraction of the slip in the transformed β constituent of the structure can result from slip transfer from the equiaxed α which yields first, such the observed slip systems were better explained by a slip transfer factor such as the Luster-Morris parameter (m') associated with the slip system in equiaxed α and the adjacent colony structure. An example of this behaviour is given

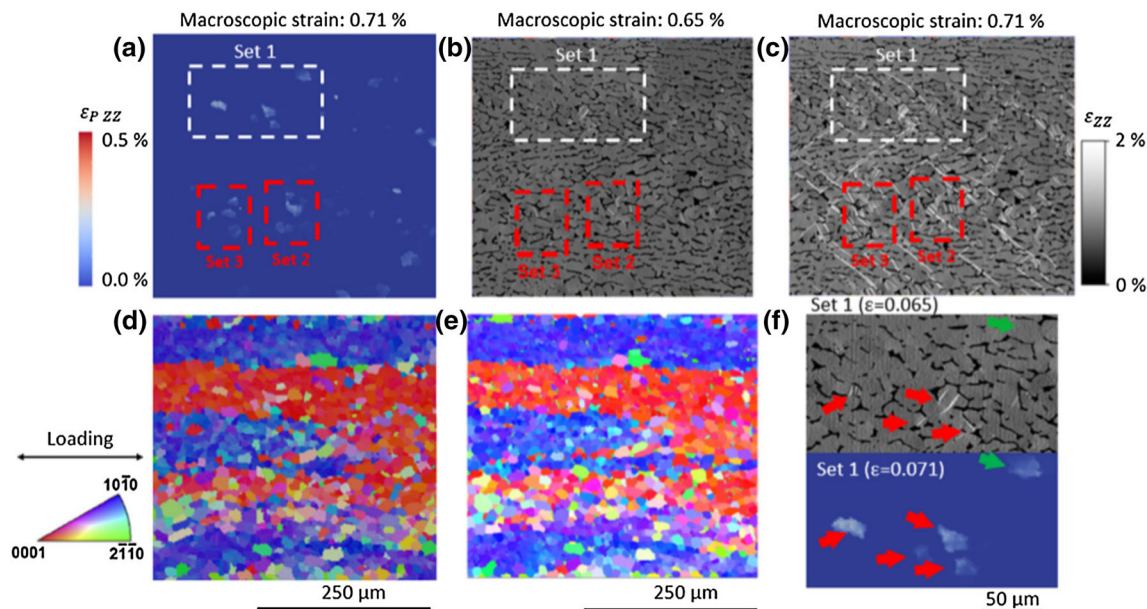


Fig. 31—(a) Simulated plastic strain field using an experimentally collected 3D polycrystalline aggregate and (b) and (c) experimentally obtained plastic strain field showing a good agreement regarding plastic strain localization at the MTR scale (Sets 1–3, where an early slip activity is observed correspond to similar regions). The crystallographic orientation along the loading direction is shown for (d) the polycrystalline aggregate and (e) the experimentally characterized microstructure. The red arrows in (f) also demonstrate a good agreement between experimental (up) and simulated fields (down) at the grain scale (reprinted with permission from Ref. [99]) (Color figure online).

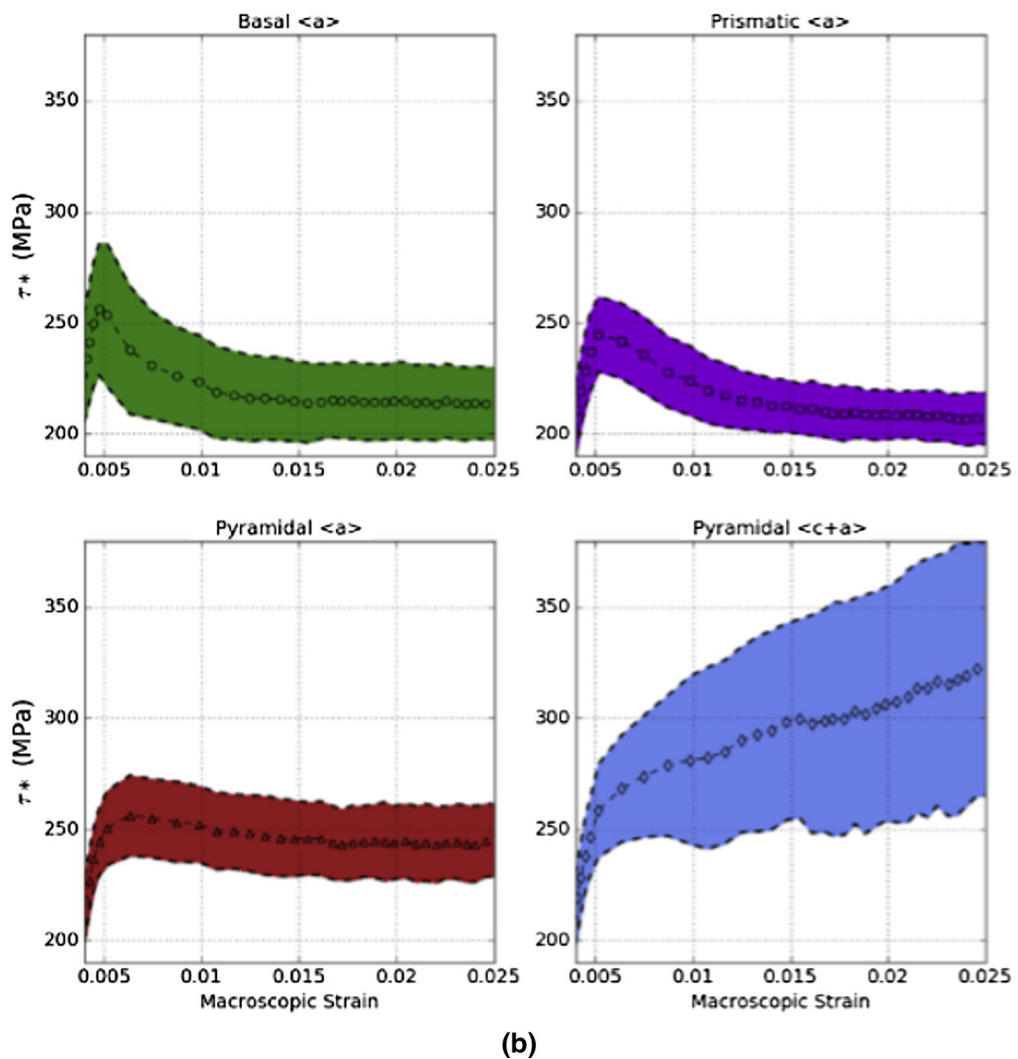
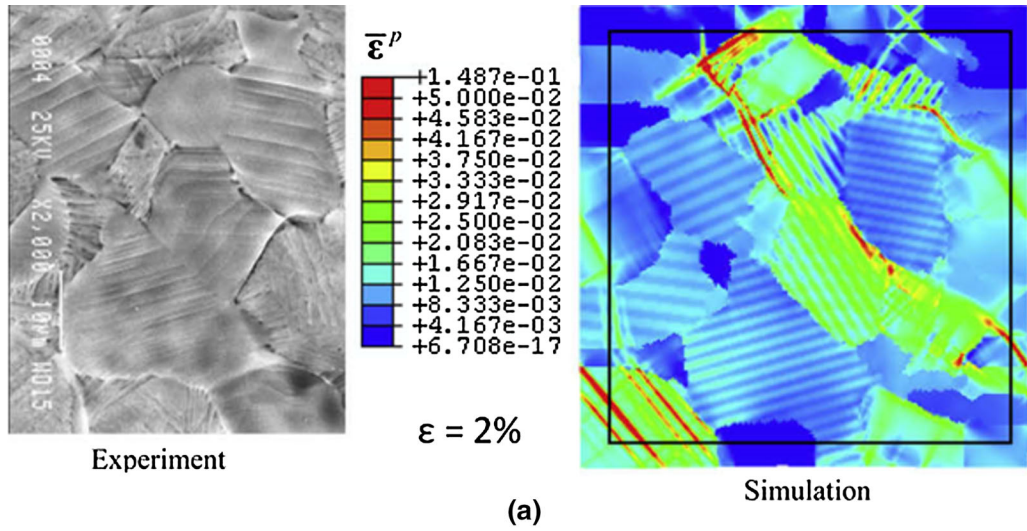


Fig. 32—(a) SEM micrograph of a deformed Ti-6Al-4V specimen with a bi-modal microstructure along with a simulated plastic strain field at a strain of 2 pct using a CP model including SRO induced softening (reprinted with permission from Ref. [170]), (b) slip strength evolution for different slip modes as fitted using high energy X-ray diffraction microscopy data and crystal plasticity simulations (reprinted with permission from Ref. [171]).

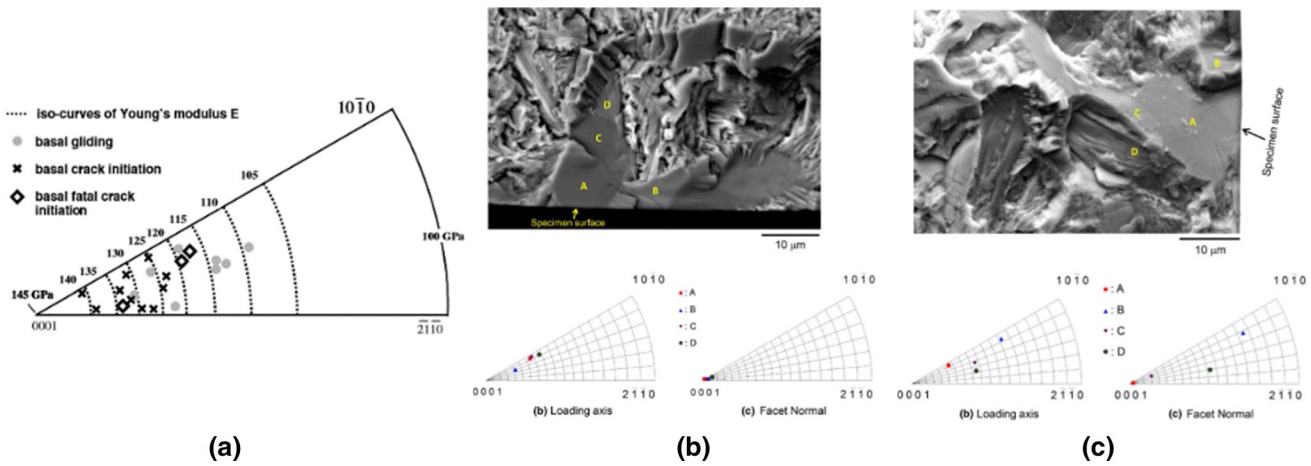


Fig. 33—(a) Crystallographic orientations at fatigue crack initiation sites relative to the loading direction with the orientation of α grains with basal slip activity indicated (reprinted with permission from Ref. [179]), (b) fatigue crack initiation sites showing a faceted morphology and low lifetimes for crack growth along well aligned basal planes, (c) crack growth along non basal planes with longer lifetimes (reprinted from Ref. [188]).

in Figure 28. In the metastable β Ti-5553 alloy as well, slip was observed to initiate in primary α and extends in the transformed β regions.^[59] Owing to a good alignment between basal slip systems and $\{110\}\langle 111\rangle$ slip systems, slip transfer occurs on slip systems with high m' values. The slip traces in transformed β regions match the $\{110\}$ plane traces at the mesoscale as shown in Figures 29(a) and (b).

A somewhat different situation pertains when the multivariant α is embedded in a coarse β matrix (where the slip length in β is high) as in Figure 2d. Slip lengths in this situation are found to be restricted as shown in Figures 29(c) and (d). Slip initiates in the β phase (when no equiaxed α is present) and has been identified through Burgers vector and slip traces analysis to belong to the $\{112\}\langle 111\rangle$ system. Crystallographic analysis shows that for a particular set of this family, slip planes and directions in the twelve variants of the α phase will lie close to the β slip system in only a few cases with high Luster–Morris parameters, m' .^[14] The slip length will then be defined by the non-random, 3D distribution of the α variants (Figure 3 and Reference 2) and the probability of slip bands in β intersecting variants across which slip transfer cannot occur.

The epitaxial process described above also results in special misorientations between the recrystallised β grains, as explained in Reference 19 and given in Figure 4(c). Figure 30 shows examples of such grains in a β heat treated structure. Grain boundary α forms preferentially at those boundaries that are related by these misorientations^[11,13] because their crystallography allows the α phase formed at such β boundaries to be Burgers oriented to both grains. Widmanstatten sideplates originate from grain boundary α and extend into both β grains to which it is Burgers related (Figures 30(a) and (b)). When the adjacent β grains are related by the special misorientation $\langle 111\rangle$ 60 deg, the rotation axis is a common slip direction in both β grains and the close packed direction in α , and the symmetry about this rotation axis in relation to the

Burgers orientation relationship with α ensures that slip planes in the two adjacent grains and the grain boundary α with this Burgers vector will be parallel or very nearly so.^[14] Figure 30(c) shows that in this specific case, slip can transfer from one β grain to another across the grain boundary α and its sideplates.

In summary, the energetics associated with the BOR governs the morphology and distribution and misorientations between the α and β phases from different thermomechanical processing paths and chemistries, and in turn the probability of slip transfer between the two phases and mean free paths for slip. While many of the results described above have been obtained in post macroscopic yield conditions, it is quite likely these characteristics will manifest themselves in the microplasticity regime as well. Methodologies of incorporation of interface reactions and kinetics into crystal plasticity models are now emerging.^[98,122,159] Most often however, multivariant α distributions in transformed β are homogenised in such models into representative kinetic parameters.

In addition, in view of the complexity of interaction of compositional and microstructural effects at various length scales that have been described above, the use of genetic algorithms and neural networks on a property database to isolate these effects,^[143,159,160] may provide useful insights into the physics of various processes, provided an adequate input of various parameters is used.

VI. MICROMECHANICS AND COMPUTATIONAL CRYSTAL PLASTICITY

Mechanistic understanding of the interplay between mechanical response and microstructure has been intensively investigated using crystal plasticity (CP) simulations. In particular, it is a key technique for the understanding of the texture related anisotropy, assessment of fatigue lives or dwell-related fatigue life debits.

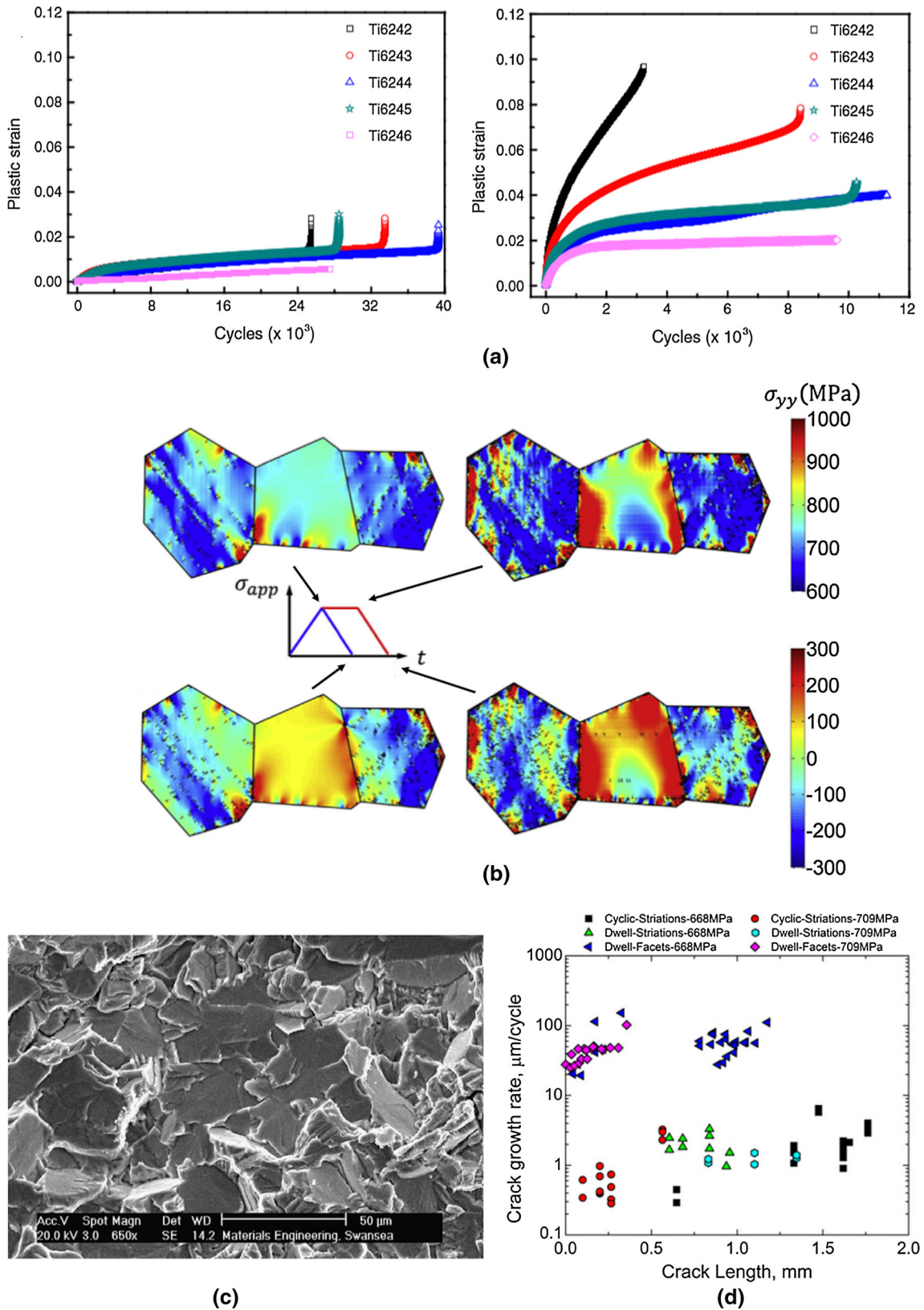


Fig. 34—(a) Cumulated plastic strain as a function of the number of cycles at room temperature for various alloys (fatigue on the left-hand side and dwell-fatigue on the right-hand side) (reprinted from [203]), (b) stress fields showing the load shedding onto hard grains (center grain) associated with the dwell-fatigue loading (different loading paths are shown with arrows) (reprinted from Ref. [172] under the terms of the Creative Commons BY 4.0), (c) typical faceted crack initiation sites [216] and (d) short crack growth rates depending on the growth mode (faceted or striations) and loading conditions (fatigue or dwell-fatigue) (reprinted with permission from Ref. [212]).

values in colonies while considering both α and β orientations.^[110] With this approach, the CRSS is higher in colonies by 4 to 14 pct depending on the slip system. Size effects were also analytically incorporated considering characteristic lengths for more predictive insights in Reference 141. With the development of new simulation techniques and computing capacities, explicit modeling of the dual phase structure becomes affordable.^[174] Such approaches highlight the key role of strain gradient hardening effect and slip transfer.^[167,175]

CP simulations have also provided evidence for and assessment of load shedding occurring during creep loading, an important feature of dwell fatigue. This behavior is found to result from the interplay between abnormally low hardening rates in Ti alloys that stems from SRO or precipitate shearing and minimal interactions between slip systems, as well as moderate strain rate sensitivities.^[176] This softening was incorporated in the model of Pagan *et al.* and calibrated using near field- and far field- HEDM data.^[171] The evolution of the slip system strength with respect to the macroscopic applied strain is shown in figure 32(b). The combination of synchrotron characterization and crystal plasticity models provides a useful combination of data including crystallographic orientations and stress and strain states at the grain scale for calibration and validation of the simulated behavior.^[102,169] It was also recently highlighted that initial residual stress plays a key role and can be extracted from HEDM experiments and used as an input for CP simulations.^[177]

As mentioned in the dedicated section, microtextured regions have a substantial influence on the mechanical response and the material performance. However, consideration of such regions is a significant challenge. Although a crystallographic orientation is dominant, locally misoriented grains play a critical role in the deformation behavior and long range mechanical effects may exist.^[99] It is therefore important to consider mm-scale realistic 3D microstructures to obtain a faithful reproduction of the experimental behavior, which is a challenge that can be overcome using recently developed 3D reconstruction techniques. The second challenge is the simulation of such large polycrystalline aggregates. This can now be achieved using fast-Fourier transforms based crystal plasticity simulations.^[178] Finally, recent investigations have also shown that the onset of slip activity proceeds at slightly lower strain in interior grains compared to traction free surface grains.^[168]

VII. FATIGUE AND DWELL-FATIGUE CRACK NUCLEATION MECHANISMS IN RELATION WITH MICROPLASTICITY

A. Fatigue

Plasticity processes govern the fatigue behavior of Ti alloys. As a consequence, numerous features previously discussed have been found to affect the material response at different scales under cyclic loading. While an exhaustive overview of the cyclic deformation behavior of Ti alloys is out of the scope of the present article, a few

examples are given in the following to illustrate this relationship. Cyclic softening was noticed during strain controlled loading by numerous researchers^[179–181] and was found to result from Ti_3Al precipitate shearing.^[182] Plasticity also governs the fatigue life as localized basal slip is known to be involved in quasi-cleavage facet formation under fatigue loading.^[183,184] This feature is consistent with the observation of basal slip activity at lower applied stress than the other slip modes as discussed in the previous sections. This specific role of basal slip has been observed for many Ti alloys from the near- α Ti-6242 alloy to Ti-6246, which is sometimes considered as a metastable β alloy, and over a wide range of loading conditions including low, high and very high cycles fatigue.^[179,185–188] However, crack nucleation on prismatic slip bands was occasionally reported with specific microstructures.^[65,189] Fatigue crack nucleation and microcrack propagation resistance is improved^[190] with decreasing slip length. It was recently demonstrated from experimental observations that fatigue crack propagation can proceed along pre-existing slip bands.^[191]

Microplasticity is thus quite critical in developing a reliable understanding and prediction of performance under cyclic loading and microstructural features play a major role in providing a critical configuration leading to crack initiation.^[192] The effective slip length which governs the fatigue performance, is classically equivalent to the equiaxed α grain size in equiaxed structures. In fully lamellar colony microstructures slip length is usually taken as equal to the colony size. As β layers are soft barriers to dislocation glide, lamellar microstructures exhibit a high slip length and poor fatigue crack nucleation resistance in comparison to equiaxed or bi-modal microstructures. The effect of microtextured regions on long range strain localization and slip transfer is also important. The effective slip length is increased with the presence of MTRs as described earlier. These considerations outline the critical importance of considering slip band-grain/phase boundary interaction and potentially associated processes such as grain boundary sliding or twinning. As discussed previously, complex interactions between slip bands and grain boundaries or interfaces lead to complex relationships with the fatigue behavior. Other studies also suggest an important role of the stress normal to the basal plane in crack formation, which was found to occur preferentially on this slip plane.^[179] Thus the c-direction of α grains in which crack nucleation occurred is less than 45 deg from the loading axis, while basal slip proceeds for declination angles higher than 45 deg as well. This is illustrated in Figure 33(a) where the crystallographic orientation of α grains at crack initiation sites is reported along with the orientation of α grains where basal slip traces were observed. Recent simulation and experimental studies demonstrated that MTRs with a dominant [0001] orientation lead to higher stress and strain magnitudes,^[58,99] which may also be consistent with a reduction in fatigue life and the preferential crack nucleation in such regions.^[179,187,193] A recent study suggested that the orientation of the slip direction is an important parameter as well, and should exhibit a relatively high component normal to the specimen surface.^[194] This feature may

facilitate reaching a critical slip step height such as noticed for crack nucleation on Ni based superalloys.^[195] Data analytics combined with crystal plasticity simulations have been employed to identify influential parameters and confirmed the role of parameters enumerated previously.^[196]

In spite of these substantial characterization efforts, prediction of fatigue crack initiation sites is still a significant challenge. This is linked to the underlying randomness and hierarchy in the microstructural scale.^[192] Therefore, microstructure sensitive models have been employed for an accurate simulation of the fatigue behavior. CP simulation approaches are usually employed to obtain stress and strain fields at the microstructure scale. Consideration of residual stress at the grain scale in such simulations is allowed by recent experimental and simulation approaches. This enables an improved agreement between predicted and measured mechanical fields^[169, 177] as well as promising insights into an improved prediction of the fatigue behavior, which is affected by residual stress. The Fatemi–Socie parameter is often successfully used as a Fatigue Indicator Parameter (FIP).^[197–199] Used at the macroscopic scale, it successfully accounts for fatigue lives of Ti-6Al-4V submitted to multiaxial loading.^[200] However, it was also used at the mesoscale by Goh *et al.* for instance.^[199] This critical plane approach is consistent with the experimentally observed combined effect of strain localization and high stress normal to the basal plane. As fatigue life variability is a major concern for Ti alloys,^[188, 192] a dedicated approach has been proposed to identify microstructure sensitive extreme value probabilities.^[198] A good agreement between features found at crack initiation sites and high FIP values was observed. Short crack growth was also reported to play a major role in the fatigue life scatter, as crack growth might be facilitated by well aligned slip planes.^[188] This is illustrated in Figures 33(b) and (c), where short-life and long-life crack initiation sites are presented along with the crack plane and the crystallographic orientations at the initiation site. Short fatigue lives are found for crack growth along well aligned basal planes. This finding agrees well with the observations of Zhang *et al.* who reported a minimal resistance to crack growth along well aligned slip planes.^[201] This naturally implies a detrimental effect of microtextured regions on the fatigue performance.

Finally, it is interesting to notice that alternative mechanisms have been suggested for fatigue crack initiation and employed to account for crack initiation features and for fatigue life assessment.^[201, 202] In these studies, the interface between macrozones or grain boundaries were considered to be critical for crack nucleation due to slip impingement at these interfaces. Such mechanisms are very similar to the one reported for dwell-fatigue loading conditions.

B. Dwell-Fatigue

A long standing issue in titanium alloys is the dwell-fatigue life debit introduced when the peak stress is held for a significant time (> 30 seconds) at or near

room temperature. As debits up to $\times 10$ to $\times 20$ have been reported,^[203–206] this topic has attracted considerable effort for several decades. This section captures key features and is not intended to provide a detailed overview. Indeed, this is an intricate phenomenon as the magnitude of the dwell debit is influenced by microstructural features such as composition, morphology, SRO, microtexture, *etc.* and testing conditions such as the peak stress, the loading waveform, the load hold duration, temperature, *etc.* However, microplasticity plays a major role in this phenomenon which is closely linked to the occurrence of creep at room temperature in Ti alloys. Indeed, Qiu *et al.* highlighted the relation between dwell debit and plastic strain accumulation during the hold in load.^[203] This is illustrated in Figure 34(a). As a consequence, the active deformation mechanisms, which depends strongly on the accumulated plastic strain, may differ. As several percent plastic strain can be achieved, the operation of $\langle c + a \rangle$ pyramidal slip and twinning is more frequent.^[112] In particular, the sensitivity to the alloy composition is noticeable on this plot: Ti-6242 is dwell sensitive while Ti-6246 is not. More generally near- α alloys usually exhibit a higher dwell-sensitivity than $\alpha + \beta$ alloys. This feature does not seem to stem from different active deformation mechanisms.^[57] The crack initiation mechanism postulated by Evans and Bache based on experimental characterization of dwell-fatigue tested specimens^[144] suggests that $\langle a \rangle$ type slip activity in a soft grain triggers basal or near basal facet nucleation in an adjacent hard grain due to a stress concentration in this grain resulting from dislocations piled-up at the interface between the soft and hard grains. A typical faceted crack initiation site such as found under dwell-fatigue loading is presented in Figure 34(c). Further support to this mechanism came from additional analysis.^[101, 207] Crystal plasticity simulations enabled quantification of the load shedding between hard and soft grains, thus highlighting the effect of the load hold on the local stress in hard grains. This is presented in Figure 34(b), where the stress field obtained from dislocation dynamics simulations reveals a higher stress magnitude reached in the hard grain after the load hold. Various effects from the microstructure including the type of microstructural elements,^[158] the crystallographic orientation^[208] and the slip modes^[118] or test conditions such as temperature^[166] and loading type were investigated.^[208] In particular, the disappearance of the dwell effect at temperatures around 200 °C^[2] in Ti-6242 was found to be controlled by the time constant associated with the process of thermally activated dislocation escape. Experimental investigations highlighted that SRO and α_2 precipitation states are also important factors, as low cooling rates, which promote SRO and α_2 formation are associated with increased dwell-fatigue life debits.^[209] In addition, basal slip in the soft grain plays a major role as several studies reported the presence of α grains suitably oriented for basal slip at crack initiation sites.^[185] Two causes can be found in the literature: first, basal slip being more rate sensitive than prismatic slip, it induces higher stresses in neighboring hard grains^[118] and α grains where basal slip operates

generally experience higher plastic strain magnitudes,^[113] which may also favor incompatibility stresses. However, a recent study reported a complex interplay of $\langle c + a \rangle$, $\langle a \rangle$ slip and twinning in these grains.^[112] As a consequence, the exact process of crack nucleation in hard/soft grains is not clear yet as highlighted in Reference 210 where multiple deformation mechanisms (*i.e.*, basal and $\langle c + a \rangle$ pyramidal slip) are found active underneath the fracture surface at crack initiation sites. As no twin was previously reported to be present at crack initiation sites, it was assumed to be beneficial and to delay cracking.^[112] A beneficial effect of twinning was also found on the crack propagation resistance.^[211] It is worth mentioning that several studies suggested that short crack growth seemingly has a dominant contribution to the dwell effect.^[212–214] This is mainly attributed to faster faceted short crack growth rates with applied load holds at peak stress. Such an effect is illustrated in Figure 34(d). The MTRs, providing long-range path for rapid faceted crack propagation, are strong controller of dwell fatigue lifetimes.^[214] Several researchers pointed out that the facet normal is deviated from the c -axis by 10 to 15 deg and thus that the crack path does not coincide with the basal plane.^[215] The exact mechanisms associated with this crack growth process is still not clear. Its identification, including the plasticity processes at crack tips and possible hydrogen effects is key to tackling dwell debit issues.

VIII. SUMMARY

Titanium and its alloys constitute a unique set of relatively coarse microstructural combinations of two ductile phases of similar slip strengths. The two phases, hcp(α) and bcc(β) can be distributed in a variety of morphologies and length scales and are in most cases related by Burgers orientation relationship which allows a parallelism of some slip planes and directions in each phase enabling easy slip transfer. The major microstructural categories include single phase polycrystalline α , two-phase structures which have a fully lamellar distribution of α within β grains or equiaxed α grains with β films at their boundaries or bimodal structures of equiaxed α and lamellar α , and finally, polycrystalline β phase containing a variety of metastable nanoscale products.

α phase is both elastically and plastically anisotropic. Grain orientations with the c -axis aligned along the loading direction are elastically stiff and plastically hard. In α phase containing 6 to 7 wt pct Al, which is the composition of the α phase in most two phase engineering alloys, plasticity initiates through basal and then prismatic $\langle a \rangle$ slip with subsequent accommodation by pyramidal $\langle a \rangle$ slip in soft grains and pyramidal $\langle c + a \rangle$ slip and sometimes twinning in hard grains. Slip is planar due to short range order or Ti_3Al (α_2) precipitation in these compositions. Substantive crystal plasticity-based modelling of early plasticity has been carried out with reasonably well-defined slip parameters and good predictive capability.

The plasticity of the β phase depends significantly on compositional effects on its stability with respect to stress induced transformations and its intrinsic complex, nanoscale structural ensembles of the ω and O' . Elasticity of β is strongly influenced by the presence of these phases. Stress induced transformation to α'' martensite has been exploited in shape memory behaviour. Transformation induced plasticity and twinning induced plasticity can be induced by tailoring composition, and various stress induced products α'' , ω , or $\{332\}\langle 11\bar{3} \rangle$ and $\{111\}\langle \bar{1}\bar{1}2 \rangle$ twinning can occur under stress to form a hierarchical pattern of structures. Uniquely, the O' phase can act as precursor to nanoscale distributions of α'' martensite that form continuously under stress or decreasing temperature to produce non-linear pseudoelasticity or even invar and elinvar effects. In more β enriched compositions, deformation occurs by slip on either $\{110\}\langle 111 \rangle$ or $\{112\}\langle 111 \rangle$ systems. Stress transformation induced nanosized metastable products and dislocation based plasticity interact with each other in ways are incompletely understood at this time, such that plasticity in the β phase remains a rich field for further exploration.

Plasticity in dual-phase structures is determined by several factors that act in consonance and whose effects are difficult to isolate. Figure 35 summarizes these effects. Plasticity usually initiates in softer equiaxed α in grains oriented for basal and prismatic slip. A variety of factors can then influence the spread of plasticity. Microtextured regions can increase slip lengths and exacerbate stress and plastic strain heterogeneities. Stress and strain incompatibilities can arise between hard and soft grains, as well as between microtextured regions and randomly oriented grains. Slip transfer to transformed β regions depends on the strength of the transformed β and relative orientation of equiaxed α and adjacent β . The strength of transformed β depends on the scale of lath α as well as its distribution and the strength of the lath α/β interface, which appears to be a weak obstacle. The presence of grain boundary α can significantly influence the initiation of plasticity if the grain boundary films are surrounded by relatively hard transformed β such that initial plasticity localizes into the softer grain boundary α . In addition, a major part of the strengths of Ti alloys results from the interactions of slip bands with α/α grain boundaries. Grain boundary related processes involves a combination of slip transmission, blocked slip, shear accommodation by grain boundaries and twinning.

Crystal plasticity simulations combined with experimental characterization techniques have provided a new understanding of the interplay between mechanics and microstructure. This topic is important as the mechanical response is governed by strain localization and stress and strain partitioning at the microstructural scale. The simulations were enabled by novel characterization techniques as well as efficient simulation approaches and high-performance calculation capabilities. Guidelines are currently available to simulate the onset and the development of slip activity as well as crack nucleation under a wide range of loading conditions including high

temperatures, high rates and complex loading paths with mechanistic and microstructural considerations. In particular, simulation of time dependent deformation processes such as room temperature creep induced load shedding from soft grains on to hard grains is key to understanding dwell effects at near ambient temperatures Ti alloys. Promising insights arise from the explicit consideration of type-2 residual stress, which has been a long time standing issue regarding fatigue prediction and can now be measured and incorporated into crystal plasticity calculations. In addition, major efforts have been put into the simulation of slip transfer. However, the level of fidelity achieved will be further improved in the future with the multiplication of experimental data used as input for simulations, progress in microstructure reconstruction, improved models and combination of simulation techniques to cope with intrinsic limitations of conventional crystal plasticity models, which often ignore the role of planar slip, resultant local shear stresses at interfaces and details of dislocation reactions and dislocation generation at interfaces and boundaries for instance.

Finally, we have briefly discussed the relation between microplasticity and the behavior of Ti alloys submitted to fatigue and dwell-fatigue loading. Extensive studies of the onset and the development of plasticity allowed significant progress in the understanding of the behavior of Ti alloys under cyclic loading. In addition, the analysis and the identification of crack initiation and growth mechanisms has allowed the development of suitable simulation approaches, in turn providing a new understanding of the effect of microstructural features as well as prediction capabilities with probabilistic approaches and considerations of representative microstructural volumes.

ACKNOWLEDGMENTS

DB acknowledges the support of the J.C Bose Fellowship of DST and the Raja Ramanna Fellowship of the DAE, India.

REFERENCES

- D. Banerjee and J.C. Williams: *Acta Mater.*, 2013, vol. 61, pp. 844–79.
- G. Lütjering and J.C. Williams: *Titanium*, 2nd ed., Springer, Berlin, 2007.
- Y. Zheng, R.E.A. Williams, S. Nag, R. Banerjee, H.L. Fraser, and D. Banerjee: *Scripta Mater.*, 2016, vol. 116, pp. 49–52.
- M. Tahara, H.Y. Kim, T. Inamura, H. Hosoda, and S. Miyazaki: *Acta Mater.*, 2011, vol. 59, pp. 6208–18.
- D. Choudhuri, Y. Zheng, T. Alam, R. Shi, M. Hendrickson, S. Banerjee, Y. Wang, S.G. Srinivasan, H. Fraser, and R. Banerjee: *Acta Mater.*, 2017, vol. 130, pp. 215–28.
- A.T. Churchman: *Proc. R. Soc. Lond. A*, 1954, vol. 226, pp. 216–26.
- G.H. Teichert, N.S.H. Gunda, S. Rudraraju, A.R. Natarajan, B. Puchala, K. Garikipati, and A. Van der Ven: *Computat. Mater. Sci.*, 2017, vol. 128, pp. 127–39.
- A. van de Walle and M. Asta: *Metall. Mater. Trans. A*, 2002, vol. 33A, pp. 735–41.
- F. Ye, W.-Z. Zhang, and D. Qiu: *Acta Mater.*, 2004, vol. 52, pp. 2449–60.
- Y. Zheng, R.E.A. Williams, G.B. Viswanathan, W.A.T. Clark, and H.L. Fraser: *Acta Mater.*, 2018, vol. 150, pp. 25–39.
- R. Shi, V. Dixit, G.B. Viswanathan, H.L. Fraser, and Y. Wang: *Acta Mater.*, 2016, vol. 102, pp. 197–211.
- B. Dash, R. Jangid, S.R. Koneru, A. Pilchak, and D. Banerjee: *Philos. Mag.*, 2019, vol. 99, pp. 956–70.
- T. Liu, L. Germain, J. Teixeira, E. Aeby-Gautier, and N. Gey: *Acta Mater.*, 2017, vol. 141, pp. 97–108.
- S. Balachandran, R. Jangid, S.R. Koneru, A. Pilchak, and D. Banerjee: *Proceedings 14th International Conference on Titanium*, France, 2019.
- D. Choudhuri, A. Kashiwar, R. Shi, Y. Wang, R. Banerjee, and D. Banerjee: *Acta Mater.* Submitted for publication.
- Y. Zheng, R.E.A. Williams, D. Wang, R. Shi, S. Nag, P. Kami, J.M. Sosa, R. Banerjee, Y. Wang, and H.L. Fraser: *Acta Mater.*, 2016, vol. 103, pp. 850–58.
- L. Thijs, F. Verhaeghe, T. Craeghs, J.V. Humbeeck, and J.-P. Kruth: *Acta Mater.*, 2010, vol. 58, pp. 3303–12.
- S.L. Semiatin: *Metall. Mater. Trans. A*, 2020, vol. 51, pp. 2593–25.
- S. Balachandran, S. Kumar, and D. Banerjee: *Acta Mater.*, 2017, vol. 131, pp. 423–34.
- N. Gey, P. Bocher, E. Uta, L. Germain, and M. Humbert: *Acta Mater.*, 2012, vol. 60, pp. 2647–55.
- H. Ogi, S. Kai, H. Ledbetter, R. Tarumi, M. Hirao, and K. Takashima: *Acta Mater.*, 2004, vol. 52, pp. 2075–80.
- R.A. Adebisi, S. Sathish, A.L. Pilchak, and P.A. Shade: *AIP Conf. Proc.*, 2016, vol. 1706, p. 070005.
- E.S. Fisher and C.J. Renken: *Phys. Rev.*, 1964, vol. 135, pp. A482–94.
- J.-Y. Kim, V. Yakovlev, and S.I. Rokhlin: in *AIP Conference Proceedings*, vol. 615, AIP Publishing, 2002, pp. 1118–25.
- J.W. Flowers, Jr, K.C. O'Brien, and P.C. McEleney: *J. Less Common Met.*, 1964, vol. 7, pp. 393–95.
- A.M. Stapleton, S.L. Raghunathan, I. Bantounas, H.J. Stone, T.C. Lindley, and D. Dye: *Acta Mater.*, 2008, vol. 56, pp. 6186–96.
- E. Wielewski, D.E. Boyce, J.-S. Park, M.P. Miller, and P.R. Dawson: *Acta Mater.*, 2017, vol. 126, pp. 469–80.
- R.H. Olsen and H.A. Moreen: *Metall. Trans.*, 1973, vol. 4, pp. 701–05.
- T.J. Turner, P.A. Shade, J.V. Bernier, S.F. Li, J.C. Schuren, P. Kenesei, R.M. Suter, and J. Almer: *Metall. Mater. Trans. A*, 2017, vol. 48, pp. 627–47.
- N. Hsu and H. Conrad: *Scripta Metall.*, 1971, vol. 5, pp. 905–08.
- Y.T. Lee and G. Welsch: *Mater. Sci. Eng. A*, 1990, vol. 128, pp. 77–89.
- S. Naka, A. Lasalmonie, P. Costa, and L.P. Kubin: *Philos. Mag. A*, 1988, vol. 57, pp. 717–40.
- M. Ghazisaeidi and D.R. Trinkle: *Acta Mater.*, 2014, vol. 76, pp. 82–86.
- E. Clouet, D. Caillard, N. Chaari, F. Onimus, and D. Rodney: *Nat. Mater.*, 2015, vol. 14, pp. 931–36.
- M. Poschmann, M. Asta, and D.C. Chrzan: *Comput. Mater. Sci.*, 2019, vol. 161, pp. 261–64.
- M.P. Biget and G. Saada: *Philos. Mag. A*, 1989, vol. 59, pp. 747–57.
- D. Caillard, M. Gaumé, and F. Onimus: *Acta Mater.*, 2018, vol. 155, pp. 23–34.
- P. Kwasniak and E. Clouet: *Scripta Mater.*, 2019, vol. 162, pp. 296–99.
- H. Conrad: *Prog. Mater. Sci.*, 1981, vol. 26, pp. 123–403.
- N. Chaari, D. Rodney, and E. Clouet: *Scripta Mater.*, 2019, vol. 162, pp. 200–03.
- Q. Yu, L. Qi, T. Tsuru, R. Traylor, D. Rugg, J.W. Morris, M. Asta, D.C. Chrzan, and A.M. Minor: *Science*, 2015, vol. 347, pp. 635–39.
- B. Barkia, V. Doquet, J.P. Couzinié, I. Guillot, and E. Hériprié: *Mater. Sci. Eng. A*, 2015, vol. 636, pp. 91–102.
- T. Tsuru, M. Itakura, M. Yamaguchi, C. Watanabe, and H. Miura: *The Effect of Al and V Solutes on Dislocation Motion in Titanium Alloys: A First-Principles Study*, Social Science Research Network, Rochester, 2018.

44. T. Sakai and M.E. Fine: *Scripta Metall.*, 1974, vol. 8, pp. 541–44.
45. T. Neeraj†, M.F. Savage, J. Tatalovich, L. Kovarik, R.W. Hayes, and M.J. Mills: *Philos. Mag.*, 2005, vol. 85, pp. 279–95.
46. I.P. Jones and W.B. Hutchinson: *Acta Metall.*, 1981, vol. 29, pp. 951–68.
47. W. Roberts, J. Gong, A.J. Wilkinson, and E. Tarleton: *Scripta Mater.*, 2020, vol. 178, pp. 119–23.
48. Z. Wu and W.A. Curtin: *Proc Natl Acad Sci USA*, 2016, vol. 113, pp. 11137–42.
49. W.J. Joost, S. Ankem, and M.M. Kuklja: *Acta Mater.*, 2016, vol. 105, pp. 44–51.
50. Q. Luan, T.B. Britton, and T.-S. Jun: *Mater. Sci. Eng. A*, 2018, vol. 734, pp. 385–97.
51. A.A. Salem, S.R. Kalidindi, and R.D. Doherty: *Acta Mater.*, 2003, vol. 51, pp. 4225–37.
52. J.C. Williams, A.W. Sommer, and P.P. Tung: *Metall. Trans.*, 1972, vol. 3, pp. 2979–84.
53. J.C. Williams, R.G. Baggerly, and N.E. Paton: *Metall. Mater. Trans. A*, 2002, vol. 33, pp. 837–50.
54. A. Fitzner, D.G.L. Prakash, J.Q. da Fonseca, M. Thomas, S.-Y. Zhang, J. Kelleher, P. Manuel, and M. Preuss: *Acta Mater.*, 2016, vol. 103, pp. 341–51.
55. A. Chakraborty, C. Zhang, S. Balachandran, T.R. Bieler, and P. Eisenlohr: *Acta Mater.*, 2020, vol. 184, pp. 241–53.
56. J. Gong and A.J. Wilkinson: *Acta Mater.*, 2009, vol. 57, pp. 5693–705.
57. S. Hémery and P. Villedchaise: *Mater. Sci. Eng. A*, 2017, vol. 697, pp. 177–83.
58. S. Hémery, V.T. Dang, L. Signor, and P. Villedchaise: *Metall. Mater. Trans. A*, 2018, pp. 1–9.
59. S. Hémery and P. Villedchaise: *Acta Mater.*, 2017, vol. 141, pp. 285–93.
60. S. Hémery, A. Nait-Ali, M. Guéguen, and P. Villedchaise: *Mater. Des.*, 2018, vol. 137, pp. 22–32.
61. S. Hémery and P. Villedchaise: *Metall. Mater. Trans. A*, 2018, pp. 1–4.
62. A. Radecka, P.A.J. Bagot, T.L. Martin, J. Coakley, V.A. Vorontsov, M.P. Moody, H. Ishii, D. Rugg, and D. Dye: *Acta Mater.*, 2016, vol. 112, pp. 141–49.
63. A. Radecka, J. Coakley, V.A. Vorontsov, T.L. Martin, P.A.J. Bagot, M.P. Moody, D. Rugg, and D. Dye: *Scripta Mater.*, 2016, vol. 117, pp. 81–85.
64. G. Welsch, G. Lütjering, K. Gazioglu, and W. Bunk: *MTA*, 1977, vol. 8, pp. 169–77.
65. M.C. Brandes, M.J. Mills, and J.C. Williams: *Metall. Mater. Trans. A*, 2010, vol. 41, pp. 3463–72.
66. G. Welsch and W. Bunk: *MTA*, 1982, vol. 13, pp. 889–99.
67. A. Radecka, J. Coakley, I.P. Jones, D. Rugg, T.C. Lindley, and D. Dye: *Mater. Sci. Eng. A*, 2016, vol. 650, pp. 28–37.
68. S. Hémery and P. Villedchaise: *Scripta Mater.*, 2017, vol. 130, pp. 157–60.
69. H.Y. Kim, Y. Ikehara, J.I. Kim, H. Hosoda, and S. Miyazaki: *Acta Mater.*, 2006, vol. 54, pp. 2419–29.
70. P.J.S. Buenconsejo, H.Y. Kim, H. Hosoda, and S. Miyazaki: *Acta Mater.*, 2009, vol. 57, pp. 1068–77.
71. Y. Danard, R. Poulain, M. Garcia, R. Guillou, D. Thiaudière, S. Mantri, R. Banerjee, F. Sun, and F. Prima: *Materialia*, 2019, vol. 8, p. 100507.
72. F. Sun, J.Y. Zhang, M. Marteleur, C. Brozek, E.F. Rauch, M. Veron, P. Vermaut, P.J. Jacques, and F. Prima: *Scripta Mater.*, 2015, vol. 94, pp. 17–20.
73. T. Saito, T. Furuta, J.-H. Hwang, S. Kuramoto, K. Nishino, N. Suzuki, R. Chen, A. Yamada, K. Ito, Y. Seno, T. Nonaka, H. Ikehata, N. Nagasako, C. Iwamoto, Y. Ikuhara, and T. Sakuma: *Science*, 2003, vol. 300, pp. 464–7.
74. L.-C. Zhang and L.-Y. Chen: *Adv. Eng. Mater.*, 2019, vol. 21, p. 1801215.
75. M. Abdel-Hady, K. Hinoshita, and M. Morinaga: *Scripta Mater.*, 2006, vol. 55, pp. 477–80.
76. Q. Liang, Z. Kloenne, Y. Zheng, D. Wang, S. Antonov, Y. Gao, Y. Hao, R. Yang, Y. Wang, and H.L. Fraser: *Scripta Mater.*, 2020, vol. 177, pp. 181–85.
77. L. Lilensten, Y. Danard, C. Brozek, S. Mantri, P. Castany, T. Gloriant, P. Vermaut, F. Sun, R. Banerjee, and F. Prima: *Acta Mater.*, 2019, vol. 162, pp. 268–76.
78. S. Hanada, M. Ozeki, and O. Izumi: *MTA*, 1985, vol. 16, pp. 789–95.
79. S. Hanada and O. Izumi: *Metall. Mater. Trans. A*, 1987, vol. 18, pp. 265–71.
80. S. Hanada and O. Izumi: *MTA*, 1980, vol. 11, pp. 1447–52.
81. H. Tobe, H.Y. Kim, T. Inamura, H. Hosoda, and S. Miyazaki: *Acta Mater.*, 2014, vol. 64, pp. 345–55.
82. S.A. Mantri, D. Choudhuri, T. Alam, V. Ageh, F. Sun, F. Prima, and R. Banerjee: *Scripta Mater.*, 2017, vol. 130, pp. 69–73.
83. M.J. Lai, T. Li, and D. Raabe: *Acta Mater.*, 2018, vol. 151, pp. 67–77.
84. J.F. Xiao, Z.H. Nie, Z.W. Ma, G.F. Liu, F. Hao, and C.W. Tan: *Mater. Sci. Eng. A*, 2020, vol. 772, p. 138687.
85. W. Chen, S. Cao, W. Kou, J. Zhang, Y. Wang, Y. Zha, Y. Pan, Q. Hu, Q. Sun, and J. Sun: *Acta Mater.*, 2019, vol. 170, pp. 187–204.
86. J. Gao, A.J. Knowles, D. Guan, and W.M. Rainforth: *Scripta Mater.*, 2019, vol. 162, pp. 77–81.
87. E. Levine, S. Hayden, and H. Margolin: *Acta Metall.*, 1974, vol. 22, pp. 1443–48.
88. L. Qi, C. Chen, H. Duan, S. He, Y. Hao, H. Ye, R. Yang, and K. Du: *Acta Mater.*, 2019, vol. 174, pp. 217–26.
89. Y. Wang, J. Gao, H. Wu, S. Yang, X. Ding, D. Wang, X. Ren, Y. Wang, X. Song, and J. Gao: *Sci. Rep.*, 2014, vol. 4, pp. 1–5.
90. Q. Liang, D. Wang, Y. Zheng, S. Zhao, Y. Gao, Y. Hao, R. Yang, D. Banerjee, H.L. Fraser, and Y. Wang: *Acta Mater.*, 2020, vol. 186, pp. 415–24.
91. M. Tane, T. Nakano, S. Kuramoto, M. Niinomi, N. Takesue, and H. Nakajima: *Acta Mater.*, 2013, vol. 61, pp. 139–50.
92. M. Tane, T. Nakano, S. Kuramoto, M. Hara, M. Niinomi, N. Takesue, T. Yano, and H. Nakajima: *Acta Mater.*, 2011, vol. 59, pp. 6975–88.
93. S. Kuramoto, T. Furuta, J.H. Hwang, K. Nishino, and T. Saito: *Metall. Mater. Trans. A*, 2006, vol. 37, pp. 657–62.
94. R.J. Talling, R.J. Dashwood, M. Jackson, and D. Dye: *Acta Mater.*, 2009, vol. 57, pp. 1188–98.
95. E. Plancher, C.C. Tasan, S. Sandloebes, and D. Raabe: *Scripta Mater.*, 2013, vol. 68, pp. 805–08.
96. Y. Zheng, D. Banerjee, and H.L. Fraser: *Scripta Mater.*, 2016, vol. 116, pp. 131–34.
97. Y. Zheng, T. Alam, R. Banerjee, D. Banerjee, and H.L. Fraser: *Scripta Mater.*, 2018, vol. 152, pp. 150–53.
98. P. Castany, M. Besse, and T. Gloriant: *Scripta Mater.*, 2012, vol. 66, pp. 371–73.
99. S. Hémery, A. Nait-Ali, M. Guéguen, J. Wendorf, A.T. Polonsky, M.P. Echlin, J.C. Stinville, T.M. Pollock, and P. Villedchaise: *Acta Mater.*, 2019, vol. 181, pp. 36–48.
100. S. Hémery, A. Nait-Ali, and P. Villedchaise: *Mech. Mater.*, 2017, vol. 109, pp. 1–10.
101. V. Hasija, S. Ghosh, M.J. Mills, and D.S. Joseph: *Acta Mater.*, 2003, vol. 51, pp. 4533–49.
102. P.R. Dawson, D.E. Boyce, J.-S. Park, E. Wielewski, and M.P. Miller: *Acta Mater.*, 2018, vol. 144, pp. 92–106.
103. S. Zaefferer: *Mater. Sci. Eng. A*, 2003, vol. 344, pp. 20–30.
104. M.H. Pourian, P. Pilvin, F. Bridier, and P. Bocher: *Comput. Mater. Sci.*, 2014, vol. 92, pp. 468–75.
105. F. Bridier, P. Villedchaise, and J. Mendez: *Acta Mater.*, 2005, vol. 53, pp. 555–67.
106. S. Ankem and H. Margolin: *MTA*, 1980, vol. 11, pp. 963–72.
107. P. Castany, F. Pettinari-Sturmel, J. Douin, and A. Coujou: *Mater. Sci. Eng. A*, 2008, vols. 483–484, pp. 719–22.
108. P. Castany, F. Pettinari-Sturmel, J. Douin, and A. Coujou: *Mater. Sci. Eng. A*, 2017, vol. 680, pp. 85–91.
109. P. Castany, F. Pettinari-Sturmel, J. Crestou, J. Douin, and A. Coujou: *Acta Mater.*, 2007, vol. 55, pp. 6284–91.
110. D. Deka, D.S. Joseph, S. Ghosh, and M.J. Mills: *Metall. Mater. Trans. A*, 2006, vol. 37, pp. 1371–88.
111. Z. Zhang, T.-S. Jun, T.B. Britton, and F.P.E. Dunne: *J. Mech. Phys. Solids*. <https://doi.org/10.1016/j.jmps.2016.06.007>.
112. C. Lavogiez, S. Hémery, and P. Villedchaise: *Int. J. Fatigue*, 2019, p. 105341.
113. S. Hémery and P. Villedchaise: *Acta Mater.*, 2019, vol. 171, pp. 261–74.
114. D. Lunt, T. Busolo, X. Xu, J. Quinta da Fonseca, and M. Preuss: *Acta Mater.*, 2017, vol. 129, pp. 72–82.

115. M.P. Echlin, J.C. Stinville, V.M. Miller, W.C. Lenthe, and T.M. Pollock: *Acta Mater.*, 2016, vol. 114, pp. 164–75.
116. C. Lavogiez, S. Hémerly, and P. Villedchaise: *Scripta Mater.*, 2018, vol. 157, pp. 30–33.
117. H. Li, C.J. Boehlert, T.R. Bieler, and M.A. Crimp: *Philos. Mag.*, 2012, vol. 92, pp. 2923–46.
118. Z. Zhang and F.P.E. Dunne: *Int. J. Fatigue*, 2018, vol. 113, pp. 324–34.
119. T.-S. Jun, D.E.J. Armstrong, and T.B. Britton: *J. Alloys Compds.* <https://doi.org/10.1016/j.jallcom.2016.02.146>.
120. Z. Zhang, T.-S. Jun, T.B. Britton, and F.P.E. Dunne: *Acta Mater.*, 2016, vol. 118, pp. 317–30.
121. K. Chatterjee, J.Y.P. Ko, J.T. Weiss, H.T. Philipp, J. Becker, P. Purohit, S.M. Gruner, and A.J. Beaudoin: *J. Mech. Phys. Solids*, 2017, vol. 109, pp. 95–116.
122. A. Banerjee, S. Balachandran, S. Suwas, and D. Banerjee: in *Proceedings of the 13th World Conference on Titanium*, Wiley, 2016, pp. 1095–101.
123. L.R. Zeng, H.L. Chen, X. Li, L.M. Lei, and G.P. Zhang: *J. Mater. Sci. Technol.* <https://doi.org/10.1016/j.jmst.2017.07.016>.
124. Y. Chong, T. Bhattacharjee, M.-H. Park, A. Shibata, and N. Tsuji: *Mater. Sci. Eng. A*, 2018, vol. 730, pp. 217–22.
125. C. de Formanoir, G. Martin, F. Prima, S.Y.P. Allain, T. Des-solier, F. Sun, S. Vivès, B. Hary, Y. Bréchet, and S. Godet: *Acta Mater.*, 2019, vol. 162, pp. 149–62.
126. D. Lunt, X. Xu, T. Busolo, J. Quinta da Fonseca, and M. Preuss: *Scripta Mater.*, 2018, vol. 145, pp. 45–49.
127. A. Gysler and S. Weissmann: *Mater. Sci. Eng.*, 1977, vol. 27, pp. 181–93.
128. D. Banerjee and J.C. Williams: *Def. Sc. J.*, 2014, vol. 36, pp. 191–206.
129. L. Germain, N. Gey, M. Humbert, P. Vo, M. Jahazi, and P. Bocher: *Acta Mater.*, 2008, vol. 56, pp. 4298–308.
130. I. Bantounas, T.C. Lindley, D. Rugg, and D. Dye: *Acta Mater.*, 2007, vol. 55, pp. 5655–65.
131. V. Sinha, M.J. Mills, and J.C. Williams: *Metall. Mater. Trans. A*, 2006, vol. 37, pp. 2015–26.
132. D. Lunt, J.Q. da Fonseca, D. Rugg, and M. Preuss: *Mater. Sci. Eng. A*, 2017, vol. 680, pp. 444–53.
133. S. Hémerly, P. Nizou, and P. Villedchaise: *Mater. Sci. Eng.*, 2018, vol. 709, pp. 277–84.
134. J.R. Mayeur and D.L. McDowell: *Int. J. Plast.*, 2007, vol. 23, pp. 1457–85.
135. M. Peters, A. Gysler, and G. Lütjering: *MTA*, 1984, vol. 15, pp. 1597–605.
136. M.R. Bache and W.J. Evans: *Mater. Sci. Eng. A*, 2001, vols. 319–321, pp. 409–14.
137. W.J. Evans, J.P. Jones, and M.T. Whittaker: *Int. J. Fatigue*, 2005, vol. 27, pp. 1244–50.
138. E.O. Hall: *Proc. Phys. Soc. B*, 1951, vol. 64, pp. 747–53.
139. N.J. Petch. The cleavage strength of polycrystals. *J. Iron Steel Inst.*, vol. 174, 1953, pp. 25–28. References—Scientific Research Publish. [http://www.scirp.org/\(S\(351jmbntvnsjt1aadkposzje\)\)/reference/ReferencesPapers.aspx?ReferenceID=426784](http://www.scirp.org/(S(351jmbntvnsjt1aadkposzje))/reference/ReferencesPapers.aspx?ReferenceID=426784). Accessed 8 August 2017.
140. Y. Chong, G. Deng, S. Gao, J. Yi, A. Shibata, and N. Tsuji: *Scripta Mater.*, 2019, vol. 172, pp. 77–82.
141. G. Venkatramani, S. Ghosh, and M. Mills: *Acta Mater.*, 2007, vol. 55, pp. 3971–86.
142. M. Zhang, J. Zhang, and D.L. McDowell: *Int. J. Plast.*, 2007, vol. 23, pp. 1328–48.
143. P.C. Collins, S. Koduri, B. Welk, J. Tiley, and H.L. Fraser: *Metall. Mater. Trans. A*, 2013, vol. 44, pp. 1441–53.
144. W.J. Evans and M.R. Bache: *Int. J. Fatigue*, 1994, vol. 16, pp. 443–52.
145. R. Ding, J. Gong, A.J. Wilkinson, and I.P. Jones: *Acta Mater.*, 2016, vol. 103, pp. 416–23.
146. J. Luster and M.A. Morris: *MMTA*, 1995, vol. 26, pp. 1745–56.
147. Z. Zheng, D.S. Balint, and F.P.E. Dunne: *Acta Mater.*, 2017, vol. 127, pp. 43–53.
148. S. Hémerly, C. Tromas, and P. Villedchaise: *Mater.*, 2019, vol. 5, p. 100189.
149. S. Joseph, I. Bantounas, T.C. Lindley, and D. Dye: *Int. J. Plast.*, 2018, vol. 100, pp. 90–103.
150. F. Coghe, W. Tirry, L. Rabet, D. Schryvers, and P. Van Houtte: *Mater. Sci. Eng. A*, 2012, vol. 537, pp. 1–10.
151. D.G.L. Prakash, R. Ding, R.J. Moat, I. Jones, P.J. Withers, J.Q. da Fonseca, and M. Preuss: *Mater. Sci. Eng. A*, 2010, vol. 527, pp. 5734–44.
152. L. Wang, Y. Yang, P. Eisenlohr, T.R. Bieler, M.A. Crimp, and D.E. Mason: *Metall. Mater. Trans. A*, 2009, vol. 41, pp. 421–30.
153. D. He, J. Zhu, S. Zaefferer, and D. Raabe: *Mater. Des.*, 2014, vol. 56, pp. 937–42.
154. S. Suri, G.B. Viswanathan, T. Neeraj, D.-H. Hou, and M.J. Mills: *Acta Mater.*, 1999, vol. 47, pp. 1019–34.
155. M.F. Savage, J. Tatalovich, and M.J. Mills: *Philos. Mag.*, 2004, vol. 84, pp. 1127–54.
156. M.F. Savage, J. Tatalovich, M. Zupan, K.J. Hemker, and M.J. Mills: *Mater. Sci. Eng. A*, 2001, vols. 319–321, pp. 398–403.
157. P. Zhao, C. Shen, M.F. Savage, J. Li, S.R. Niezgoda, M.J. Mills, and Y. Wang: *Acta Mater.*, 2019, vol. 171, pp. 291–305.
158. S. Waheed, Z. Zheng, D.S. Balint, and F.P.E. Dunne: *Acta Mater.*, 2019, vol. 162, pp. 136–48.
159. I. Ghamarian, P. Samimi, V. Dixit, and P.C. Collins: *Metall. Mater. Trans. A*, 2015, vol. 46, pp. 5021–37.
160. P.C. Collins, C.V. Haden, I. Ghamarian, B.J. Hayes, T. Ales, G. Penso, V. Dixit, and G. Harlow: *JOM*, 2014, vol. 66, pp. 1299–309.
161. D. Peirce, R.J. Asaro, and A. Needleman: *Acta Metall.*, 1982, vol. 30, pp. 1087–119.
162. Thermodynamics and kinetics of slip: [by] U.F. Kocks, A.S. Argon and M.F. Ashby. (Livre, 1975) [WorldCat.org]<https://www.worldcat.org/title/thermodynamics-and-kinetics-of-slip-by-u-f-kocks-as-argon-and-mf-ashby/oclc/911808627?referer=di&ht=edition>. Accessed 16 Oct 2019.
163. B.D. Smith, D.S. Shih, and D.L. McDowell: *Int. J. Plast.*, 2018, vol. 101, pp. 1–23.
164. A. Shahba and S. Ghosh: *Int. J. Plast.*, 2016, vol. 87, pp. 48–68.
165. S. Ghosh, A. Shahba, X. Tu, E.L. Huskins, and B.E. Schuster: *Int. J. Plast.*, 2016, vol. 87, pp. 69–85.
166. Z. Zhang, M.A. Cuddihy, and F.P.E. Dunne: *Proc. R. Soc. A*, 2015, vol. 471, p. 20150214.
167. Z. Zheng, S. Waheed, D.S. Balint, and F.P.E. Dunne: *Int. J. Plast.*, 2018, vol. 104, pp. 23–38.
168. M. Kasemer, M.P. Echlin, J.C. Stinville, T.M. Pollock, and P. Dawson: *Acta Mater.*, 2017, vol. 136, pp. 288–302.
169. V. Tari, R.A. Lebensohn, R. Pokharel, T.J. Turner, P.A. Shade, J.V. Bernier, and A.D. Rollett: *Acta Mater.*, 2018, vol. 154, pp. 273–83.
170. M. Zhang, F. Bridier, P. Villedchaise, J. Mendez, and D.L. McDowell: *Acta Mater.*, 2010, vol. 58, pp. 1087–96.
171. D.C. Pagan, P.A. Shade, N.R. Barton, J.-S. Park, P. Kenesei, D.B. Menasche, and J.V. Bernier: *Acta Mater.*, 2017, vol. 128, pp. 406–17.
172. Z. Zheng, D.S. Balint, and F.P.E. Dunne: *Int. J. Plast.*, 2016, vol. 87, pp. 15–31.
173. F. Bridier, D.L. McDowell, P. Villedchaise, and J. Mendez: *Int. J. Plast.*, 2009, vol. 25, pp. 1066–82.
174. T. Ozturk and A.D. Rollett: *Comput. Mech.*, 2017, pp. 1–16.
175. P.J. Ashton, T.-S. Jun, Z. Zhang, T.B. Britton, A.M. Harte, S.B. Leen, and F.P.E. Dunne: *Int. J. Fatigue*, 2017, vol. 100, pp. 377–87.
176. T. Neeraj, D.-H. Hou, G.S. Daehn, and M.J. Mills: *Acta Mater.*, 2000, vol. 48, pp. 1225–38.
177. K. Kapoor and M.D. Sangid: *Mater. Sci. Eng. A*, 2018, vol. 729, pp. 53–63.
178. R.A. Lebensohn, A.K. Kanjarla, and P. Eisenlohr: *Int. J. Plast.*, 2012, vols. 32–33, pp. 59–69.
179. F. Bridier, P. Villedchaise, and J. Mendez: *Acta Mater.*, 2008, vol. 56, pp. 3951–62.
180. Y. Mahajan and H. Margolin: *MTA*, 1982, vol. 13, pp. 269–74.
181. A.S. Beranger, X. Feaugas, and M. Clavel: *Mater. Sci. Eng. A*, 1993, vol. 172, pp. 31–41.
182. X. Feaugas and M. Clavel: *Acta Mater.*, 1997, vol. 45, pp. 2685–701.
183. C.A. Stubbington and A.W. Bowen: *J. Mater. Sci.*, 1974, vol. 9, pp. 941–47.
184. D.K. Benson, J.C. Grosskreutz, and G.G. Shaw: *MT*, 1972, vol. 3, pp. 1239–48.

185. A.L. Pilchak and J.C. Williams: *Metall. Mater. Trans. A*, 2011, vol. 42, pp. 1000–27.
186. C.J. Szczepanski, S.K. Jha, J.M. Larsen, and J.W. Jones: *Metall. Mater. Trans. A*, 2008, vol. 39A, pp. 2841–51.
187. I. Bantounas, D. Dye, and T.C. Lindley: *Acta Mater.*, 2009, vol. 57, pp. 3584–95.
188. V. Sinha, A.L. Pilchak, S.K. Jha, W.J. Porter, R. John, and J.M. Larsen: *Metall. Mater. Trans. A*, 2018, vol. 49A, pp. 1061–78.
189. J. Everaerts, D. Gontcharov, B. Verlinden, and M. Wevers: *Int. J. Fatigue*, 2017, vol. 98, pp. 203–11.
190. G. Lütjering: *Mater. Sci. Eng. A*, 1998, vol. 243, pp. 32–45.
191. A. Maenosono, M. Koyama, Y. Tanaka, S. Ri, Q. Wang, and H. Noguchi: *Int. J. Fatigue*, 2019, vol. 128, p. 105200.
192. S.K. Jha, C.J. Szczepanski, R. John, and J.M. Larsen: *Acta Mater.*, 2015, vol. 82, pp. 378–95.
193. K. Le Biavant, S. Pommier, and C. Prioul: *Fat. Fract. Eng. Mater. Struct.*, 2002, vol. 25, pp. 527–45.
194. S. Sasaoka, J. Arakawa, H. Akebono, A. Sugeta, Y. Shirai, E. Nakayama, and Y. Kimura: *Int. J. Fatigue*, 2018, vol. 117, pp. 371–83.
195. M. Risbet, X. Feaugas, C. Guillemer-Neel, and M. Clavel: *Scripta Mater.*, 2003, vol. 49, pp. 533–38.
196. S.K. Jha, R.A. Brockman, R.M. Hoffman, V. Sinha, A.L. Pilchak, W.J. Porter, D.J. Buchanan, J.M. Larsen, and R. John: *JOM*, 2018, pp. 1–7.
197. D.L. McDowell and F.P.E. Dunne: *Int. J. Fatigue*, 2010, vol. 32, pp. 1521–42.
198. C.P. Przybyla and D.L. McDowell: *Int. J. Plast.*, 2011, vol. 27, pp. 1871–95.
199. C.-H. Goh, J.M. Wallace, R.W. Neu, and D.L. McDowell: *Int. J. Fatigue*, 2001, vol. 23, pp. 423–35.
200. A. Fatemi, R. Molaei, S. Sharifimehr, N. Phan, and N. Shamsaei: *Int. J. Fatigue*, 2017, vol. 100, pp. 347–66.
201. K. Zhang, K.V. Yang, A. Huang, X. Wu, and C.H.J. Davies: *Int. J. Fatigue*, 2015, vol. 80, pp. 288–97.
202. D. Ozturk, A.L. Pilchak, and S. Ghosh: *Scripta Mater.*, 2017, vol. 127, pp. 15–18.
203. J. Qiu, Y. Ma, J. Lei, Y. Liu, A. Huang, D. Rugg, and R. Yang: *Metall. Mater. Trans. A*, 2014, vol. 45, pp. 6075–87.
204. V. Sinha, M.J. Mills, and J.C. Williams: *Metall. Mater. Trans. A*, 2004, vol. 35, pp. 3141–48.
205. W.J. Evans and C.R. Gostelow: *MTA*, 1979, vol. 10, pp. 1837–46.
206. M.R. Bache, M. Cope, H.M. Davies, W.J. Evans, and G. Harrison: *Int. J. Fatigue*, 1997, vol. 19, pp. 83–88.
207. F.P.E. Dunne, D. Rugg, and A. Walker: *Int. J. Plast.*, 2007, vol. 23, pp. 1061–83.
208. F.P.E. Dunne and D. Rugg: *Fatigue Fract. Eng. Mater. Struct.*, 2008, vol. 31, pp. 949–58.
209. M.C. Brandes: The Ohio State University, 2008.
210. A.L. Pilchak, M.C. Brandes, R.E.A. Williams, and J.C. Williams: *Ti 2011—Proceedings of the 12th World Conference on Titanium*, 2012, pp. 993–97.
211. X. Zheng, S. Zheng, J. Wang, Y. Ma, H. Wang, Y. Zhou, X. Shao, B. Zhang, J. Lei, R. Yang, and X. Ma: *Acta Mater.* <https://doi.org/10.1016/j.actamat.2019.10.010>.
212. A.L. Pilchak: *Scripta Mater.*, 2013, vol. 68, pp. 277–80.
213. A.L. Pilchak, A. Bhattacharjee, A.H. Rosenberger, and J.C. Williams: *Int. J. Fatigue*, 2009, vol. 31, pp. 989–94.
214. A.L. Pilchak: *Scripta Mater.*, 2014, vol. 74, pp. 68–71.
215. V. Sinha, M.J. Mills, and J.C. Williams: *J. Mater. Sci.*, 2007, vol. 42, pp. 8334–41.
216. M.R. Bache: *Int. J. Fatigue*, 2003, vol. 25, pp. 1079–87.
217. X. Song, S.Y. Zhang, D. Dini, and A.M. Korsunsky: *Comput. Mater. Sci.*, 2008, vol. 44, pp. 131–37.
218. J.A. Medina Perilla and J. Gil Sevillano: *Mater. Sci. Eng. A*, 1995, vol. 201, pp. 103–10.
219. H. Li, D.E. Mason, T.R. Bieler, C.J. Boehlert, and M.A. Crimp: *Acta Mater.*, 2013, vol. 61, pp. 7555–67.
220. Z. Zhang, T.-S. Jun, T.B. Britton, and F.P.E. Dunne: *J. Mech. Phys. Solids*, 2016, vol. 95, pp. 393–410.
221. E.S. Fisher and D. Dever: in: *The Science, Technology and Application of Titanium*, R.I. Jaffee and N.E. Promisel, eds., Pergamon, 1970, pp. 373–81.
222. C.N. Reid, J.L. Routbort, and R.A. Maynard: *J. Appl. Phys.*, 1973, vol. 44 (3), pp. 1398–99, <https://doi.org/10.1063/1.1662365>.
223. V. Hounkpati, S. Fréour, D. Gloaguen, V. Legrand, J. Kelleher, W. Kockelmann, and S. Kabra: *Acta Mater.*, 2016, vol. 109, pp. 341–52.
224. M. Tane, S. Akita, T. Nakano, K. Hagihara, Y. Umakoshi, M. Niinomi, and H. Nakajima: *Acta Mater.*, 2008, vol. 56, pp. 2856–63.
225. H.W. Jeong, Y.S. Yoo, Y.T. Lee, and J.K. Park: *J. Appl. Phys.*, 2010, vol. 108, p. 063515.
226. M. Herbig, A. King, P. Reischig, H. Proudhon, E.M. Lauridsen, J. Marrow, J.-Y. Buffière, and W. Ludwig: *Acta Mater.*, 2011, vol. 59, pp. 590–601.
227. R. Hermann, H. Hermborn, M. Calin, B. Büchner, and J. Eckert: *Scripta Mater.*, 2012, vol. 66, pp. 198–201.
228. Q. Meng, S. Guo, X. Ren, H. Xu, and X. Zhao: *Appl. Phys. Lett.*, 2014, vol. 105, p. 131907.
229. A. Schick, C.-P. Fritzen, W. Floer, Y.M.H.U. Krupp, and H.-J. Christ: *WIT Trans. Eng. Sci.* 2000, vol. 26.
230. S.L. Raghunathan, A.M. Stapleton, R.J. Dashwood, M. Jackson, and D. Dye: *Acta Mater.*, 2007, vol. 55, pp. 6861–72.
231. J.L.W. Warwick, J. Coakley, S.L. Raghunathan, R.J. Talling, and D. Dye: *Acta Mater.*, 2012, vol. 60, pp. 4117–27.

Publisher's Note Springer Nature remains neutral with regard to jurisdictional claims in published maps and institutional affiliations.